UNIVERSIDADE DE SÃO PAULO
ESCOLA DE ENGENHARIA DE SÃO CARLOS
DEPARTAMENTO DE ENGENHARIA DE ESTRUTURAS

UNIVERSITÉ PARIS-SACLAY
ÉCOLE NORMALE SUPÉRIEURE PARIS-SACLAY
LABORATOIRE DE MÉCANIQUE ET TECHNOLOGIE

Ayrton Ribeiro Ferreira

Corrected version
(Original version is available at EESC/USP)

Micromechanical modeling of effective behavior of anisotropic porous ductile materials

Modelagem micromecânica do comportamento efetivo de materiais dúcteis porosos anisótropos

Modélisation micromécanique du comportement effectif des matériaux ductiles poreux anisotropes

São Carlos

2019

Ayrton Ribeiro Ferreira

Micromechanical modeling of effective behavior of anisotropic porous ductile materials

This doctoral dissertation is submitted in partial fulfillment of requirements for the Degree of Doctor in Science – Civil Engineering (Structures) at the São Carlos School of Engineering, University of São Paulo and for the Degree of Doctor in Mechanics (Mechanical Engineering – Civil Engineering) at the École Normale Supérieure Paris-Saclay, Université Paris-Saclay.

Concentration area: Structures

Advisors: Sergio Persival Baroncini Proença
(Full professor at EESC/USP)

Ahmed Benallal
(Research director at CNRS/ENS Paris-Saclay, UPSaclay)

São Carlos

2019

Catalog card prepared by Patron Service at "Prof. Dr. Sergio Rodrigues Fontes" Library at EESC/USP

F383m

Ferreira, Ayrton Ribeiro
Micromechanical modeling of effective behavior of anisotropic porous ductile materials / Ayrton Ribeiro Ferreira ; Dissertation directed by Sergio Persival Baroncini Proença; Ahmed Benallal. -- São Carlos, 2019.
Doctoral (Dissertation) Graduate Program in Civil Engineering (Structures) and Research Area in Structures – São Carlos School of Engineering, at University of São Paulo, École Normale Supérieure Paris-Saclay of Université Paris-Saclay, 2019.

1. Ductile fracture. 2. Gurson model. 3. Anisotropy. 4. Porous materials. I. Benallal, Ahmed. II. Title.

Elena Luzia Palloni Gonçalves – CRB 8/4464

FOLHA DE JULGAMENTO

Candidato: Engenheiro **AYRTON RIBEIRO FERREIRA.**

Título da tese: "Modelagem micromecânica do comportamento efetivo de materiais dúcteis porosos anisótropos".

Data da defesa: 23/05/2019.

Comissão Julgadora:	**Resultado:**
Prof. Associado **Adair Roberto Aguiar** (Escola de Engenharia de São Carlos/EESC)	APROVADO
Profa. Associada **Larissa Driemeier** (Escola Politécnica/EP-USP)	APROVADO
Prof. Dr. **Rodrigo Bresciani Canto** (Universidade Federal de São Carlos/UFSCar)	APROVADO
Prof. Dr. **Habibou Maitournam** (École Polytecnique/Paris)	APROVADO
Prof. Dr. **Nicolas Schmitt** (Écola Normale Supérieure de Cachan/Paris Saclay)	APROVADO

Coordenador do Programa de Pós-Graduação em Engenharia Civil (Engenharia de Estruturas):
Prof. Associado **Vladimir Guilherme Haach**

Presidente da Comissão de Pós-Graduação:
Prof. Titular **Murilo Araujo Romero**

ACKNOWLEDGEMENTS

First of all, I gratefully acknowledge Sergio and Ahmed for their patient, present and inspiring guidance over the course of these intense years of research.

I am also immensely grateful to my family for their support in difficult times, their comforting presence and their incentive – and why not *understanding* – to pursue a scientific career.

I would like also to thank all my friends, which life presented me throughout the years in São Carlos and in Cachan, for the fruitful discussions and for all lessons we learned in recent years.

I am also thankful to CNPq and CAPES for the financial support during the years in São Carlos and the year in Cachan, respectively.

I could not finish without acknowledging the staff at the Departamento de Engenharia de Estruturas and at the Laboratoire de Mécanique et Technologie for their *infinite* patience, cordiality and support in the administrative matters during my doctoral years.

Muito obrigado a todos vocês! Merci beaucoup à tous !

ABSTRACT

FERREIRA, A. R. **Micromechanical modeling of effective behavior of anisotropic porous ductile materials**. 2019. 151p. Dissertation (Doctorate) – Escola de Engenharia de São Carlos, Universidade de São Paulo – École Normale Supérieure Paris-Saclay, Université Paris-Saclay, São Carlos, 2019.

The manufacturing of ductile materials generally inserts impurities into their microscopic composition. These impurities may detach from the surrounding matrix and even crack along progressive deformation. Due to the consequent incapacity of these undesirable particles of supporting any stress, these ductile materials are equivalently assumed to be porous. Porosity has been effectively shown to play a fundamental role in the mechanisms of ductile fracture. Many micromechanical models have been proposed since the 1970s with the aim of mathematically describing these mechanisms. Among them, the acclaimed Gurson model combines the averaging homogenization technique with the kinematic theorem of Limit Analysis to estimate the macroscopic yield criterion and porosity evolution law of porous ductile materials. However, the Gurson model and most of its extensions only account for isotropic ductile fracture. Thus, the purpose of the present work is to contribute to the conception of yield criteria for anisotropic porous ductile rupture. Three main contributions are hereby proposed by profiting from similar hypothesis to those of the Gurson model. The first contribution is the assessment of the influence of void morphology on overall yield criteria for those classes of materials. The second is the inclusion of an anisotropic yield criterion in the material matrix so that the macroscopic behavior presents matrix-induced anisotropy even for spherical cavities. The third and last advancement consists of generalizing the material matrix yield criterion of the Gurson model in order to include a linear transformation-based class of yield functions that has been widely used to represent specific high strength aluminum alloys. The results hereby presented highlight the consistency and robustness of the three formulations. Moreover, the role of the porosity on the modeling of yield behavior of aluminum alloys encourages further work regarding experimental parameter characterization.

Keywords: Ductile fracture. Gurson model. Anisotropy. Porous materials.

RESUMO

FERREIRA, A. R. **Modelagem micromecânica do comportamento efetivo de materiais dúcteis porosos anisótropos**. 2019. 151p. Tese (Doutorado) – Escola de Engenharia de São Carlos, Universidade de São Paulo – École Normale Supérieure Paris-Saclay, Université Paris-Saclay, São Carlos, 2019.

A fabricação de materiais dúcteis insere impurezas em suas composições microscópicas. Essas impurezas podem se soltar da matriz circundante e até trincar durante um processo de deformação progressiva. Devido à consequente incapacidade destas partículas indesejáveis para suportar qualquer esforço, estes materiais dúcteis são equivalentemente assumidos como sendo porosos. Investigações experimentais têm extensamente mostrado que a porosidade desempenha um papel fundamental nos mecanismos de ruptura de materais dúcteis. Desde a década de 1970, vários modelos micromecânicos têm sido propostos para descrever esses mecanismos matematicamente. Entre eles, o célebre modelo de Gurson combina a técnica de homogeneização com o teorema cinemático da Análise Limite para estimar o critério de plastificação macroscópica e a lei de evolução da porosidade dos materiais dúcteis porosos. No entanto, o modelo de Gurson e a maioria de suas extensões consideram apenas situações de ruptura dúctil em meios isotrópos. O objetivo do presente trabalho é, portanto, contribuir para o desenvolvimento de critérios de plastificação para a ruptura dúctil de meios porosos anisotrópos. Três principais contribuições são propostas neste trabalho, as quais se valem de hipóteses semelhantes às do modelo de Gurson. A primeira contribuição é a avaliação da influência da morfologia do vazio nos critérios de plastificação macroscópica desta classe de materiais. A segunda é a inclusão de um critério de plastificação anisotrópico na representação da matriz do material, de modo que o comportamento macroscópico exiba anisotropia induzida por ela, mesmo para cavidades esféricas. O terceiro e último avanço é a generalização do critério de plasticidade da matriz de modo a incluir uma classe de funções de plastificação baseadas em transformações lineares. Esta classe de funcões tem sido amplamente utilizada com sucesso para modelar ligas de alumínio de alta resistência. Os resultados apresentados neste trabalho atestam a coerência e robustez das três formulações. Além disso, o papel da porosidade na modelagem da plasticidade das ligas de alumínio encoraja trabalhos futuros sobre a caracterização experimental de parâmetros de anisotropia.

Palavras-chave: Ruptura dúctil. Modelo de Gurson. Anisotropia. Materiais Porosos.

RÉSUMÉ

FERREIRA, A. R. **Modélisation micromécanique du comportement effectif des matériaux ductiles poreux anisotropes**. 2019. 151p. Thèse (Doctorat) – Escola de Engenharia de São Carlos, Universidade de São Paulo – École Normale Supérieure Paris-Saclay, Université Paris-Saclay, São Carlos, 2019.

La fabrication de matériaux ductiles insère généralement des impuretés dans leurs compositions microscopiques. Ces impuretés peuvent se détacher de la matrice environnante et même se fissurer lors d'une déformation progressive. En raison de la résultante incapacité de ces particules indésirables à supporter toute contrainte, ces matériaux ductiles sont, de manière équivalente, supposés être poreux. Il a été largement démontré que la porosité joue un rôle fondamental dans les mécanismes de la rupture ductile. Depuis les années 1970, de nombreux modèles micromécaniques ont été proposés dans le but de décrire mathématiquement ces mécanismes. Parmi eux, le célèbre modèle de Gurson combine la technique d'homogénéisation avec le théorème cinématique de l'analyse limite pour estimer le critère de plastification macroscopique et la loi d'évolution de la porosité des matériaux ductiles poreux. Cependant, le modèle de Gurson, ainsi que la plupart de ses extensions, ne tient compte que de la rupture ductile isotrope. Le but du présent travail est donc de contribuer à la conception de critères de plastification pour la rupture ductile des milieux poreux anisotropes. Trois contributions principales tirant parti d'hypothèses similaires à celles du modèle de Gurson sont ici proposées. La première contribution est l'évaluation de l'influence de la morphologie des vides sur les critères de plastification macroscopique de ces classes de matériaux. La deuxième est l'inclusion d'un critère de plastification anisotrope dans la matrice du matériau, de sorte que le comportement macroscopique présente une anisotropie induite par cette matrice, y compris pour les cavités sphériques. Le troisième et dernier progrès consiste à généraliser le critère de plastification de la matrice afin d'inclure une classe de fonctions de plastification basée sur des transformations linéaires. Cette classe de fonction a été largement employée avec succès pour représenter des alliages d'aluminium à haute résistance. Les résultats ici présentés soulignent la cohérence et la robustesse des trois formulations. En outre, le rôle de la porosité sur la modélisation de la plasticité des alliages d'aluminium incite à poursuivre les travaux sur la caractérisation expérimentale des paramètres d'anisotropie.

Mots-clés : Rupture ductile. Modèle de Gurson. Anisotropie. Matériaux Poreux.

LIST OF FIGURES

LIST OF TABLES

LIST OF ABBREVIATIONS AND ACRONYMS

FEM	Finite Element Method
SEM	Scanning Electron Microscope
OAS	Orowan Alternating Slip
RVE	Representative Volume Element
REV	Representative Elementary Volume
FCC	Face-Centered Cubic
BCC	Body-Centered Cubic
GTN	Gurson-Tvergaard-Needleman
IPE	Isotropic Plastic Equivalent
BVP	Boundary Value Problem
SVD	Single Value Decomposition
I	Isotropic
C	Cubic
TI	Transversely Isotropic
T	Tetragonal
O	Orthotropic

LIST OF SYMBOLS

$\boldsymbol{\sigma}$	Microscopic stress tensor
σ_m	Microscopic hydrostatic (or *mean*) stress
σ_{eq}	Microscopic von Mises stress
ω	Microscopic stress Lode angle
σ_0	Microscopic yield stress
$\dot{\boldsymbol{\epsilon}}$	Microscopic strain rate tensor
$\dot{\boldsymbol{\epsilon}}_m$	Microscopic hydrostatic (or *mean*) strain rate
$\dot{\epsilon}_{eq}$	Microscopic equivalent strain rate
ξ	Microscopic strain rate Lode angle
$\dot{\lambda}$	Microscopic plastic multiplier rate
π	Microscopic plastic dissipation potential
$\tilde{\pi}$	Auxiliary microscopic plastic dissipation potential
π_G	Gurson's microscopic plastic dissipation potential
g	Microscopic stress function
m	Hershey-Hosford yield criterion exponent
G	Microscopic strain rate function
$\boldsymbol{\Sigma}$	Macroscopic stress tensor
Σ_m	Macroscopic hydrostatic stress
Σ_{eq}	Macroscopic von Mises stress
Θ	Macroscopic stress Lode angle
T	Macroscopic stress triaxiality
μ	Macroscopic stress Lode parameter
Σ_m^f	Macroscopic hydrostatic stress factor
$\boldsymbol{\Sigma}^G$	Gurson's macroscopic stress tensor

Σ_m^G	Gurson's macroscopic hydrostatic stress
Σ_{eq}^G	Gurson's macroscopic equivalent stress
$\dot{\boldsymbol{E}}$	Macroscopic strain rate tensor
$\dot{E}_m$	Macroscopic hydrostatic strain rate
$\dot{E}_{eq}$	Macroscopic equivalent strain rate
η	Macroscopic strain rate Lode angle
H	Macroscopic strain rate triaxiality
Π	Macroscopic plastic dissipation potential
Π_G	Gurson's macroscopic plastic dissipation potential
$\mathbb{L}$	Anisotropic linear transformation on Cauchy stresses (fourth-order tensor)
$\underline{\underline{\boldsymbol{L}}}$	Anisotropic linear transformation on Cauchy stresses (Voigt notation)
$\underline{\underline{\boldsymbol{L}}}^+$	Moore-Penrose generalized inverse of $\underline{\underline{\boldsymbol{L}}}$
$\underline{\underline{\boldsymbol{L}}}^*$	Adjoint matrix of the Moore-Penrose generalized inverse of $\underline{\underline{\boldsymbol{L}}}$
$\mathbb{C}$	Anisotropic linear transformation on deviatoric stresses (fourth-order tensor)
$\underline{\underline{\boldsymbol{C}}}$	Anisotropic linear transformation on deviatoric stresses (Voigt notation)
$\boldsymbol{s}^i$	IPE microscopic stress tensor
s_{eq}^i	IPE microscopic von Mises stress
$\tilde{s}_{eq}$	IPE auxiliary microscopic von Mises stress
S_j^i	IPE principal microscopic stresses
α	Ratio between two IPE microscopic von Mises stresses
β	Ratio between two IPE microscopic equivalent strain rates
ν	Poisson's coefficient
κ	Arbitrary nonnegative real value
ϕ	Anisotropic yield function
ψ	Isotropic yield functions

$\boldsymbol{a}^*$	Auxiliary stress variable tensor
a^*_{eq}	Auxiliary von Mises stress variable
ξ_a	Auxiliary stress Lode angle variable
f	Porosity
f_c	Critical porosity
f_F	Final fracture porosity
f^*	Porosity variable in Eq. (3.58)
l_{RVE}	RVE's characteristic length of the RVE
l_{struc}	Structure's characteristic length
l_{load}	Load's characteristic length
$\boldsymbol{x}$	Position vector in a three-dimensional space
$\boldsymbol{n}(\boldsymbol{x})$	Normal unitary vector to a given surface $\partial\Omega$, with $x \in \partial\Omega$
(e_1, e_2, e_3)	Cartesian referential system
$(e_r, e_\varphi, e_\theta)$	Spherical referential system
R	RVE's outer radius
r_v	RVE's inner radius
r_1, r_2, r_3	Principal radii of an ellipsoid following the referential (e_1, e_2, e_3)
r, φ, θ	Radius, azimuthal and zenith angles referring to $(e_r, e_\varphi, e_\theta)$
V	Total volume occupied by the RVE (i.e. including volume of voids)
Ω	Continuum domain that contains the RVE material matrix
$\bar{\Omega}$	RVE total domain (i.e. including the voided regions)
$\partial\Omega^+, \partial\Omega^-$	Outer and inner RVE contours
$\boldsymbol{F}^d$	Traction vector on the outer surface of the RVE
$\boldsymbol{u}^d$	Displacement vector on the outer surface of the RVE
$\boldsymbol{u}$	Displacement vector field
$\dot{\boldsymbol{u}}$	Velocity vector field

$\dot{\boldsymbol{u}}_G^V, \dot{\boldsymbol{u}}_G^S$	Gurson's trial velocity fields associated to pure dilatation (V) and pure distortion (S)
$\mathbb{I}$	Fourth-order identity
$\mathbb{J}$	Fourth-order deviatoric identity
$\mathbf{1}$	Second-order identity
$\underline{\underline{\boldsymbol{J}}}$	Second-order deviatoric identity
(ℓ_1, ℓ_2, ℓ_3)	Auxiliary representation of ellipsoidal principal radii
c	Scalar coefficient of $\underline{\underline{\boldsymbol{L}}}$
b_i	Barlat's components in an arbitrary orthotropic $\underline{\underline{\boldsymbol{L}}}$
ρ^1, ρ^2, ρ^3	Gauss natural (i.e. dimensionless) coordinates
$\boldsymbol{M}$	Rotation tensor
N_1, N_2, N_3	Number of integration points for the directions ρ^1, ρ^2, ρ^3.
J_ρ	Determinant of the Jacobian that maps (r, φ, θ) into ρ^1, ρ^2, ρ^3
$\tilde{H}$	Auxiliary strain rate triaxiality
$\tilde{\eta}$	Auxiliary macroscopic strain rate Lode angle
$\tilde{\boldsymbol{E}}$	Auxiliary macroscopic stain rate tensor
$N_{\tilde{H}}, N_{\tilde{\eta}}$	Number of divisions in the ranges of $\tilde{H}$ and $\tilde{\eta}$
Γ	Set of stress points that lie on the yield surface
χ_i	Interpolation shape function
ι_i	Natural (i.e. dimensionless) coordinates inside an element composed by points in Γ
err	Barlat's characterization error function
z	Barlat's special weights
d	Lankford coefficient

CONTENTS

1 INTRODUCTION

The ability of modeling failure process in structures made of ductile materials has a vital importance in a wide range of activities. For example, it can predict when, where and how a fracture may occur and propagate in rivet connections made of aluminum alloys in aircraft fuselages. Additionally, it details the perforation process in metallic plates hit by projectiles, which indicates the types of alloys that are more appropriate for specific military applications. Finally, pinned connections of tall steel towers can be prevented to fail by localization of plastic deformations, which could cause serious damage to the structure. These examples illustrate that three of the major contemporary industries benefit from the development of reliable models to understand ductile fracture processes.

Throughout the deformation process of these ductile materials, their mechanical properties may considerably vary. This variation is due to the intense plastic strain fields that concentrate around impurities in their microstructure. On the other hand, these concentration fields deform the surroundings of the impurities so intensely that they normally detach from the material matrix, which creates *pores* in the microstructure. With even more intense loads, these pores become significantly deformed in such a way that the distribution of stresses from grain to grain in the microscale prefer certain directions instead of others. Thus, consistent mathematical descriptions to account for the *anisotropy* along ductile fracture processes are required.

Studies over the last fifty years demonstrated that microscopic parameters are crucial to understand these ductile rupture processes. Additionally, not only the failure processes themselves, but also the mechanical behavior of macroscopic structures has been shown to be strongly dependent on their microstructure. Thus, a research area called micromechanics has been the subject of important developments since then with the aim of taking into account microstructure parameters in the modeling of conventional engineering structures. This field usually benefits from *homogenization* techniques so that information on the constitutive response of highly complex microstructure arrangements can be used to generate macroscopically homogeneous material models.

The aim of this doctoral dissertation is to propose advances on the mathematical descriptions of yield criteria associated to ductile rupture. The models hereby developed are based on the acclaimed Gurson model's framework. To sum up, three contributions are presented in this work, all of them focusing solely on effective yield criteria – therefore, the ongoing evolution in anisotropy with further plastic strain is not taken into account. The first contribution is the investigation of the influence of different void morphologies on the overall anisotropic behavior of ductile materials. The second one is the inclusion of a microscopic anisotropic yield criterion into the original Gurson formulation so that

the effect of anisotropic material matrices could be accounted for. Finally, the anisotropic yield criterion of the material matrix in Gurson's framework is generalized to linear transformation-based yield functions. Basically, these functions allow anisotropic aluminum alloys to be characterized with an arbitrary number of parameters.

A summary of each chapter of the doctoral dissertation is presented below.

- chapter 2 summarizes the state-of-art of the understanding of ductile rupture. Both classical background and novel tendencies in the field are discussed. The text focuses on justifying the mechanisms of ductile rupture by appointing the main experimental evidence that supports them. Moreover, some analytical and numerical studies are also pointed out in order to complement this evidence. The chapter ends with a brief overview of the main inconsistencies in the current understanding of shear-dominated failure of ductile materials that have been reported over the last fifteen years.

- chapter 3 provides an introduction to the modeling of isotropic porous ductile materials. The chapter begins by introducing the basic concepts of the averaging homogenization. The Gurson (1975) model is then presented in detail. Some of its main phenomenological extensions are also briefly discussed. Finally, with the aim of providing a basis to the understanding of the next chapters, two analytical extensions of the Gurson model are reviewed. The first one is proposed by Benallal, Desmorat and Fournage (2014), who assessed the importance of some approximations in the original formulation of the Gurson model on the overall macroscopic behavior. The more recent work of Benallal (2017) – which included the third invariant of microscopic stress into the matrix yield criterion – is also detailed and illustrated by some numerical examples.

- chapter 4 consists of the first contribution of the present doctoral dissertation. Therein, an extension of Benallal (2017) is proposed to consider different morphologies of the pores. Both spheroidal and ellipsoidal voids are explored. The results show the consistency of the formulation, as well as the robustness of the numerical implementation. Nevertheless, the anisotropic effect induced by different porous morphologies is limited to high stress triaxialities. This limitation motivated the development of the formulations in chapters 5 and 6.

- chapter 5 consists of the second contribution to the doctoral dissertation. In this chapter, the yield criterion of the material surrounding the pores as considered by Benallal (2017) is extended in order to include anisotropic material matrices. This extension relies on the continuum anisotropic yield function of Karafillis and Boyce (1993) and includes different material symmetries. Four of them are thereby explored: (i) Cubic; (ii) Transversely Isotropic; (iii) Tetragonal; and (iv) Orthotropic. Differently to chapter 4, the results point out the sensibility of the anisotropic

effects on the material matrix parameters. Besides, the confrontation of orthogonal material symmetries demonstrates the physical and mathematical consistency of the formulation.

- chapter 6 consists of the third and last contribution of this doctoral dissertation. A generalization of the microscopic yield criterion is thereby proposed with the aim of representing anisotropic material matrices that follow Barlat et al. (2005). Basically, this work provided a framework to compose yield functions that can include an arbitrary number of anisotropy parameters to be experimentally determined. This model has been widely confirmed as being an adequate formulation for continuous – not porous – modeling of aluminum alloys. Thus, chapter 6 contributes to the field by inserting this acclaimed model into a Gurson-like formulation for *porous* ductile materials. The results show a remarkable influence of the porosity on the overall macroscopic yield criterion and encourages further experimental characterization work of porous aluminum alloys.

- chapter 7 provides some details on the numerical implementation of the formulation contained in chapters 4, 5 and 6. The covered aspects are: (i) the numerical integration procedure for obtaining macroscopic yield criteria; (ii) the discretization procedure of the macroscopic strain rate variables; and (iii) an interpolation-based procedure for obtaining level-set (or *contour*) plots of three-dimensional yield surfaces.

- chapter 8 finally depicts the advantages and deficiencies of the three formulations proposed in this doctoral dissertation. Moreover, it links some of the these deficiencies to further work that must be carried out in the near future.

Three appendix sections contain complementary details on the formulations and numerical implementation hereby developed:

- Appendix A summarizes some practical aspects of the *Voigt notation* for symmetric tensor operations. This notation was used throughout every implementation of this doctoral dissertation with the aim of saving computation time.

- Appendix B proposes a numerical N-dimensional procedure to obtain level-set (or *contour*) plots of N-dimensional surfaces, with applications in Mechanics of Materials. This procedure is a generalization of that presented in section 7.3 for two-dimensional surfaces described in three-dimensional spaces.

- Appendix C lists the auxiliary derivatives that are required for the implementation of Eq. (6.16), (6.28) and (6.29).

2 AN OVERVIEW OF DUCTILE RUPTURE

2.1 Classical background

This section summarizes some important concepts about the classical view of ductile fracture. Its emphasis is to present both pioneering studies on key concepts and some of the most significant contributions to the understanding of specific phenomena. The text is strongly based on the reviews by Hahn, Kanninen and Rosenfield (1972), Schwalbe (1977), Stone et al. (1985), Garrison Jr and Moody (1987), Benzerga and Leblond (2010) and Besson (2010). Much richer and vaster overviews can be found in their works.

2.1.1 Nucleation: the genesis of voids

The manufacturing processes of steels and alloys generally result in undesirable small non-metallic particles in their microstructures. These particles are commonly called either *second-phase* particles, because of their different chemical composition to the grains that compose most of the texture, or *inclusions*, due to their undesirable presence. They can be classified into two main types. The first is called *endogenous* and refers to particles that arise from the chemical reactions in the melt. The second type is *exogenous* and represents inclusions that enter the melt during pouring. While endogenous particles are typically small and dispersed throughout the material, the exogenous ones vary in size and tend to be concentrated in specific regions of the casting (BEELEY, 2001).

Due to geometric aspects of the microstructure and to the non-metallic character of inclusions, the stress and plastic deformation tend to concentrate around them when the ductile material is under load. Then, two very important mechanisms may occur. The first one is the decohesion of the particle–matrix interface as a consequence of the intense plastic flow along the interface. Since it implies that the particle is no longer attached to the surrounding matrix, the particle can no longer contribute to the material's mechanical stiffness. Thus, it is equivalently assumed that a *void* is generated in the same position as the original inclusion. This phenomenon is called *nucleation* by *particle–matrix decohesion* and was first documented by Tipper (1948–49 apud GARRISON JR; MOODY, 1987). Then, Puttick (1959) observed it by studying copper and iron notched specimens under tensile loading. Following the conclusions of Wilcox and Clauer (1972) and Gurland (1972), the particle–matrix decohesion is likely to arise first in larger particles.

The second nucleation mechanism takes place when the particle itself – and not the interface as in the earlier case – cannot support the stress concentration imposed to it. Therefore, the particle cracks and can no longer add any stiffness to the material. In the

same way as the first case, it is thus equivalently assumed that the particle is substituted by a cavity. This mechanism is known as nucleation by *particle cracking* and one of the first experimental pieces of evidences were given by Puttick (1959). More recently, Agarwal et al. (2002) observed that the process of intermetallic particle cracking of an aluminum alloy (6061–T651) presented anisotropy behavior due to the rotation of particles during uniaxial compression tests.

Babout et al. (2004) investigated the hardness effect of aluminum alloys on void nucleation in tensile tests. For this purpose, a structural 2124 aluminum alloy and a commercially pure aluminum were chosen to represent a hard and a soft matrix, respectively. In short, they found that particle cracking generally prevails in materials with a hard matrix, while particle–matrix decohesion is associated to softer ones. Other trends about the competition of these two nucleation mechanisms are presented by Benzerga and Leblond (2010). Among them, it has been found that particle cracking is related to higher (i) matrix yield strength; (ii) matrix hardening exponent; and (iii) particle elongation along the tensile test. On the other hand, particle–matrix decohesion is normally linked to (v) higher particle stiffness and (vi) to transverse loadings.

2.1.2 Void growth

After nucleation, the progress of the loading level continues to concentrate plastic deformations in portions of the matrix around voids, which causes permanent changes in their boundaries. Due to this phenomenon, the voids can grow and evolve their shapes. This mechanism is then called *void growth*. The earlier experimental investigations that treated void growth was presented by Ashby (1966), Ashby and Johnson (1969) and Ashby (1970). The first work stated that the void growth is described mainly by dislocation motions of grains around the voids. The author also proposed a dislocation-based expression for the estimation of void growth. However, Rosenfield (1968) concluded that the predictions provided by this expression was indeed small. Additionally, the hypothesis of the dislocation influence was found not to be enough to completely describe the void growth phenomenon.

The mechanism of void growth was also introduced and explored by some studies based on analytical developments in continuum mechanics. Firstly, McClintock, Kaplan and Berg (1966) developed a fracture criterion for the growth of cylindrical voids immersed in a viscous (or plastic by a thereby specific approximation) infinite media under shear loading with a superimposed mean stress. McClintock (1968a) and McClintock (1968b) (*errata*) then generalized the earlier work and proposed a criterion for ductile fracture due to the growth of cylindrical holes under arbitrary history of load. Their main conclusions highlighted the strong influence of (i) the tensile stress transverse to the void elongation on the fracture strain (i.e. ductility); (ii) intermediate principal stress also on the fracture strain; and the history of stress and strain on ductile fracture.

Two other very important studies – also based on continuum mechanics approaches – contributed to understanding of void growth. Rice and Tracey (1969) studied the enlargement of spherical cavities in an infinite perfectly rigid–plastic medium under remote tensile stress with a superposed hydrostatic one. Their work concluded that there exists high dependence of void growth on the stress triaxiality, as well as an exponentially decrease of the fracture strain with increasing triaxiality. Then, Tracey (1971) went further by continuing the same path as the earlier work. He investigated the effects of the hardening exponent and interaction between voids within a similar framework to Rice and Tracey (1969). His conclusions indicated the decelerating influence of the hardening exponent on the void enlargement and the need for accounting for large strain theory for further investigation on the effect of interaction between voids.

2.1.3 Coalescence: the linkage between voids

The next stage of the classical view of ductile rupture consists of the linkage of adjacent voids due to the intersection of their boundaries and the consequent formation of microcracks. This stage is called *coalescence* and may occur due to four main mechanisms: (i)internal necking; (ii) microshear bands (or "void sheets"); (iii) necklace; and (iv) intergranular cracking. This propagation of a microcrack by coalescence is found to evolve in a very short time interval when compared to the mechanisms cited above, as documented by Broek (1973).

The internal necking occurs due to the enlargement of two adjacent cavities until their boundaries collapse and form only one larger cavity (Fig. 1a, 4a and 5a). The term "necking" refers to the high plastic deformations in the region between two voids just before they become linked. This mechanism was first suggested by Henry (1855 apud ARGON; IM; SAFOGLU, 1975) and, since the advent of Scanning Electron Microscopy (SEM) for mechanics in the 1950s, it has been unequivocally accepted.

Coalescence by formation of a void sheet arises from the nucleation of smaller – but numerous – secondary voids oriented following a shear band localization between two larger and distant voids (Fig. 1b and 4c). Cox and Low (1974) presented their classical result for a tensile test of an AISI 4340 steel (Fig. 5c). In their experiment, metallography analyses led to the conclusion that larger voids were nucleated firstly at manganese sulfide particles. These voids enlarged until a critical point from which smaller particles of carbides started to nucleate in the narrow band between the larger voids. Although these secondary voids were much smaller, they were numerous enough so that a void sheet could be formed by a dense arrangement of microvoids. At the final stage of their experiment, this void sheet linked the initial two larger voids and then created a macrocrack. The formation of microscopic shear band localization in single crystals was further investigated by Asaro (1979) and Pegel et al. (1980). Later, Moody and Greulich (1985) also observed a formation

of slip band fracture by void sheet coalescence of carbides in a Fe-Ni-Co superalloy.

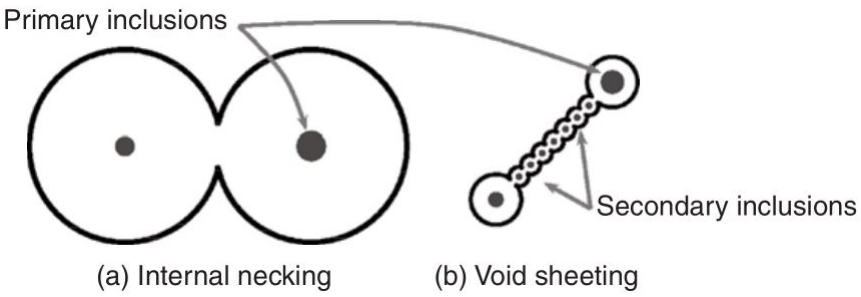

Figure 1: An illustration of the coalescence mechanisms by *internal necking* and by *void sheeting*.

In Fig. 1a, two voids become linked due to their enlargement until their boundaries collapse by forming only one larger void. In Fig. 1b, two larger and more distant voids become jointed by the nucleation of smaller voids aligned with a shear band. Source: (BESSON, 2010).

Necklace (also known as *coalescence in columns*) is a peculiar coalescence mechanism discovered by Benzerga (2000). He observed a formation of vertical void sheets in uniaxial loading tests of steel specimens. Differently to the microshear bands, these sheets resulted from the alignment of elongated manganese sulfide particles following the loading axis direction. Consequently, these voids continued to become even more elongated throughout the increase of the load level until such a point that, even though the particular volume fraction of each void was small, the voids were linked due to the coincidence of intense elongation of them in the same "columns" (i.e. loading axis direction). This mechanism was also perceived in uniaxially loaded steel notched bars in Benzerga, Besson and Pineau (2004).

Finally, coalescence by intergranular fracture consists of a microcrack propagation by adjacent particle interfaces. Distinctly to internal necking, it is generally caused by a deficient resistance of the particle boundaries due to a chemical action of a hostile environment (DOWLING, 2013). Additionally, this mechanism also tends to occur in high strength aluminum alloys in which both the matrix and the particles themselves are too stiff compared to their interfaces (LUDTKA; LAUGHLIN, 1982).

2.1.4 Considerations about ductility

The influence of certain parameters on the ductility has been also assessed by several experimental and analytical–numerical studies. Increasing stress triaxialities (T, Eq. (2.1)) from the value of 1/3, were shown to decrease strain failure, according to numerous studies (e.g. (RICE; TRACEY, 1969) and (AGOGINO, 1978)). The specific value of $T = 1/3$ refers to the initial conditions of a uniaxial tensile test in round smooth bars (i.e. $\Sigma_2 = \Sigma_3 = 0$ in Eq. (2.1)), according to Benzerga and Leblond (2010).

The stress Lode parameter μ (defined in Eq. (2.2)) is found to also decrease ductility when its value approximates zero, which corresponds to a pure shear condition in the plane 1–3, according to Bao and Wierzbicki (2004), Barsoum and Faleskog (2007b), Barsoum and Faleskog (2007c), Barsoum and Faleskog (2007a), Barsoum and Faleskog (2011) and Barsoum, Faleskog and Pingle (2011). The reasons for this is still a matter of intense research.

$$T = \frac{\Sigma_m}{\Sigma_{eq}} = \frac{\dfrac{\Sigma_1 + \Sigma_2 + \Sigma_3}{3}}{\sqrt{\dfrac{1}{2}\left[(\Sigma_1 - \Sigma_2)^2 + (\Sigma_2 - \Sigma_3)^2 + (\Sigma_3 - \Sigma_1)^2\right]}} \in [-\infty, \infty] \tag{2.1}$$

$$\mu = \frac{2\Sigma_2 - \Sigma_1 - \Sigma_3}{\Sigma_1 - \Sigma_3} \in [-1, 1] \tag{2.2}$$

where Σ_1, Σ_2 and Σ_3 are the principal macroscopic stresses.

The influence of initial porosity (or equivalently volume fraction of particles) has been widely recognized as well. It is well-known that the increasing initial porosity causes decreasing failure strain. This conclusion was first reported in the experimental studies of Lentz (1978), Speich and Spitzig (1982) and Spitzig (1985). Then, Bourcier et al. (1986) dedicated a whole study to assess the effect of initial porosity on the fracture process of titanium alloys with different hardening behaviors. They concluded that the concentration of porosity in certain regions of their specimens led to localization-induced cracks.

The orientation of elongated particles was also a subject of investigation in the 1970s. Bernard, Grumbach and Moliexe (1975) and Wilson (1979) studied short-transverse ductility of steel plates and fatigue properties of a carbon plate steel A516–70, respectively. Their works agreed that the more an elongated void was transversely oriented to the rolling direction, the less ductile the materials became.

2.1.5 Reference values of critical porosities

The overall porosity $\bar{f}$ of a given material is defined as an estimation of the average of volume fraction of every void. Thus, it is reasonable to assume that a critical porosity $\bar{f}_c$ is related to the beginning of a coalescence process and, thus, to the final stage of ductile rupture itself.

Following this idea, estimations of $\bar{f}_c$ have been consistently proposed in the literature. Nowadays, there is consensus that, for most ductile rupture conditions, the critical porosity may vary in $\bar{f}_c \in [\approx 1\%, \approx 2\%]$, according to Marino, Mudry and Pineau (1985), Pardoen and Delannay (1998), Benzerga, Besson and Pineau (2004) and Benzerga, Besson and Pineau (2004).

2.2 Recent investigations

In the last 15 years, many efforts have been devoted to better explaining some inconsistencies between experimental observations regarding ductile failure in shear-dominated loadings (i.e. $-1/3 \leq T \leq 1/3$ and $\mu \approx 0$). The classical works that performed tensile tests, generally on round smooth or notched bars, assured that the failure strain decreases for increasing stress triaxialities T from 1/3 on (e.g. the work of Hancock and Mackenzie (1976)). These results are in agreement with the predictions provided by the analytical work of Rice and Tracey (1969). Additionally, in the 1980s, Johnson and Cook (1985) found that ductility continued to increase with decreasing positive triaxialities below $T = 1/3$.

However, Bao and Wierzbicki (2004) obtained a very different outcome from a series of tests on a 2024-T351 aluminum alloy. They found that the ductility *decreased* for decreasing triaxialities below $T \approx 1/3$ and that it reached a minimum in the vicinities of the level $T = 0$. Notwithstanding, the ductility then increased quickly for decreasing values of $T \leq 0$, as illustrated in Fig. 2.

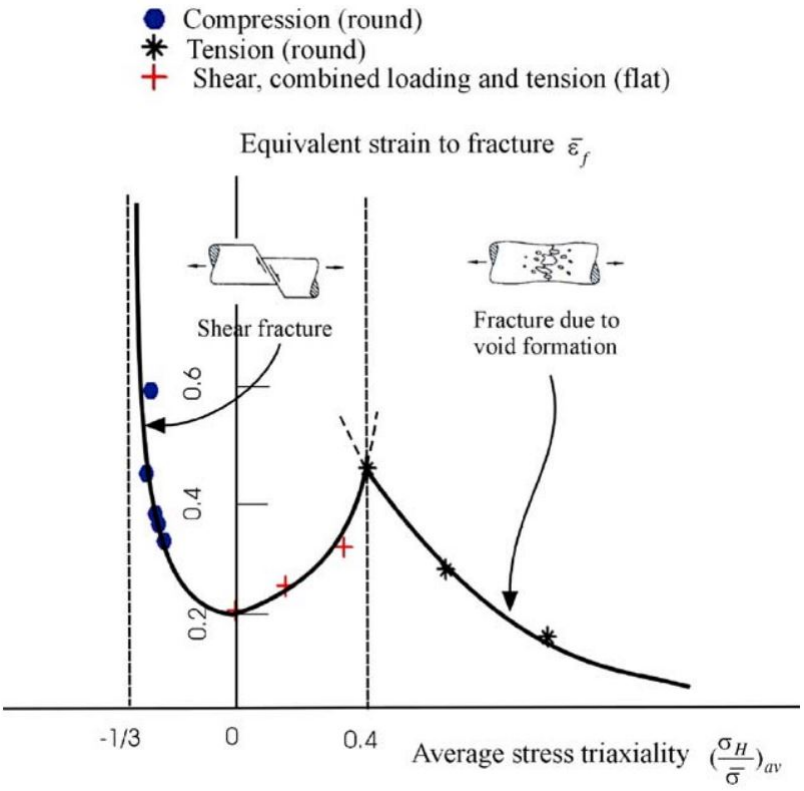

Figure 2: The relation between fracture strain and stress triaxiality for tests on a 2024-T351 aluminum alloy.

For a decreasing stress triaxiality T, Bao and Wierzbicki (2004) obtained (i) an increasing ductility until $T \approx 0.4$; (ii) a decreasing ductility until it reached a minimum level at $T \approx 0$; and a rapidly increasing ductility for $-1/3 \leq T \leq 0$. Source: (BAO; WIERZBICKI, 2004).

The scientific community promptly proposed some explanations. Teng and Wierzbicki

(2006) proposed that (i) a void growth mechanism should prevail in the region $T \geq 1/3$ and (ii) a shear-decohesion should predominantly occur for $T < 1/3$. Later, Barsoum and Faleskog (2007b), Barsoum and Faleskog (2007c) and Barsoum and Faleskog (2011) proposed that ductile fracture should be developed by a combination of the mechanisms of *intervoid necking* (Fig. 4a and 5a) and *intervoid shearing* (Fig. 4b and 5b).

Nevertheless, more inconsistencies have been continually reported in the present decade. For example, Ghahremaninezhad and Ravi-Chandar (2013) obtained a shear-dominated failure mode on a 6061-T6 aluminum alloy that apparently did not involve any influence of coalescence of voids. Additionally, increasing ductility related to a decreasing stress triaxiality was observed by Ghahremaninezhad and Ravi-Chandar (2012), Ghahremaninezhad and Ravi-Chandar (2013), Haltom, Kyriakides and Ravi-Chandar (2013) and Scales, Tardif and Kyriakides (2016).

The interaction between coalescence and localization phenomenon was investigated by Tekoğlu, Hutchinson and Pardoen (2015). They performed 3D FEM calculations on an elastoplastic periodic cell to find out whether these two mechanisms occurred simultaneously. They concluded that (i) for increasing stress triaxialities, coalescence and localization tend not to occur at the same time; and (ii) for triaxialities near zero, these mechanisms tend to occur simultaneously.

The influence of the Lode parameter on the evolution of porosity in ductile materials was studied by Danas and Ponte Castañeda (2012). They used a second order nonlinear homogenization method of Ponte Castañeda (2002a) to obtain the effective response of porous materials under different loading conditions. They remarked that the effect of the Lode parameter μ is more significant at the evolution of porosity than at the effective yield surfaces. Moreover, their results showed that the lowest failure strain coincided with a Lode parameter $\mu = 1$, while no void collapse was observed for the axisymmetric condition of $\mu = -1$. However, Hutchinson and Tvergaard (2012) argued that 3D FEM calculations – as in Bao and Wierzbicki (2004) – indicate that the minimum ductility should not coincide with $\mu = 1$. According to them, some analytical considerations in Danas and Ponte Castañeda (2012) could have erroneously influenced this result.

Dunand and Mohr (2014) performed several 3D FEM analysis of periodic cells – including contact and large strain theory – to assess the influence of the Lode angle on the localization at low triaxialities. Some of their results are shown in Fig. 3. Each black dot in this figure represents a proportional loading, keeping constant both stress triaxiality and Lode angle, that led the cell to a localization pattern. They found that the failure strain is a convex function of both the stress Lode angle and triaxiality. Besides, Fig. 3 reveals that the localization phenomenon does not occur for stress triaxialities approximately in the range of $T \in [0, 0.18]$. Furthermore, for around $T \in [0.18, 0.6]$, the development of localization relies on a specific variation of the Lode angle as a function of the triaxiality.

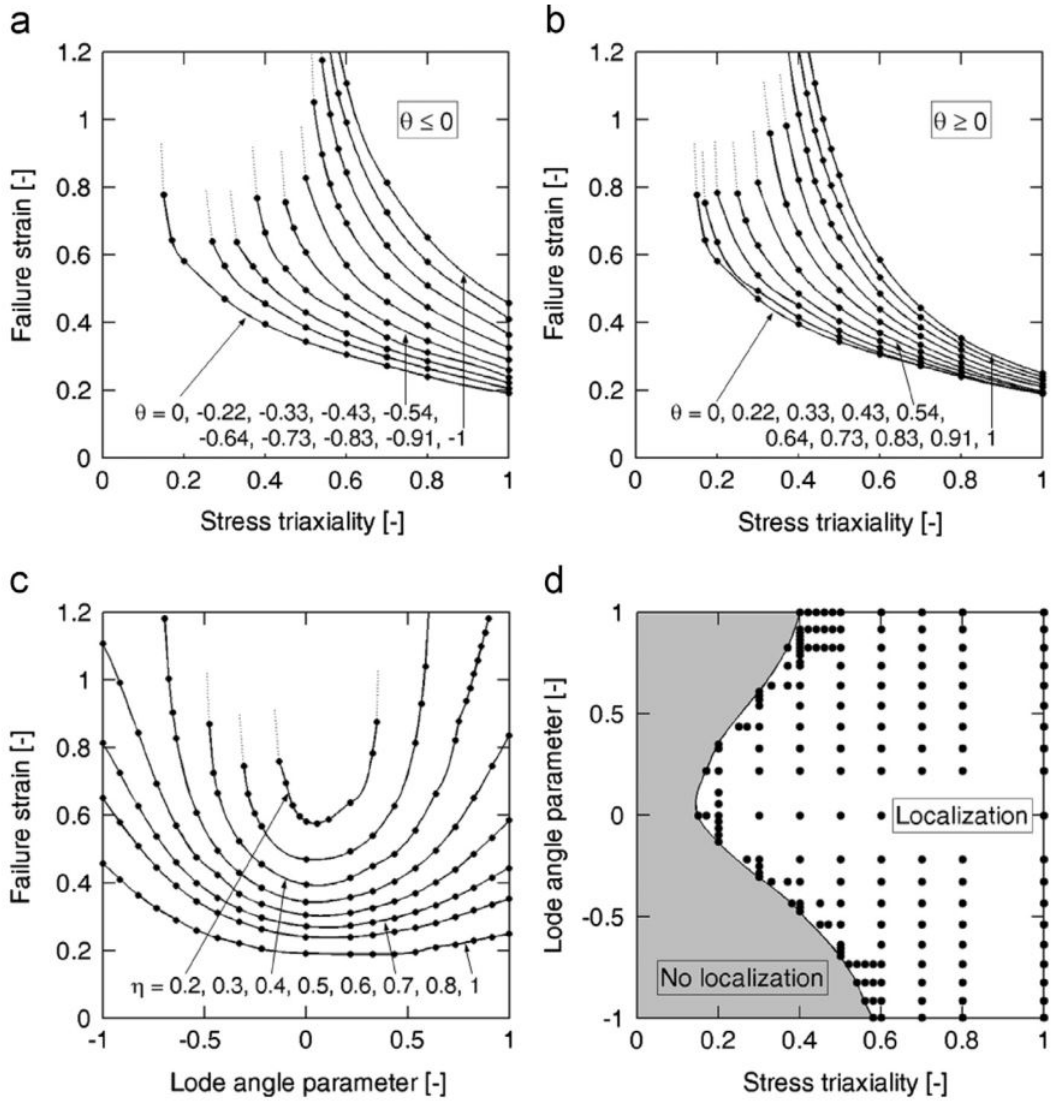

Figure 3: Failure strain associated to the occurrence of plastic localization as function of the stress triaxiality η and the stress Lode angle θ, according to Dunand and Mohr (2014).

Each black dot corresponds to a 3D FEM calculation of a periodic porous material under a proportional loading that led the cell to a failure due to localization. Note: Due to different nomenclatures in their manuscript, η represents the stress triaxiality T, while θ to the stress Lode angle Θ. Source: (DUNAND; MOHR, 2014)

In a very recent work, Noell, Carroll and Boyce (2018) proposed an extended group of seven mechanisms that should play a role in different ductile rupture conditions. According to them, these mechanisms may not only compete with one another – as in the sense of Barsoum's view –, but they may facilitate the occurrence of other ones. Moreover, these mechanisms can also work sequentially in a progressive load to rupture of a material. These mechanisms are illustrated by schematic representations, in Fig. 4, and by experimental observations provided by the literature in Fig 5. Since Noell, Carroll and Boyce (2018) limited their experimental investigations to high-purity copper, nickel and aluminum, further works are required to validate their hypothesis to structural engineering

materials and high-strength alloys.

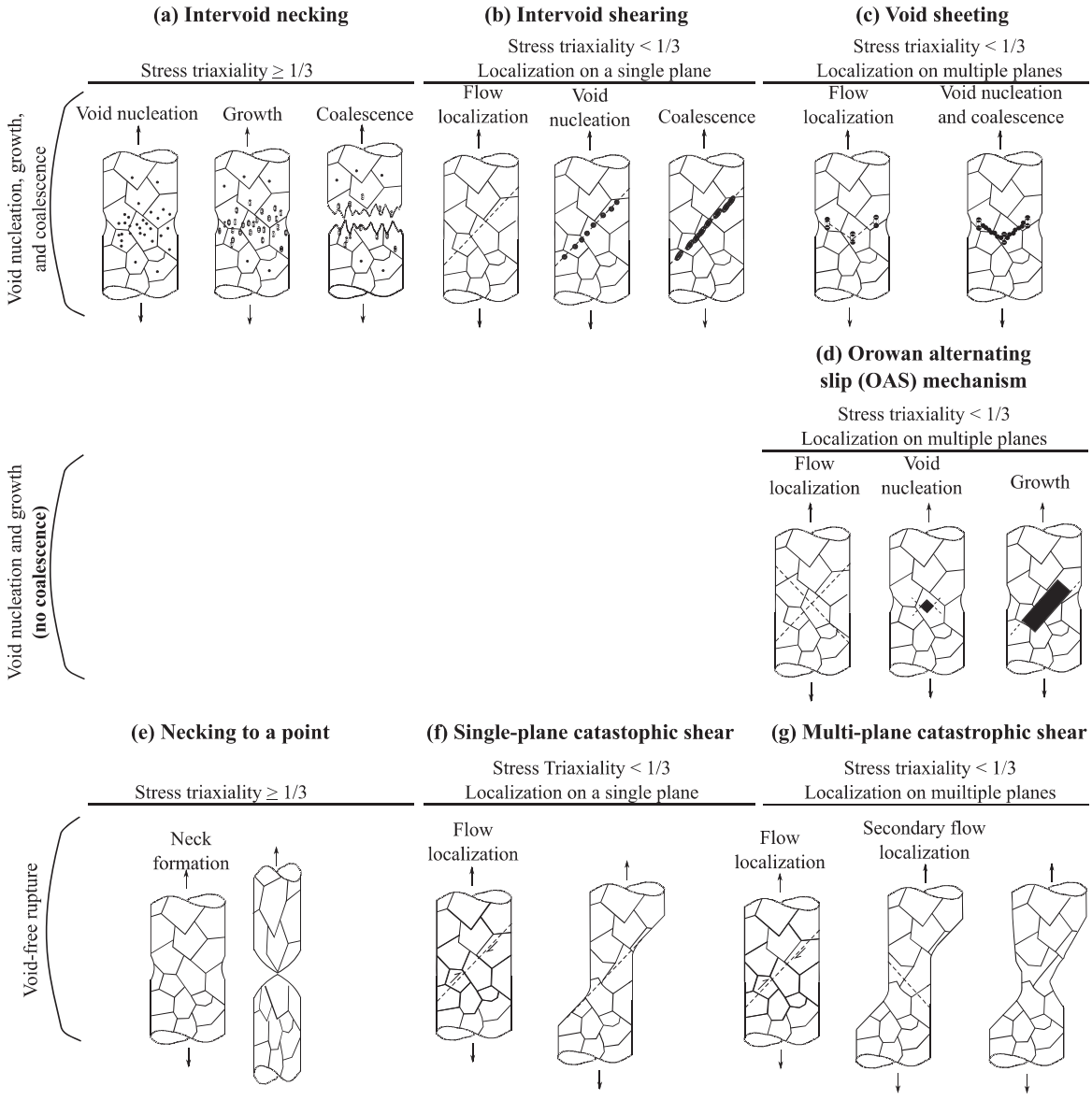

Figure 4: A schematic illustration of the seven mechanisms of ductile rupture proposed by Noell, Carroll and Boyce (2018).

Coalescence-based mechanisms: (a) coalescence by adjacent enlarged voids until their boundaries collapse into a larger unique void; (b) coalescence by a nucleation of small voids that are aligned to a shear band localization; and (c) linkage of two larger voids by the nucleation of smaller and numerous ones following the direction of one or more shear bands. Coalescence-free mechanism: (d) in the Orowan Alternating Splip (OAS) mechanism, groups of voids are nucleated in the vicinities of the crossing points of two slip bands and then proceed to grow (no coalescence). Void-free mechanisms: (e) rupture by necking to a point; (f) rupture by slipping along a shear localization band; and (g) rupture by slipping along multiple shear localization bands. Source: (NOELL; CARROLL; BOYCE, 2018).

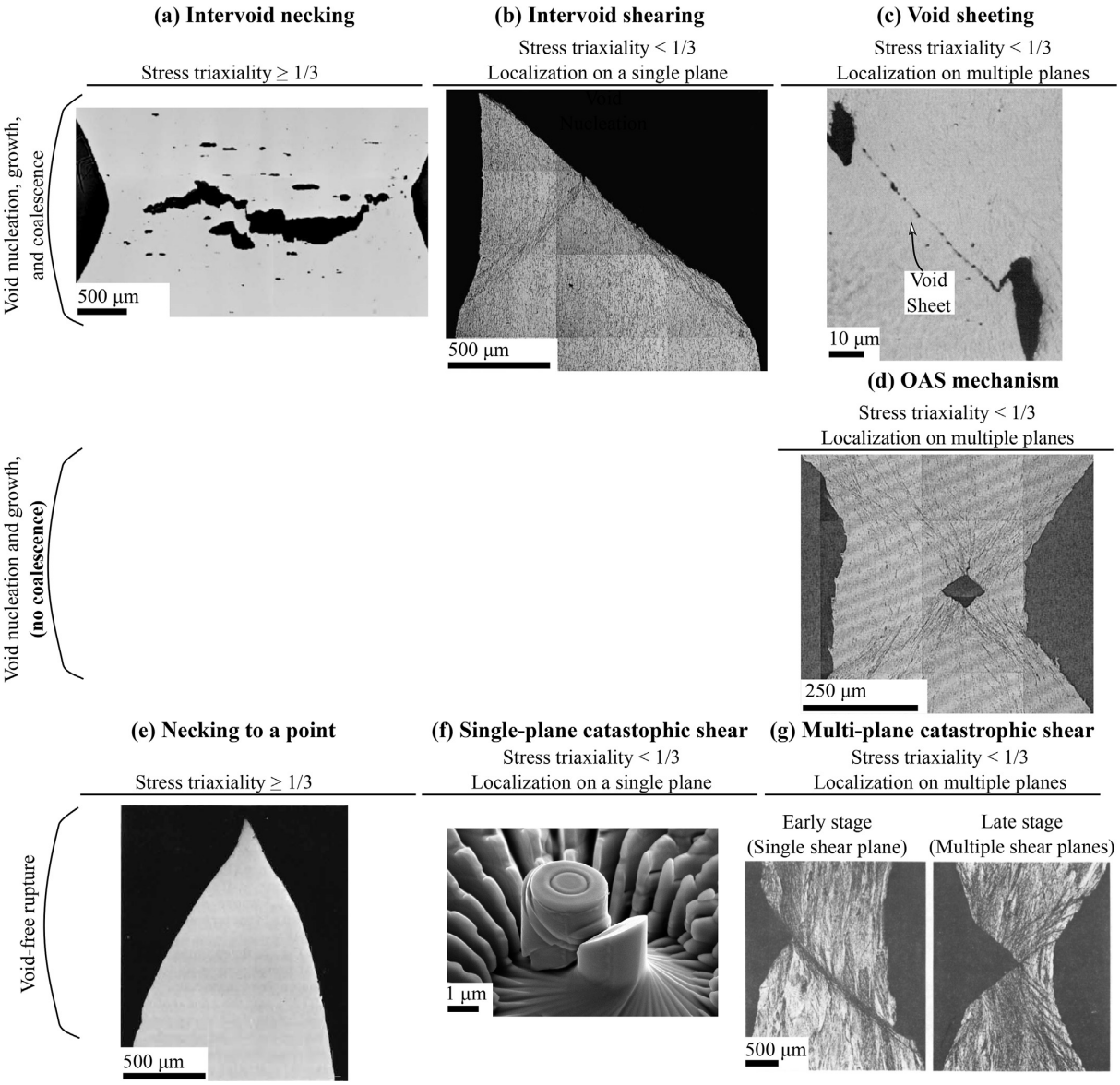

Figure 5: Illustrations of the seven mechanisms of Noell, Carroll and Boyce (2018) of ductile rupture by SEM images presented by the literature.

Coalescence-based mechanisms: (a) intervoid necking (BENZERGA; BESSON; PINEAU, 2004); (b) intervoid shearing (SPENCER; CORBIN; LLOYD, 2002); and (c) Void sheeting (COX; LOW, 1974). Coalescence-free mechanism: (d) OAS mechanism (SPENCER; CORBIN; LLOYD, 2002). Void-free mechanisms: (e) necking to a point (CHIN; HOSFORD; BACKOFEN, 1964 apud NOELL; CARROLL; BOYCE, 2018); (f) Slipping along a shear band (SHARON et al., 2014 apud NOELL; CARROLL; BOYCE, 2018); and (g) Slipping along multiple shear bands (WEINRICH; FRENCH, 1976). Source: (NOELL; CARROLL; BOYCE, 2018).

3 ISOTROPIC DUCTILE FRACTURE MODELING: THE GURSON MODEL AND ITS EXTENSIONS

This chapter describes some of the most relevant models for isotropic ductile fracture. The first one is the acclaimed Gurson model, which was proposed by Gurson (1975) (in his doctoral dissertation) and then by Gurson (1977) (in a scientific paper). Basically, he combines the averaging homogenization technique with the kinematic approach of Limit Analysis theorem to analytically formulate a continuum constitutive model for porous ductile materials that couples yield criterion and damage evolution. Since then, several extensions of this model – some purely phenomenological and other numerical/analytical – have been proposed in order to overcome some of its limitations. Among these, some of the most important work to the field, and also useful to the understanding of the contributions of this doctoral dissertation, are hereby presented. Moreover, the basic concepts about the averaging homogenization technique and the notations used throughout this document – not only in this chapter – are resumed in the first section.

3.1 Preliminaries

3.1.1 Tensorial and matrix algebra notations

Throughout this document, most mathematical expressions are written following an intrinsic or index tensorial notation. Scalar quantities are represented by regular weight letters (e.g. α, λ, r, R). First and second-order tensors are referred to in bold letters (e.g. $\boldsymbol{\sigma}$, $\boldsymbol{\dot{\epsilon}}$, $\boldsymbol{\dot{E}}$). Their precise orders are indicated in the text and may also be inferred by the context. Fourth-order tensors are written in cursive letters (e.g. $\mathbb{L}$, $\mathbb{C}$).

Whenever needed, additional notation is also used in some sections in order to avoid ambiguities between matrices and vectors. A matrix algebra notation is then conveniently adopted in certain sections concerning aspects of numerical implementation. According to this notation, a scalar variable is still represented by regular letters (e.g. C, λ, η). However, vectors and matrices are still written in bold, but hold respectively one and two underlines (e.g. vectors are $\underline{\boldsymbol{\dot{\epsilon}}}$, $\underline{\boldsymbol{\dot{\kappa}}}$, while matrices are $\underline{\underline{\boldsymbol{L}}}$, $\underline{\underline{\boldsymbol{C}}}$).

The numerical implementation of products involving symmetric high-order tensors requires an equivalent matrix algebra representation so that the unnecessary operations are avoided. For this purpose, the well-known *Voigt notation* is used in order to conveniently treat tensor operations as matrix–vector relations. Some details about this notation are given in Appendix A.

3.1.2 A brief overview of the averaging homogenization technique

In general terms, homogenization techniques offer approaches for modeling heterogeneous media (i.e. consisting of more than one material) by defining an equivalent, but hypothetical, homogeneous medium. However, in most engineering materials, the heterogeneities are arbitrarily distributed on microscale, which does not allow that every heterogeneity be accounted for. In order to avoid this inconvenience, Hill (1963) proposed that a heterogeneous medium could be consistently represented by its smallest material portion that contains every relevant property of the material. This portion is commonly called *Representative Volume Element* (RVE) or *Representative Elementary Volume* (REV). According to Besson et al. (2010), the validity of this idealization is guaranteed for most cases if the characteristic lengths (i) l_{RVE} of the RVE; (ii) l_{struct} of the engineering structure to be modeled; and (iii) l_{load} of the load fluctuations applied to the final structure satisfy

$$\begin{aligned} l_{RVE} &\ll l_{struct} \\ l_{RVE} &\ll l_{load}. \end{aligned} \tag{3.1}$$

Based on the RVE concept, the equivalence between the real heterogeneous material (represented by the RVE) and the fictitious homogeneous one is achieved by averaging the microscopic (i.e. pointwise in the RVE) stress and strain fields in the domain Ω – including heterogeneities, voids, inclusions – (Fig. 6). These averaged tensors are then assumed to be those of the hypothetical homogeneous material. The average of a *statically admissible* (i.e. equilibrated) microscopic stress field $\boldsymbol{\sigma}^*$ in the domain Ω of the RVE is

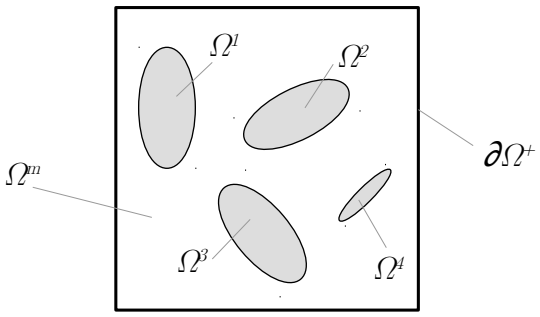

Figure 6: An illustration of an arbitrary RVE containing four heterogeneities.

The illustrated RVE contains four arbitrary heterogeneities enumerated from 1 to 4. The material matrix is represented by Ω^m, while Ω^i represents the interior of the i-th heterogeneity. The boundary $\partial\Omega^+$ denotes the outer surface of the RVE. The total domain Ω is defined as $\Omega = \Omega^m \cup \Omega^1 \cup \Omega^2 \cup \Omega^3 \cup \Omega^4$. This RVE representation is taken as two-dimensional for the sake of simplicity and distinctness. However, the RVEs used in the next sections of this document are assumed to be three-dimensional, as will be indicated later on. Source: the author.

$$< \boldsymbol{\sigma} >= \frac{1}{V} \int_{\Omega} \boldsymbol{\sigma} dV. \tag{3.2}$$

Equivalently, the average of a kinematically admissible (i.e. continuous and derived from velocity field that respects the essential boundary conditions) strain rate field $\dot{\boldsymbol{\epsilon}}$ in Ω is

$$< \dot{\boldsymbol{\epsilon}} >= \frac{1}{V}\int_{\Omega} \dot{\boldsymbol{\epsilon}} dV. \tag{3.3}$$

The integrals in Eq. (3.2) and (3.3) can be equivalently evaluated in the external boundary $\partial\Omega^+$ by using the Divergence Theorem. For this, one must also verify that, considering no volume forces and small strains theory,

$$(\sigma_{ik}x_j)_{,k} = \sigma_{ik,k}x_j + \sigma_{ik}x_{j,k} = \sigma_{ij}$$

and

$$\epsilon_{ij} = \frac{1}{2}(\dot{u}'_{i,j} + \dot{u}_{j,i}).$$

The Eq. (3.2) and (3.3) can be then transformed into

$$< \boldsymbol{\sigma} >_{ij}= \frac{1}{V}\int_{\Omega} \sigma_{ij} dV = \frac{1}{V}\int_{\Omega} (\sigma_{ik}x_j)_{,k} dV = \frac{1}{V}\int_{\partial\Omega^+} \sigma_{ik}x_k n_j dS \tag{3.4}$$

and

$$< \dot{\boldsymbol{\epsilon}} >_{ij}= \frac{1}{V}\int_{\Omega} \dot{\boldsymbol{\epsilon}}_{ij} dV = \frac{1}{V}\int_{\Omega} \frac{1}{2}(\dot{u}_{i,j} + \dot{u}_{j,i}) dV = \frac{1}{2V}\int_{\partial\Omega^+} (\dot{u}_i n_j + \dot{u}_j n_i) dS. \tag{3.5}$$

where $\boldsymbol{n}(\boldsymbol{x})$ is the normal unitary vector to the outer surface $\partial\Omega^+$ at the point $\boldsymbol{x} \in \partial\Omega^+$.

Although the averaging process is straightforward, an equally important – but more complicated – task is the definition of the boundary conditions to the RVE problem. These boundary conditions must represent as accurately as possible the actual situation in which the microscopic portion of material is subjected. However, it is a very complex task due to the arbitrary distribution of the heterogeneities and the impossibility of determining the precise stress and strain field acting on the planes of interaction between two material portions. Two idealizations regarding these questions were then proposed by Hill (1963): (i) uniform *stress* field on the external boundary $\partial\Omega^+$ (Eq. (3.6)); and (ii) uniform *strain* field on the external boundary $\partial\Omega^+$ (Eq. (3.7)).

$$\boldsymbol{F}^d(\boldsymbol{x}) = \boldsymbol{\Sigma} \cdot \boldsymbol{n}(\boldsymbol{x}) \quad \boldsymbol{x} \in \partial\Omega^+, \tag{3.6}$$

where $\boldsymbol{F}^d(\boldsymbol{x})$ is the traction vector applied at $\boldsymbol{x} \in \partial\Omega^+$ and $\boldsymbol{\Sigma}$ is a uniform (i.e. constant) *macroscopic* stress tensor applied on $\partial\Omega^+$.

$$\dot{\boldsymbol{u}}^d(\boldsymbol{x}) = \dot{\boldsymbol{E}} \cdot \boldsymbol{x} \quad \boldsymbol{x} \in \partial\Omega^+ \tag{3.7}$$

where $\dot{\boldsymbol{u}}^d(\boldsymbol{x})$ is the velocity vector at $\boldsymbol{x} \in \partial\Omega^+$ and $\dot{\boldsymbol{E}}$ is a uniform (i.e. constant) *macroscopic* strain rate tensor applied on $\partial\Omega^+$.

These two types of boundary conditions lead to relevant conclusions. The first one is that the boundary condition of uniform stress implies the average $< \boldsymbol{\sigma} >$ to equal the applied macroscopic stress $\boldsymbol{\Sigma}$. Similarly, the second one is that uniform strain in $\partial\Omega^+$ causes $< \dot{\boldsymbol{\epsilon}} >= \dot{\boldsymbol{E}}$. These two results can save computational effort in numerical implementations involving one of these assumptions. They can also be easily verified by considering Eq. (3.4) and (3.5).

The strain energy density may also be conveniently averaged in the domain of the RVE. Thanks to the Hill-Mandel lemma ((HILL, 1967) and (MANDEL, 1972 apud ZAOUI, 2002)), the average strain energy density can be equivalently evaluated as

$$< \boldsymbol{\sigma} : \dot{\boldsymbol{\epsilon}} >=< \boldsymbol{\sigma} >:< \dot{\boldsymbol{\epsilon}} > . \tag{3.8}$$

Throughout this document, the adjective *macroscopic* indicates that a certain field (stress and strain rate) is *averaged* in the domain Ω of an RVE, even though its precise meaning is related to uniform fields that are imposed as boundary conditions on $\partial\Omega$. Additionally, the term *effective* is also used by meaning *averaged*.

3.1.3 Microscopic quantities

In the present text, the microscopic stress tensor is represented by $\boldsymbol{\sigma}$. This tensor is conveniently decomposed in terms of its three stress invariants: (i) the hydrostatic (or *mean*) stress σ_m; (ii) the von Mises (or *equivalent*) measure of stress σ_{eq}; and (iii) the Lode angle ω. The microscopic stress tensor can then be written as

$$\boldsymbol{\sigma} = \sigma_{eq}\boldsymbol{e}'(\omega) + \sigma_m\mathbf{1}, \tag{3.9}$$

where

$$\sigma_m = \frac{1}{3}\operatorname{Tr}\boldsymbol{\sigma}, \tag{3.10}$$

$$\boldsymbol{\sigma}' = \boldsymbol{\sigma} - \sigma_m\mathbf{1}, \tag{3.11}$$

$$\sigma_{eq} = \sqrt{\frac{3}{2}\boldsymbol{\sigma}' : \boldsymbol{\sigma}'}, \tag{3.12}$$

$$\boldsymbol{e}'(\omega) = \begin{bmatrix} \cos\omega & 0 & 0 \\ 0 & \cos\left(\omega - \frac{2\pi}{3}\right) & 0 \\ 0 & 0 & \cos\left(\omega + \frac{2\pi}{3}\right) \end{bmatrix}, \tag{3.13}$$

$$\omega = \frac{1}{3}\arccos\left(\frac{27}{2}\frac{\det \boldsymbol{\sigma}'}{\sigma_{eq}^3}\right) \tag{3.14}$$

and $\mathbf{1}$ is the identity matrix of order three.

Similarly, the microscopic strain rate $\dot{\boldsymbol{\epsilon}}$ is hereby written in terms of its three invariants: (i) the hydrostatic (or mean) strain rate $\dot{\epsilon}_m$; (ii) the equivalent measure of strain $\dot{\epsilon}_{eq}$; and (iii) the Lode angle ξ as

$$\dot{\boldsymbol{\epsilon}} = \dot{\epsilon}_{eq} e' + \dot{\boldsymbol{\epsilon}}_m \mathbf{1}, \tag{3.15}$$

where

$$\dot{\epsilon}_m = \frac{1}{3}\operatorname{Tr}\dot{\boldsymbol{\epsilon}}, \tag{3.16}$$

$$\dot{\boldsymbol{\epsilon}}' = \dot{\boldsymbol{\epsilon}} - \dot{\epsilon}_m \mathbf{1} \tag{3.17}$$

$$\dot{\epsilon}_{eq} = \sqrt{\frac{3}{2}\dot{\boldsymbol{\epsilon}}' : \dot{\boldsymbol{\epsilon}}'}, \tag{3.18}$$

$$\boldsymbol{e}' = \begin{bmatrix} \cos\xi & 0 & 0 \\ 0 & \cos\left(\xi - \frac{2\pi}{3}\right) & 0 \\ 0 & 0 & \cos\left(\xi + \frac{2\pi}{3}\right) \end{bmatrix}, \tag{3.19}$$

$$\xi = \frac{1}{3}\arccos\left(\frac{4\det \dot{\boldsymbol{\epsilon}}'}{\dot{\epsilon}_{eq}^3}\right) \tag{3.20}$$

As the following chapters deal with incompressible material matrices, the hydrostatic strain rate is nulled in the equations above (i.e $\dot{\epsilon}_m = 0$).

3.1.4 Macroscopic quantities

The macroscopic stress and strain rate are represented by $\boldsymbol{\Sigma}$ and $\dot{\boldsymbol{E}}$, respectively. Analogously to the previous subsection, the macroscopic stress is defined in terms of its invariants (i) macroscopic hydrostatic stress Σ_m (or, equivalently, the macroscopic stress triaxiality $T \in [-\infty, \infty]$); (ii) the deviatoric macroscopic stress; (iii) von Mises (or equivalent) macroscopic stress Σ_{eq}; and (iv) the macroscopic stress Lode angle Θ:

$$\begin{aligned} \boldsymbol{\Sigma} &= \frac{2}{3}\Sigma_{eq} e'(\Theta) + \Sigma_m \mathbf{1} \\ &= \Sigma_{eq}\left[\frac{2}{3}e'(\Theta) + T\mathbf{1}\right] \end{aligned} \tag{3.21}$$

where

$$\Sigma_m = \frac{1}{3}\,\mathrm{Tr}\,\boldsymbol{\Sigma}, \tag{3.22}$$

$$\boldsymbol{\Sigma}' = \boldsymbol{\Sigma} - \Sigma_m \mathbf{1}, \tag{3.23}$$

$$\Sigma_{eq} = \sqrt{\frac{3}{2}\boldsymbol{\Sigma}' : \boldsymbol{\Sigma}'}, \tag{3.24}$$

$$\boldsymbol{e}'(\Theta) = \begin{bmatrix} \cos\Theta & 0 & 0 \\ 0 & \cos\left(\Theta - \frac{2\pi}{3}\right) & 0 \\ 0 & 0 & \cos\left(\Theta + \frac{2\pi}{3}\right) \end{bmatrix}, \tag{3.25}$$

$$T = \frac{\Sigma_m}{\Sigma_{eq}} \tag{3.26}$$

and

$$\Theta = \frac{1}{3}\arccos\left(\frac{27}{2}\frac{\det\boldsymbol{\Sigma}'}{\Sigma_{eq}^3}\right) \tag{3.27}$$

Finally, the macroscopic strain rate tensor $\dot{\boldsymbol{E}}$ is also described as a function of its three invariants: (i) hydrostatic strain rate $\dot{E}_m$ (or, equivalently, the triaxiality $H \in [-\infty, \infty]$); (ii) the deviatoric macroscopic strain rate; (iii) equivalent measure $\dot{E}_{eq}$; and (iv) its Lode angle η as follows:

$$\begin{aligned} \dot{\boldsymbol{E}} &= \dot{E}_{eq} e'(\eta) + \dot{E}_m \mathbf{1} \\ &= \dot{E}_{eq}\left[e'(\eta) + H\mathbf{1}\right] \end{aligned} \tag{3.28}$$

where

$$\dot{E}_m = \frac{1}{3}\,\mathrm{Tr}\,\dot{\boldsymbol{E}}, \tag{3.29}$$

$$\dot{\boldsymbol{E}}' = \dot{\boldsymbol{E}} - \dot{E}_m \mathbf{1}, \tag{3.30}$$

$$\dot{E}_{eq} = \sqrt{\frac{2}{3}\dot{\boldsymbol{E}}' : \dot{\boldsymbol{E}}'}, \tag{3.31}$$

$$\boldsymbol{e}'(\eta) = \begin{bmatrix} \cos\eta & 0 & 0 \\ 0 & \cos\left(\eta - \frac{2\pi}{3}\right) & 0 \\ 0 & 0 & \cos\left(\eta + \frac{2\pi}{3}\right) \end{bmatrix}, \tag{3.32}$$

$$H = \frac{\dot{E}_m}{\dot{E}_{eq}} \tag{3.33}$$

and

$$\eta = \frac{1}{3}\arccos\left(\frac{4\det\dot{\boldsymbol{E}}'}{\dot{E}_{eq}^3}\right) \tag{3.34}$$

3.1.5 Graphical representation of macroscopic yield surfaces

In order to avoid representing the yield surface in three-dimensional plots, it is preferable to benefit from the intersection of the surface with certain planes that hold fundamental concepts from Mechanics of Materials. The first is called *deviatoric plane* (or even π-*plane* or *Nadai's plane*). It consists of an intersection of the yield surface with a plane that is orthogonal to the hydrostatic axis for a prescribed value $\Sigma_m = \bar{\Sigma}_m$, as Fig. 7 illustrates for a hypothetical yield stress.

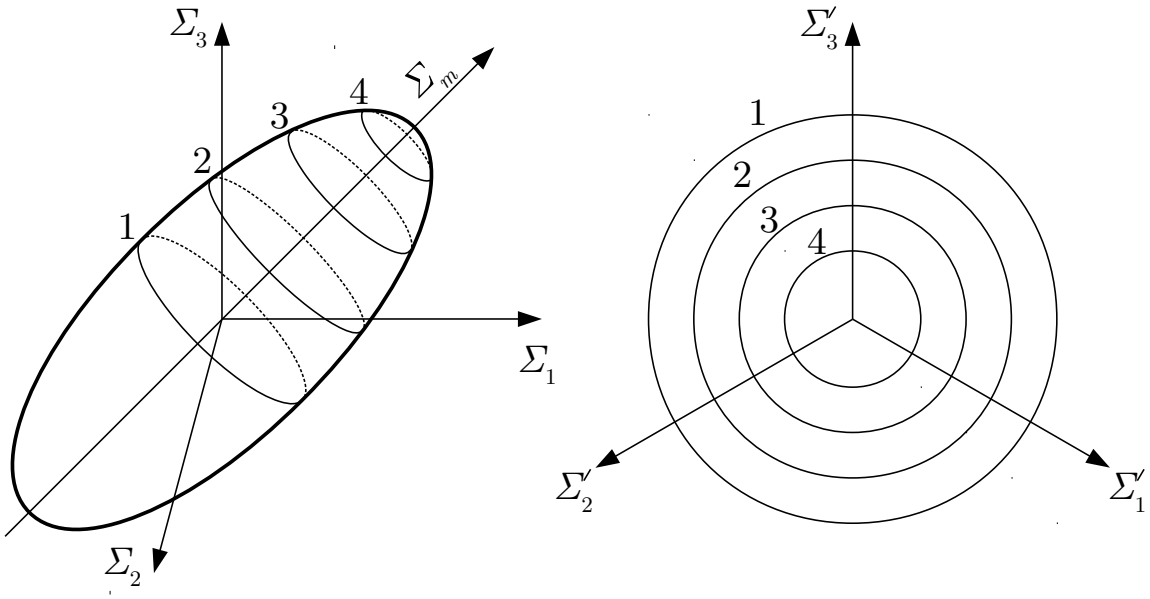

Figure 7: Illustration of the meaning of deviatoric planes of macroscopic yield surfaces.

Source: the author.

The second useful family of planes is called *meridional planes*. A meridional plane, in the context of yield surfaces, corresponds to two given values of stress Lode angles: (i) $\Theta = \bar{\Theta}$ to obtain a semi-plan; and (ii) $\Theta = \bar{\Theta} + \pi$ to its complementary semi-plan. In Fig. 8, the prescription of $\Theta = \bar{\Theta}$ may be understood as the upper quadrants of the meridional curves ($\Sigma_{eq} \geq 0$); and $\Theta = \bar{\Theta} + \pi$, to $\Sigma_{eq} < 0$.

3.2 The Gurson Yield Criterion

In the 1970s, Gurson (1975) and Gurson (1977) formulated a model with the aim of describing isotropic ductile rupture by an adequate constitutive model to be implemented within recurrent engineering problems. His approach starts by conceiving two main RVE configurations: (i) a hollow sphere with a centered spherical cavity inside it; and (ii) a cylinder with an also aligned cylindrical void contained in it. The spherical RVE was

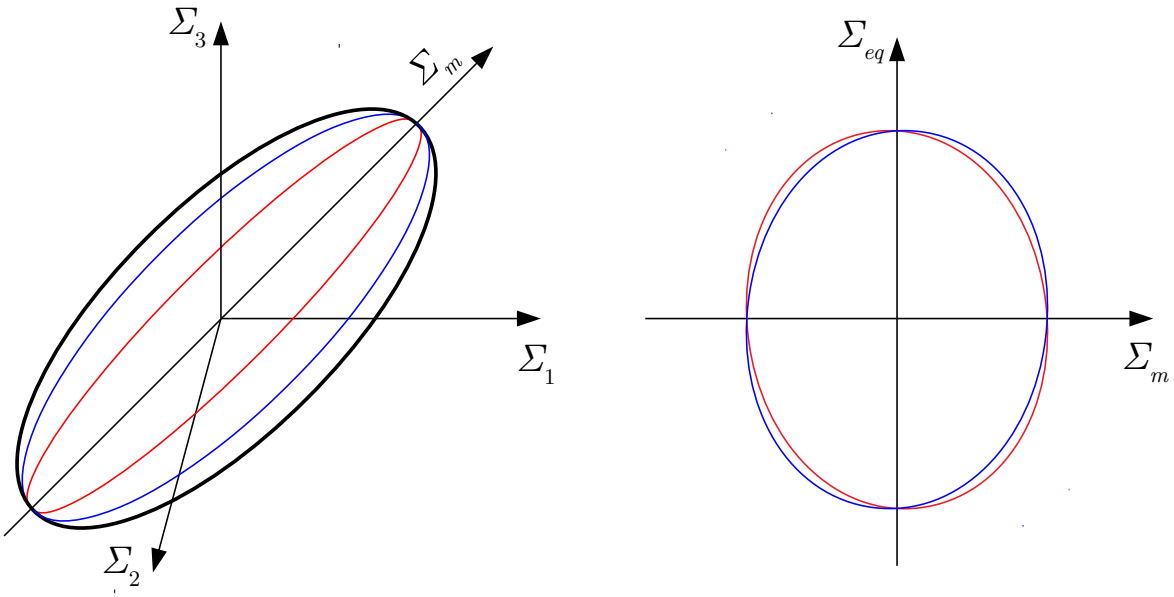

Figure 8: Illustration of the meaning of meridional planes of macroscopic yield surfaces.

Source: the author.

chosen to represent materials whose particles in microscale are arbitrarily distributed (i.e. macroscopic isotropy). The second RVE was taken to simulate materials whose defects in microscale are distributed with a preferred direction. Although both models were proposed in his doctoral dissertation, the spherical model has received much more attention in the literature. Accordingly, the present work explores only the spherical approach from here on.

The material matrix in a vicinity of the void is assumed to be continuous and (i) to follow von Mises criterion of plastification; (ii) to hold the normality rule for the plastic flow; (iii) not to present any hardening rule (i.e perfectly plastic material); and (iv) to undergo solely plastic deformation (i.e. rigid-plastic material). These assumptions are mathematically described by

$$\psi(\boldsymbol{\sigma}) = \sigma_{eq} - \sigma_0 \leq 0, \tag{3.35}$$

$$\dot{\boldsymbol{\epsilon}} = \dot{\boldsymbol{\epsilon}}^{pl} = \dot{\lambda}\frac{\partial \psi}{\partial \boldsymbol{\sigma}} \qquad \text{and} \tag{3.36}$$

$$\operatorname{Tr} \dot{\boldsymbol{\epsilon}} = 0, \tag{3.37}$$

where $\psi(\boldsymbol{\sigma}) \leq 0$ is the isotropic yield function, $\boldsymbol{\sigma}$ is the Cauchy stress tensor, σ_0 is the microscopic yield stress, σ_{eq} is the von Mises (or equivalent) stress, $\dot{\boldsymbol{\epsilon}}$ and $\dot{\boldsymbol{\epsilon}}^{pl}$ are respectively the total and the plastic microscopic strain rate tensor and $\dot{\lambda}$ is the microscopic plastic multiplier rate.

The radii of the inner (i.e. void) and the outer spheres are respectively represented by r_v and R (Fig. 9). The porosity parameter

$$f = \left(\frac{r_v}{R}\right)^3 \tag{3.38}$$

is defined as the ratio between the volumes of the cavity and the *total* volume occupied by the RVE. A point in Ω can be conveniently described by a spherical coordinate system, as depicted in Fig. 10.

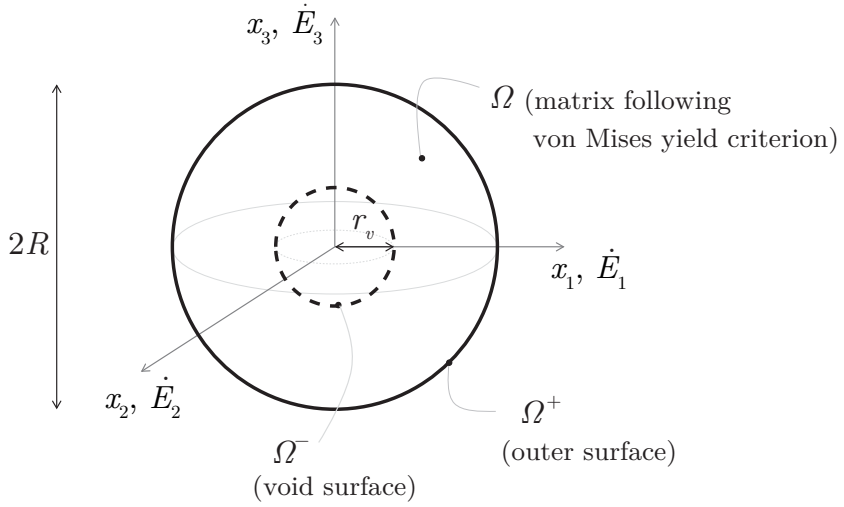

Figure 9: The Gurson's RVE chosen for modeling isotropic porous ductile materials.

The material matrix in Ω is assumed to follow the von Mises yield criterion. Source: the author.

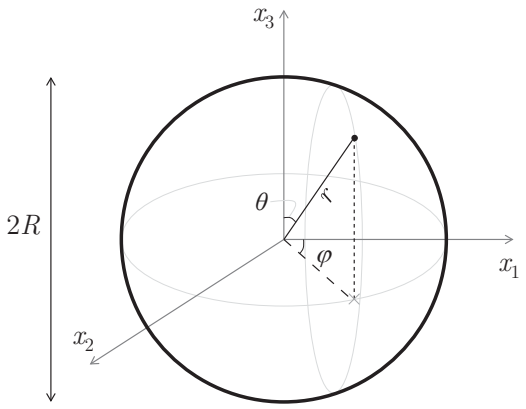

Figure 10: A spherical coordinate system whose origin coincides with the RVE center.

In this spherical coordinate system, r is the radius measured from the center of the RVE, $\varphi \in [0, 2\pi]$ is the azimuth angle and $\theta \in [0, \pi]$ is the zenith angle. Source: the author.

A uniform strain rate boundary condition is imposed on the outer surface $\partial\Omega^+$ in order to facilitate the choice of candidates to the trial strain rate field, as discussed

hereafter. The macroscopic strain rate $\dot{\boldsymbol{E}}$ is imposed in the external surface by the relation

$$\dot{\boldsymbol{u}} = \dot{\boldsymbol{E}} \cdot \boldsymbol{x}. \tag{3.39}$$

Additionally, the void surface requires another boundary condition. For this purpose, Gurson assumed that the void surface was traction-free. This assumption can be regarded as a uniform stress boundary condition in $\partial\Omega^-$:

$$\boldsymbol{F}^d(\boldsymbol{x}) = 0, \quad \boldsymbol{x} \in \partial\Omega^- \tag{3.40}$$

where $\boldsymbol{F}^d(\boldsymbol{x})$ is the traction vector on the void surface.

The microscopic dissipation potential π can then be defined as a function of a microscopic stress field $\boldsymbol{\sigma}$ and an traceless microscopic strain rate field $\dot{\boldsymbol{\epsilon}}$ as

$$\pi(\dot{\boldsymbol{\epsilon}}) = \sup_{\sigma \in \Upsilon} \{\boldsymbol{\sigma} : \dot{\boldsymbol{\epsilon}}\} \tag{3.41}$$

where $\Upsilon = \{\boldsymbol{\sigma} | \psi(\boldsymbol{\sigma}) =\leq \sigma_0\}$ is a convex set of statically admissible stress tensors $\boldsymbol{\sigma}$ and $\psi(\boldsymbol{\sigma})$ is homogenous of degree one.

The combination of the normality rule for the flow of the microscopic plastic strain rate $\dot{\boldsymbol{\epsilon}} = \dot{\lambda}\partial\psi/\partial\boldsymbol{\sigma}$ with the first degree homogeneity of the yield function $\psi(\boldsymbol{\sigma})$, Eq. (3.41) can be rewritten as

$$\pi(\dot{\boldsymbol{\epsilon}}) = \boldsymbol{\sigma} : \left(\dot{\lambda}\frac{\partial\psi}{\partial\boldsymbol{\sigma}}\right) = \dot{\lambda}\boldsymbol{\sigma} : \frac{\partial\psi}{\partial\boldsymbol{\sigma}} = \dot{\lambda}\psi(\boldsymbol{\sigma}) = \dot{\lambda}\sigma_0, \tag{3.42}$$

The evaluation of the plastic multiplier rate $\dot{\lambda}$ can be done in terms of a *kinematically admissible* (also called *compatible*) strain rate field $\dot{\boldsymbol{\epsilon}}$. According to this kinematic condition, the microscopic strain rate $\dot{\boldsymbol{\epsilon}}$ must respect the essential boundary condition, which is, in the Gurson's RVE problem, imposed on the outer surface (i.e. $\dot{\boldsymbol{\epsilon}}(R, \varphi, \theta) = \dot{\boldsymbol{E}}$). From Eq. (3.18) and (3.36), the plastic multiplier rate then satisfies

$$\dot{\lambda} = \frac{\dot{\epsilon}_{eq}}{\sqrt{\frac{2}{3}\frac{\partial\psi}{\partial\boldsymbol{\sigma}} : \frac{\partial\psi}{\partial\boldsymbol{\sigma}}}} = \frac{\dot{\epsilon}_{eq}}{\sqrt{\frac{2}{3}\left(\frac{3}{2}\frac{\boldsymbol{\sigma}'}{\sigma_{eq}}\right) : \left(\frac{3}{2}\frac{\boldsymbol{\sigma}'}{\sigma_{eq}}\right)}} = \frac{\dot{\epsilon}_{eq}\sigma_{eq}}{\sqrt{\frac{3}{2}\boldsymbol{\sigma}' : \boldsymbol{\sigma}'}} = \dot{\epsilon}_{eq}. \tag{3.43}$$

It follows from Eq. (3.42) and (3.43) that the microscopic plastic dissipation $\pi(\dot{\boldsymbol{\epsilon}})$ may thus be written in terms of only the compatible strain rate field $\dot{\boldsymbol{\epsilon}}'$ as

$$\pi(\dot{\boldsymbol{\epsilon}}) = \sigma_0\dot{\epsilon}_{eq} \tag{3.44}$$

and the macroscopic plastic dissipation potential is then derived by an average in the RVE volume as

$$\Pi = \frac{1}{V}\int_{\Omega} \sigma_0 \dot{\epsilon}'_{eq} dV. \tag{3.45}$$

The solution to the RVE (i.e. the velocity or strain rate field) can be obtained by a minimization of the macroscopic plastic dissipation potential Π in Eq. (3.45). However, this minimization procedure would result in too much of a complex description to use in common engineering situations.

Gurson (1975) then proposed that the solution could be approximated in a convenient way by carefully choosing a trial strain rate field $\dot{\boldsymbol{\epsilon}}_G$. This field would constitute an upperbound approximated solution to the minimization of Π based on kinematic theorem of Limit Analysis. It means that, by evaluating Π in Eq. (3.45) with a compatible $\dot{\boldsymbol{\epsilon}}'$ – but different to the exact solution $\dot{\boldsymbol{\epsilon}}$ – the resultant dissipation should be certainly greater than the exact dissipation calculated with $\dot{\boldsymbol{\epsilon}}$.

The Gurson's trial strain rate field $\dot{\boldsymbol{\epsilon}}_G$ relied on the contemporary results obtained by McClintock (1968a) and Rice and Tracey (1969). According to these authors, the ductile fracture is strongly dependent on the stress triaxiality. Gurson then idealized that the kinematically admissible velocity field $\dot{\boldsymbol{u}}_G$ could be decomposed into two parts. The first, $\dot{\boldsymbol{u}}_G^V$, should be the exact solution of a perfectly rigid-plastic hollow sphere under uniform external pressure. The second, $\dot{\boldsymbol{u}}_G^S$, should be an approximation of a velocity field that would only cause a shape change to the RVE. Their expressions in terms of the macroscopic strain rate $\dot{\boldsymbol{E}}$ and written in the spherical coordinate system depicted in Fig. 10 are

$$\dot{\boldsymbol{u}}_G^V = \dot{E}_m \frac{R^3}{r^2} \qquad \text{and} \tag{3.46}$$

$$\dot{\boldsymbol{u}}_G^S = \dot{\boldsymbol{E}}', \tag{3.47}$$

where $\dot{\boldsymbol{E}}' = \dot{\boldsymbol{E}} - \dot{E}_m \mathbf{1}$ is the macroscopic deviatoric strain rate and

$$\dot{\boldsymbol{u}}_G = \dot{\boldsymbol{u}}_G^V + \dot{\boldsymbol{u}}_G^S. \tag{3.48}$$

The compatibility equations from continuum mechanics allowed then to derive the acclaimed Gurson's trial velocity field by considering Eq. (3.48). Further details are given in Gurson (1975)

$$\dot{\boldsymbol{\epsilon}}_G(\dot{\boldsymbol{E}}, r, \varphi, \theta) = \dot{\boldsymbol{E}}' + \dot{E}_m \left(\frac{R}{r}\right)^3 \left[\mathbf{1} - 3\left(\mathbf{e}_r(\varphi,\theta) \otimes \mathbf{e}_r(\varphi,\theta)\right)\right] \tag{3.49}$$

where $\mathbf{e}_r(\varphi,\theta)$ r is the unitary vector on the radial direction.

The macroscopic plastic dissipation Π can be written as a function of the macroscopic strain rate $\dot{\boldsymbol{E}}$ as

$$\begin{aligned}\Pi(\dot{\boldsymbol{E}}) &= \frac{1}{V}\int_V \pi(\dot{\boldsymbol{\epsilon}}_G(\dot{\boldsymbol{E}}))dV = \frac{1}{V}\int_V \sigma_0\sqrt{\frac{2}{3}\dot{\boldsymbol{\epsilon}}_G : \dot{\boldsymbol{\epsilon}}_G} \\ &= \frac{\sigma_0}{V}\int_V \sqrt{\dot{E}_{eq}^2 - 4\dot{E}_m\left(\frac{R}{r}\right)^3 \dot{\boldsymbol{E}}' : (\mathbf{e}_r(\varphi,\theta)\otimes\mathbf{e}_r(\varphi,\theta)) + 4\dot{E}_m^2\left(\frac{R}{r}\right)^6} dV.\end{aligned} \tag{3.50}$$

where $V = \frac{4}{3}\pi R^3$ is RVE outer sphere volume and $dV = r^2\sin\theta d\theta d\varphi dr$ is the differential volume element written in spherical coordinates, with $r \in [r_v, R]$, $\varphi \in [0, 2\pi]$ and $\theta \in [0, \pi]$.

The viability of obtaining the analytical solution of Eq. (3.50) requires certain simplifications. Gurson (1975) assumed that the parcel $-4\dot{E}_m\left(\frac{R}{r}\right)^3 \dot{\boldsymbol{E}}' : (\mathbf{e}_r(\varphi,\theta)\otimes\mathbf{e}_r(\varphi,\theta))$ in Eq. (3.50) could be eliminated without gravely affecting the overall accuracy of the model. The argument was that this elimination was in fact linked to the linearization of the microscopic dissipation $\pi(\dot{\boldsymbol{\epsilon}}_G)$ in terms of the variable

$$\mu = \frac{\mathbf{e}_r^T.\dot{\boldsymbol{E}}.\mathbf{e}_r}{\dot{E}_{eq}}.$$

Thus, he concluded that the high-order terms in the series expansion of $\pi(\dot{\boldsymbol{\epsilon}}_G)$ could be neglected so that the resultant expression of Π in Eq. (3.50) could be simplified. This simplified expression reads

$$\begin{aligned}\Pi_G(\dot{\boldsymbol{E}}) &= \frac{\sigma_0}{V}\int_V \sqrt{\dot{E}_{eq}^2 + 4\dot{E}_m^2\left(\frac{R}{r}\right)^6} dV \\ &= \frac{\sigma_0\dot{E}_{eq}}{V}\int_V \sqrt{1 + 4H^2\left(\frac{R}{r}\right)^6} dV \\ &= \frac{\sigma_0\dot{E}_{eq}}{V}\int_{r_v}^R\int_0^{2\pi}\int_0^{\pi} \sqrt{1 + 4H^2\left(\frac{R}{r}\right)^6} r^2\sin\theta d\theta d\varphi dr.\end{aligned} \tag{3.51}$$

where $H = \dot{E}_m/\dot{E}_{eq}$ is the macroscopic strain rate triaxiality.

The macroscopic stresses $\boldsymbol{\Sigma}$ can now be obtained from $\Pi_G(\dot{u}_G)$ by solving the triple integral in Eq. (3.51):

$$\begin{aligned}\frac{\boldsymbol{\Sigma}^G}{\sigma_0} &= \frac{\partial\Pi_G}{\partial\dot{\boldsymbol{E}}} \\ &= \frac{2}{3}\ln\frac{2H + \sqrt{f^2 + 4H^2}}{f\left(2H + \sqrt{1 + 4H^2}\right)}\mathbf{1} + \frac{2}{3}\left(\sqrt{1 + 4H^2} - \sqrt{f^2 + 4H^2}\right)\mathbf{e}'(\eta) \\ &= \frac{\Sigma_m^G(H)}{\sigma_0}\mathbf{1} + \frac{\Sigma_{eq}^G(H)}{\sigma_0}\left(\frac{2}{3}\mathbf{e}'(\eta)\right)\end{aligned} \tag{3.52}$$

where $\Sigma_m^G = \frac{1}{3}\,\mathrm{Tr}\left(\boldsymbol{\Sigma}^G\right)$ and $\Sigma_{eq}^G = \sqrt{\frac{3}{2}\boldsymbol{\Sigma}'_G : \boldsymbol{\Sigma}'_G}$ and the porosity f is defined in Eq. (3.38).

The final yield criterion of the Gurson model was obtained by solving the system of equations

$$\Sigma_m^G(H) = \Sigma_m^G \tag{3.53a}$$
$$\Sigma_{eq}^G(H) = \Sigma_{eq}^G \tag{3.53b}$$

in terms of the strain rate triaxiality H in the resultant expressions of

$$\Sigma_m^G(H) = \frac{2}{3}\ln\frac{2H + \sqrt{f^2 + 4H^2}}{f\left(2H + \sqrt{1 + 4H^2}\right)} \tag{3.54}$$
$$\Sigma_{eq}^G(H) = \left(\sqrt{1 + 4H^2} - \sqrt{f^2 + 4H^2}\right) \tag{3.55}$$

to obtain

$$\left(\frac{\Sigma_{eq}^G}{\sigma_0}\right)^2 + 2f\cosh\left(\frac{3}{2}\frac{\Sigma_m^G}{\sigma_0}\right) - (1 + f^2) = 0. \tag{3.56}$$

Figure 11 illustrates the macroscopic yield surface obtained by the Gurson model for a material whose porosity is $f = 1\%$ and the yield stress is adopted unitary $\sigma_0 = 1$. It can be observed that the macroscopic behavior of the deviatoric planes shown in Fig. 11a are circumferential, which is a direct influence of the microscopic von Mises yield criterion. Moreover, the meridional planes depicted in Fig. 11b are independent on the macroscopic stress Lode angle Θ.

It is important to remark that, due to the linearization of $\pi(\dot{\boldsymbol{\epsilon}}_G)$ performed by Gurson (1975), the macroscopic stress Lode angle Θ is restricted to the Lode angle η associated to the macroscopic strain rate tensor. This coincidence is clearly a limitation that arises from that linearization. More recent works, as Benallal, Desmorat and Fournage (2014) and Benallal (2017), have overcome this limitation with semi-analytical developments and are described in section 3.4.

3.3 Phenomenological extensions

The Gurson model has been the topic of several studies since the 1980s aiming to surpass some of its limitations. A common approach for extending its capabilities is called phenomenological due to the nature of altering its original formulation. Basically, the predictions obtained with the original model are confronted with cell model FEM calculations and experimental data. Then, some heuristic modification based on these comparisons is

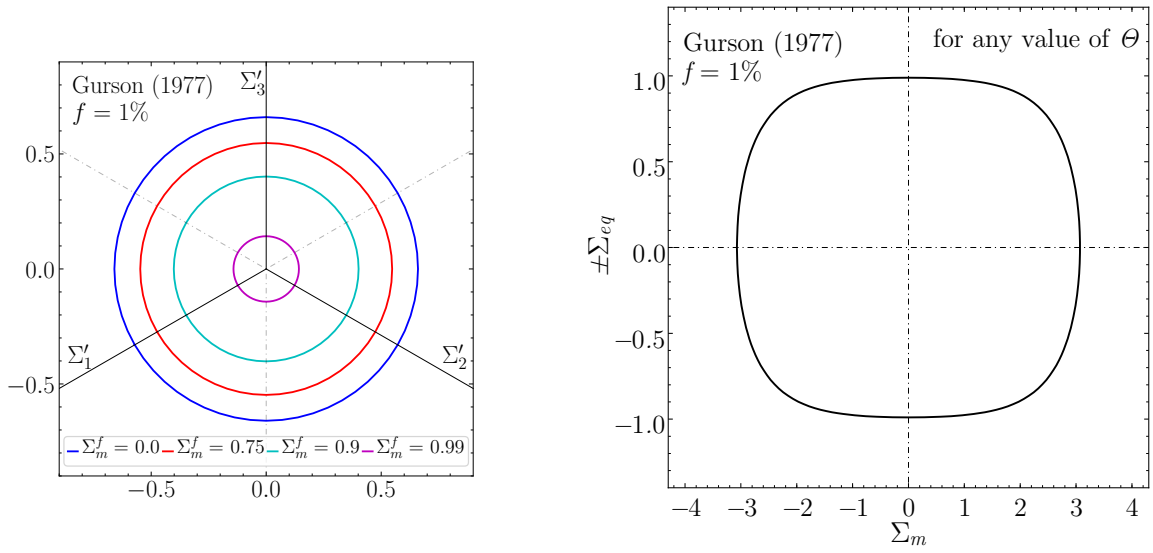

(a) Deviatoric planes (b) Meridional plane

Figure 11: Yield surface obtained with Gurson (1977) model for a porosity $f = 1\%$.

(a) deviatoric planes for different levels of $\Sigma^f_m = \Sigma_m/|\Sigma^{max}_m|$ and (b) meridional plane for any macroscopic stress Lode angle Θ. The microscopic yield stress is assumed to be unitary for simplicity, $\sigma_0 = 1$. Source: (FERREIRA; PROENÇA; BENALLAL, 2019)

proposed in order to better represent the reference behavior with a modification of the original model.

A classical Gurson model modification is that presented by Tvergaard (1981) and Tvergaard (1982). In these works, two parameters q_1 and q_2 were inserted into the original Gurson yield function (Eq. (3.56)) so that it better agreed with numerical computations of cylindrical and spherical periodic cells of porous materials. These works found that $q_1 = 1.5$ and $q_2 = 1.0$ calibrated the modified yield function (Eq. (3.57)) with enough accuracy.

$$\left(\frac{\Sigma^G_{eq}}{\sigma_0}\right)^2 + 2q_1 f \cosh\left(\frac{3q_2}{2}\frac{\Sigma^G_m}{\sigma_0}\right) - [1 + (q_1 f)^2)] = 0. \tag{3.57}$$

Another important extension of the Gurson model was proposed by Tvergaard and Needleman (1984). They argued that Gurson (1975) overestimated the porosity associated with the loss of the material stress capacity ($f_c = 1/q_1$). Thus, they proposed that the porosity should be defined as

$$f(f^*) = \begin{cases} f^*, & \text{for } f^* \leq f_c \\ f_c - \dfrac{f_u - f_c}{f_F - f_c}(f^* - f_c), & \text{for } f^* > fc, \end{cases} \tag{3.58}$$

where f_c is the critical porosity related to the beginning of the coalescence process, f_F is the final fracture porosity associated to the end of the coalescence process, and $f_u = 1/q_1$

is the porosity for which the material loses the capacity of supporting any stress. Based on the conclusions of the experimental investigations of Brown and Embury (1973 apud TVERGAARD; NEEDLEMAN, 1984) and Andersson (1977), Tvergaard and Needleman (1984) chose the values $f_c = 0.15$ and $f_F = 0.25$, respectively.

The effect of hardening in material matrices on the overall behavior of the Gurson-Tvergaard-Needleman (GTN) model was assessed by Koplik and Needleman (1988). They analyzed the spherical voids in periodic cells whose material matrix followed an exponential hardening law. According to their conclusions, $q_1 = 1.25$ and $q_2 = 1.0$ minimized the discrepancy of the GTN model with FEM calculations of periodic cells. Furthermore, a smaller value of $f_c = 0.03$ was required so that the accelerated void growth due to the matrix hardening was accounted for.

In a review on ductile material failure, Tvergaard (1990) resumed several studies on calibration of the parameters q_1 and q_2 by comparing the GTN model with both numerical and experimental references. He remarks that, in general, $q_1 \in [1.25, 2.0]$ and $q_2 \approx 1.0$ reasonably agree with those references.

Twenty years after the proposition of the GTN model, Bao and Wierzbicki (2004) pointed out the inconsistency between the prediction and experimental results of the strain failure for stress triaxialities less than $T < 1/3$ (see section 2.2 and Fig. 2). Based on this fact, a phenomenological extension of the Gurson model was developed by Nahshon and Hutchinson (2008). They proposed a modification on the evolution law of porosity so that the GTN model could better predict the strain failure caused by shear-dominated loadings. For this purpose, the new evolution law was altered to be dependent on the macroscopic stress Lode angle Θ:

$$\dot{f} = (1 - f)\,\mathrm{Tr}\,\dot{\boldsymbol{E}} + q_\Theta f \Theta(\boldsymbol{\Sigma}) \frac{\boldsymbol{\Sigma}' : \dot{\boldsymbol{E}}}{\Sigma_{eq}}, \tag{3.59}$$

where q_Θ is a scalar parameter to adjust the influence of the shear loading on the porosity evolution law, $\boldsymbol{\Sigma}'$ is the deviatoric part of the macroscopic stress tensor $\boldsymbol{\Sigma}$, and $\Theta(\boldsymbol{\Sigma})$ is the macroscopic stress Lode angle given by Eq. (3.27). The parameter q_Θ must be graphically inferred in Nahshon and Hutchinson (2008) as a function of the initial porosity f_0.

The prediction of strain failure by the Nahshon and Hutchinson (2008) for different values of q_Θ and increasing macroscopic stress triaxialities is depicted in Fig. 12. Their model could capture the overall tendency of decreasing ductility for decreasing stress triaxialities below $T = 1/3$ as in Bao and Wierzbicki (2004). However, there were no improvements in the *shape* of the macroscopic yield surfaces and further works have been developed since.

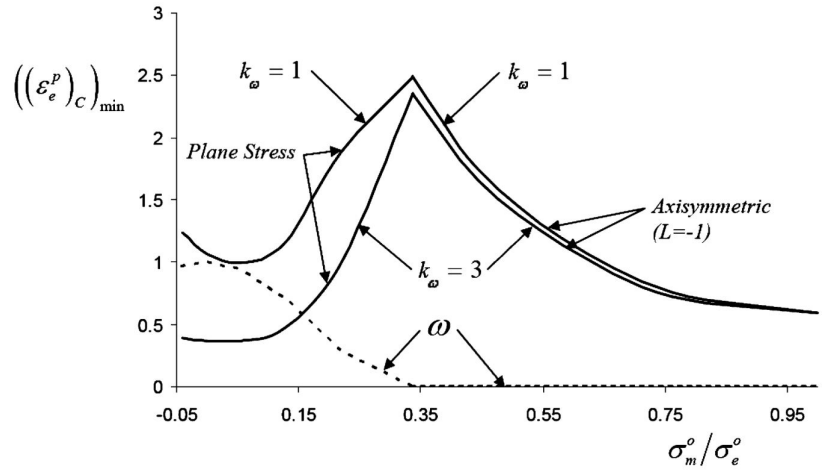

Figure 12: The relation between fracture strain and stress triaxiality obtained by Nahshon and Hutchinson (2008) aluminum alloy.

Relations between the macroscopic failure equivalent strain $((\epsilon_e^p)_c)_{min}$ and the macroscopic stress triaxiality σ_m^0/σ_e^0 for two adjustment parameter $k_\omega = 1$ and $k_\omega = 3$ was obtained with a modification on the porosity evolution law of the GTN model. The overall behavior as presented by Bao and Wierzbicki (2004) was captured. Note: $k_\omega = 1$, ω and σ_m^0/σ_e^0 corresponds to q_Θ, Θ and T in the notation of this document. Moreover, the parameter $L = -1$ is equivalent to $\Theta = 0$. Source: (NAHSHON; HUTCHINSON, 2008).

3.4 Analytical and numerical extensions

Basically, analytical and numerical extensions of the Gurson (1977) model relies on choosing some trial velocity field and on simplifications of the model in such a way that analytical developments become feasible. Among the more recent extensions, most have been concerned with the influence of the macroscopic Lode angle on the effective yield criterion of porous materials. For example, Cazacu et al. (2014) chose the trial velocity field proposed by Rice and Tracey (1969) to obtain macroscopic yield surfaces of those materials under axisymmetric loadings and concluded that these surfaces were dependent on the stress Lode angle. Trillat and Pastor (2005) also verified this dependence by performing non-linear optimizations based on both conic programming and the kinematic and static approaches of the Limit Analysis. Finally, Cheng et al. (2015) used the statical theorem of limit analysis to impose trial stress fields to 3D porous RVEs. They also obtained a yield criterion explictly dependent on the stress Lode angle.

Additionally, the effect of the *microscopic* stress Lode angle has also been a matter of recent developments. In short, the insertion of the effect of this angle accounts for non-quadratic yield criteria of material matrices (e.g. Tresca, Hershey-Hosford, William-Warnke). For instance, Trillat, Pastor and Thoré (2006) performed a non-linear optimization algorithm based on conic programming to obtain effective yield criterion of porous materials whose matrix followed Drucker-Prager criterion. Another example is the work of Soare (2016), who extended the Gurson model to account for the Hershey-Hosford matrix criterion.

They proceeded to approximate the expression of the microscopic plastic dissipation by a truncated Fourier series. This approximation allowed them to numerically obtain effective yield surfaces.

The next two subsections review some details of the two recent works by Benallal, Desmorat and Fournage (2014) and Benallal (2017), which are crucial to understanding the following chapters.

3.4.1 An assessment on the effect of linearizing the microscopic plastic potential in the Gurson model (BENALLAL; DESMORAT; FOURNAGE, 2014)

The effect of the linearization of the microscopic plastic dissipation $\pi(\dot{\boldsymbol{\epsilon}}_G)$ on the overall microscopic yield criterion obtained by the Gurson model was assessed by Benallal, Desmorat and Fournage (2014). They proceeded to the minimization of the macroscopic plastic dissipation $\Pi(\dot{\boldsymbol{E}})$ (Eq. (3.50)) without simplifying the expression of $\pi(\dot{\boldsymbol{\epsilon}}_G)$. For this purpose, they obtained the expression of the macroscopic stress $\boldsymbol{\Sigma} = \partial\Pi/\partial\dot{\boldsymbol{E}}$ by bearing the full expression of

$$\begin{aligned}\Pi(\dot{\boldsymbol{E}}) &= \frac{\sigma_0}{V}\int_V \sqrt{\dot{E}_{eq}^2 - 4\dot{E}_m\left(\frac{R}{r}\right)^3 \dot{\boldsymbol{E}}' : (\mathbf{e}_r(\varphi,\theta)\otimes\mathbf{e}_r(\varphi,\theta)) + 4\dot{E}_m^2\left(\frac{R}{r}\right)^6}\, dV \\ &= \frac{\sigma_0\dot{E}_{eq}}{V}\int_V \sqrt{1 - 4H\mu\left(\frac{R}{r}\right)^3 + 4H^2\left(\frac{R}{r}\right)^6}\, dV,\end{aligned} \tag{3.60}$$

where $\mu(\varphi,\theta) = \dot{\boldsymbol{E}}' : (\mathbf{e}_r(\varphi,\theta)\otimes\mathbf{e}_r(\varphi,\theta))$.

Since $\dot{\boldsymbol{E}}$ can be equivalently written in terms of its three invariants ($\dot{E}_m$ or H, $\dot{E}_{eq}$ and η or $\cos 3\eta$), the derivative $\boldsymbol{\Sigma} = \partial\Pi/\partial\dot{\boldsymbol{E}}$ is decomposed into three chain rule parcels

$$\begin{aligned}\boldsymbol{\Sigma} &= \frac{\partial\Pi}{\partial\dot{\boldsymbol{E}}} = \frac{\partial\Pi}{\partial\dot{E}_m}\frac{\partial\dot{E}_m}{\partial\dot{\boldsymbol{E}}} + \frac{\partial\Pi}{\partial\dot{E}_{eq}}\frac{\partial\dot{E}_{eq}}{\partial\dot{\boldsymbol{E}}} + \frac{\partial\Pi}{\partial\cos 3\eta}\frac{\partial\cos 3\eta}{\partial\dot{\boldsymbol{E}}} \\ &= \frac{1}{3}\frac{\partial\Pi}{\partial\dot{E}_m}\mathbf{1} + \frac{2}{3}\frac{\partial\Pi}{\partial\dot{E}_{eq}}\frac{\dot{\boldsymbol{E}}'}{\dot{E}_{eq}} - \frac{4}{3\sin\eta}\left(\frac{1}{\dot{E}_{eq}}\frac{\partial\Pi}{\partial\eta}\right)\left[\left(\frac{\dot{\boldsymbol{E}}'\cdot\dot{\boldsymbol{E}}'}{\dot{E}_{eq}^2} - \frac{1}{2}\mathbf{1}\right) - \frac{1}{2}\cos 3\eta\frac{\dot{\boldsymbol{E}}'}{\dot{E}_{eq}}\right]\end{aligned} \tag{3.61}$$

This assumption is consistent to isotropic materials due to the guarantee of coincidence of the principal directions of $\boldsymbol{\Sigma}$ and $\dot{\boldsymbol{E}}$. However, in anisotropic analyses, another approach should be applied (more details in chapter 4).

The complexity of Eq. (3.61) prevents that the resultant yield criterion to be written in a closed-form expression as in Gurson (1977). Nevertheless, Eq. (3.61) can be accurately solved by using common numerical integration procedures. Thus, Fig. 13 depicts three meridional planes of a macroscopic yield surface related to a material whose porosity and yield stress are respectively assumed $f = 1\%$ and $\sigma_0 = 1$. These meridional planes

correspond to six different levels of the macroscopic stress Lode angle: $\Theta = 0$, $\Theta = \pi/6$ and $\Theta = \pi/3$ for the upper quadrants ($\Sigma_{eq} \geq 0$); and $\Theta = \pi$, $\Theta = \pi/6 + \pi$ and $\Theta = \pi/3 + \pi$ for the lower quadrants (i.e. $\Sigma_{eq} < 0$). As Gurson (1975) had remarked, the linearization of $\pi(\dot{\boldsymbol{\epsilon}}_G)$ does not strongly affect the overall model's behavior. However, further improvements on the Gurson model relies on the possibility of accounting for the influence of the stress Lode angle on shear-dominated loads, which can only be considered, in the context of the Gurson model, by using the non-linearized plastic dissipation potential, as in Benallal, Desmorat and Fournage (2014).

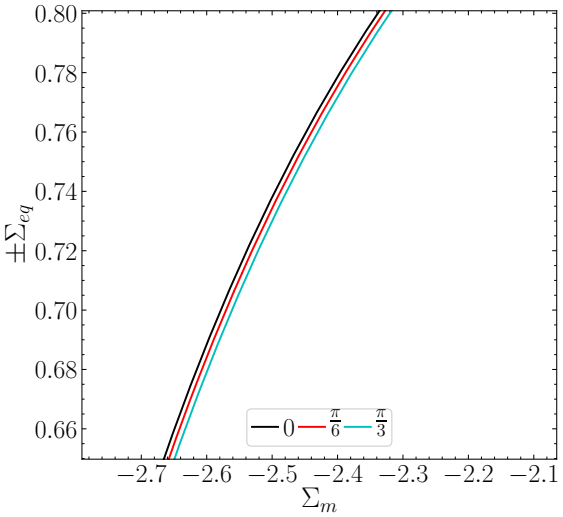

(a) Zoom on the upper left quadrant

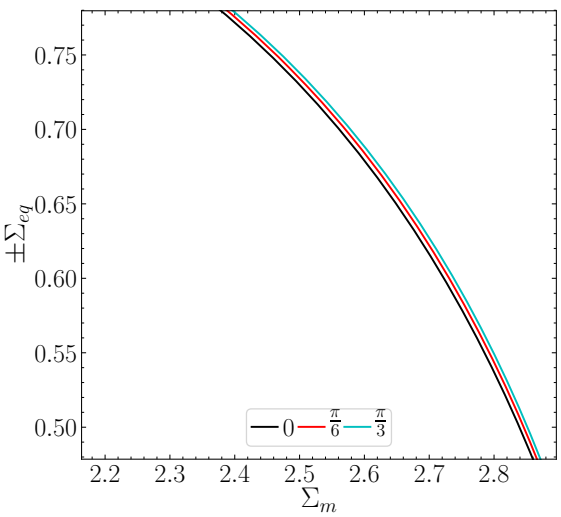

(b) Zoom on the upper right quadrant

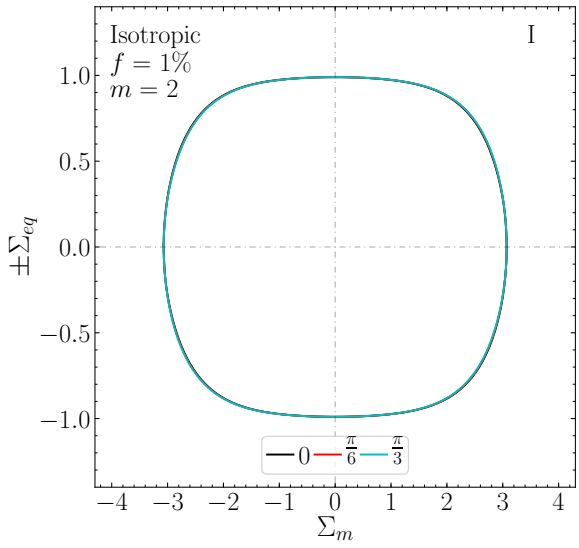

(c) Meridional planes

Figure 13: Meridional planes of a yield surface for porosity $f = 1\%$ obtained with the Benallal, Desmorat and Fournage (2014) model.

A slight distinctness between meridional planes associated to different macroscopic stress Lode angles Θ can be noticed. The microscopic yield stress σ_0 is assumed to be unitary for the sake of simplicity. Source: (FERREIRA; PROENÇA; BENALLAL, 2019).

3.4.2 Including the influence of the microscopic stress Lode angle on the Gurson model (BENALLAL, 2017)

Subsequently to Benallal, Desmorat and Fournage (2014), Benallal (2017) included the influence of the *microscopic* stress Lode angle ω on the Gurson model. This parameter was inserted into the microscopic yield criterion $\psi(\boldsymbol{\sigma})$ by defining an auxiliary function $g(\omega)$ that multiplies the equivalent measure of stress σ_{eq}:

$$\psi(\boldsymbol{\sigma}) = \sigma_{eq} g(\omega) - \sigma_0 \leq 0 \tag{3.62}$$

where, in order to guarantee the convexity of the yield surface given by $\psi(\boldsymbol{\sigma})$, the function $g(\omega)$ must satisfy $g''(\omega) + g(\omega) \geq 0$.

In a practical view, the function $g(\omega)$ generalizes the *shape* of the microscopic yield surface. Thus, a desired behavior of the yield criterion may be obtained by defining a specific function $g(\omega)$. Accordingly, Benallal (2017) proposed a particularization of $g(\omega)$ so that it represents the Hershey-Hosford yield criterion ((HERSHEY, 1954 apud NEMAT-NASSER; HORI, 1993) and (HOSFORD, 1972))

$$\sigma_{HH} = \left\{ \frac{1}{2} \left[(\sigma_1 - \sigma_2)^m + (\sigma_2 - \sigma_3)^m + (\sigma_3 - \sigma_1)^m \right] \right\}^{1/m}. \tag{3.63}$$

The particularized expression of $g(\omega)$ to represent this criterion is shown in Eq. (3.64). The von Mises yield criterion is retrieved if $m = 2$; the Tresca's, if $m \to \infty$.

$$\begin{aligned} g(\omega) = \frac{2}{3} \Bigg\{ \frac{1}{2} \Big[& (\cos\omega_1 - \cos\omega_2)^m + \\ & (\cos\omega_2 - \cos\omega_3)^m + \\ & (\cos\omega_3 - \cos\omega_1)^m \Big] \Bigg\}^{1/m}, \end{aligned} \tag{3.64}$$

where $\omega_1 = \omega$, $\omega_2 = \omega - 2\pi/3$ and $\omega_3 = \omega + 2\pi/3$.

In a similar way to Gurson (1975), the microscopic plastic potential was obtained. For this purpose, one must recall the relations for the microscopic yield criterion in Eq. (3.62) and the normality rule for the plastic flow in Eq. (3.36). The microscopic plastic dissipation potential $\pi(\dot{\boldsymbol{\epsilon}})$ is then analogous to that in Eq. (3.42). The main difference from Benallal's approach to Gurson's is the expression of the plastic multiplier rate $\dot{\lambda}$, since the microscopic yield criterion $\psi(\boldsymbol{\sigma})$ is also dependent on the shape function $g(\omega)$:

$$\dot{\lambda} = \frac{\dot{\epsilon}_{eq}}{\sqrt{\frac{2}{3} \frac{\partial \psi}{\partial \boldsymbol{\sigma}} : \frac{\partial \psi}{\partial \boldsymbol{\sigma}}}} = \frac{\dot{\epsilon}_{eq}}{\sqrt{[g(\omega)]^2 + [g'(\omega)]^2}}. \tag{3.65}$$

where

$$\frac{\partial \psi}{\partial \boldsymbol{\sigma}} = \frac{\partial \sigma_{eq}}{\partial \boldsymbol{\sigma}} g(\omega) + \sigma_{eq} \frac{\partial g}{\partial \boldsymbol{\sigma}}. \tag{3.66}$$

In order to eliminate the dependence of $\dot{\lambda}$ in Eq. (3.65) on the microscopic stress Lode angle ω, a relation between ω and ξ had to be derived. Then, Benallal (2017) proceeded following the definition of the microscopic strain rate Lode angle ξ in Eq. (3.20). In short,

$$\begin{aligned} \xi &= \frac{1}{3} \arccos\left(\frac{4 \det \dot{\boldsymbol{\epsilon}}'}{(\dot{\epsilon}_{eq})^3}\right) = \frac{1}{3} \arccos\left(\frac{4 \det \dfrac{\partial \psi}{\partial \boldsymbol{\sigma}}}{\left(\dfrac{2}{3} \dfrac{\partial \psi}{\partial \boldsymbol{\sigma}} : \dfrac{\partial \psi}{\partial \boldsymbol{\sigma}}\right)^{3/2}}\right) \\ &= \omega + \arctan\left(\frac{g'(\omega)}{g(\omega)}\right). \end{aligned} \tag{3.67}$$

The necessity of writing the microscopic plastic dissipation π in Eq. (3.42) only in terms of the $\dot{\boldsymbol{\epsilon}}'$ or its invariants requires ω to be obtained by a given ξ. This means that the relation $\xi = \xi(\omega)$ in Eq. (3.67) must be inverted. Although it is not possible to be analytically achieved, a one-dimensional interpolation procedure can accurately obtain

$$\omega \approx \omega(\xi) \tag{3.68}$$

The approximation in Eq. (3.68) leads to rewriting the plastic multiplier rate in $\dot{\lambda}$ in Eq. (3.65) only in terms of the admissible microscopic strain rate $\dot{\boldsymbol{\epsilon}}'$ as

$$\dot{\lambda} = \frac{\dot{\epsilon}_{eq}}{\sqrt{[g(\omega)]^2 + [g'(\omega)]^2}} \approx \frac{\dot{\epsilon}_{eq}}{\sqrt{[g(\omega(\xi))]^2 + [g'(\omega(\xi))]^2}}. \tag{3.69}$$

The microscopic plastic dissipation potential $\pi(\dot{\boldsymbol{\epsilon}}')$ can be finally defined as

$$\pi(\dot{\boldsymbol{\epsilon}}') = \sigma_0 \dot{\epsilon}_{eq} G(\dot{\boldsymbol{\epsilon}}'), \tag{3.70}$$

where the auxiliary function $G(\dot{\boldsymbol{\epsilon}}')$ satisfies

$$G(\dot{\boldsymbol{\epsilon}}') = \frac{1}{\sqrt{[g(\omega(\xi))]^2 + [g'(\omega(\xi))]^2}}. \tag{3.71}$$

Analogously to Benallal, Desmorat and Fournage (2014), the macroscopic stress $\boldsymbol{\Sigma}$ is obtained by assuming the Gurson's trial field $\dot{\boldsymbol{\epsilon}}_G$ (Eq. (3.49)) as the admissible microscopic strain rate $\dot{\boldsymbol{\epsilon}}' := \dot{\boldsymbol{\epsilon}}_G$. Additionally, the derivative $\boldsymbol{\Sigma} = \partial \Pi / \partial \dot{\boldsymbol{E}}$ is still evaluated

by considering $\dot{\boldsymbol{E}}$ dependent only on its three invariants $\dot{E}_m$ or H, $\dot{E}_{eq}$ and η as in Eq. (3.61).

The strong effect of the third microscopic stress invariant ω is illustrated in Fig. 14. Therein, two groups of macroscopic deviatoric planes are highlighted. The first one (Fig. 14a) is associated to a shape parameter $m = 8$ and may be regarded as an intermediate state between the von Mises and Tresca criteria. The second group (Fig. 14b) was obtained for $m = 20$, which already presents a behavior closer to that idealized by Tresca. Both groups consist of macroscopic deviatoric planes for different levels of $\Sigma_m^f = \Sigma_m/|\Sigma_m^{max}|$.

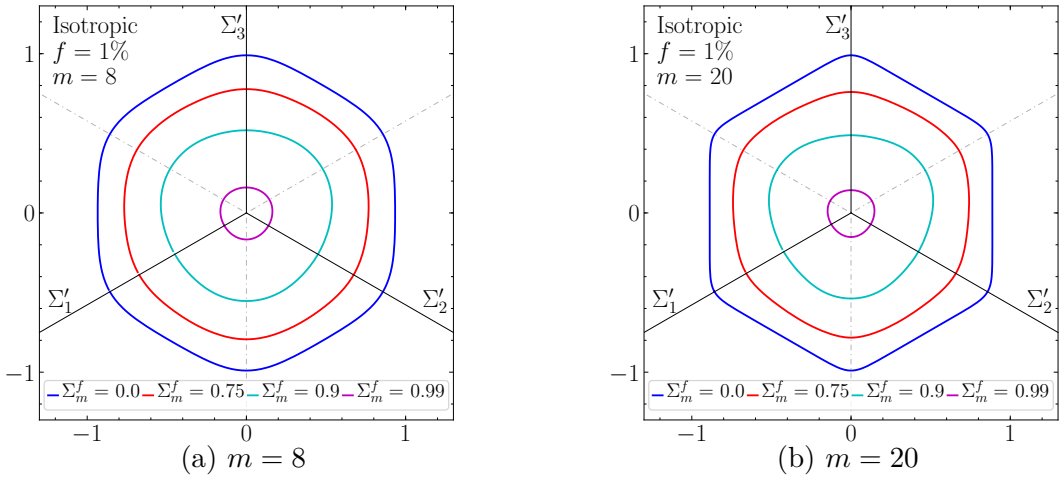

(a) $m = 8$ (b) $m = 20$

Figure 14: Macroscopic deviatoric planes obtained with the model proposed by Benallal (2017) for two intermediate shape parameters of the Hershey-Hosford criterion.

Macroscopic deviatoric planes for different levels of $\Sigma_m^f = \Sigma_m/|\Sigma_m^{max}|$ obtained from the Benallal (2017) model. The shape parameter (a) $m = 8$ implies an intermediate s between the von Mises and Tresca criteria; and (b) $m = 20$, Tresca-like sharper edges for $\Sigma_m^f = 0$. Source: (FERREIRA; PROENÇA; BENALLAL, 2019)

Meridional planes correspondent to the macroscopic yield surface in Fig. 14 are shown in Fig. 15, for $m = 8$, and in Fig. 16, for $m = 20$. In both figures, six levels of macroscopic stress Lode angle are illustrated: $\Theta = 0$, $\Theta = \pi/6$ and $\Theta = \pi/3$, for the upper quadrants (i.e. $\Sigma_{eq} \geq 0$); and $\Theta = 0 + \pi$, $\Theta = \pi/6 + \pi$ and $\Theta = \pi/3 + \pi$, for the lower quadrants (i.e. $\Sigma_{eq} < 0$). It can be observed that the microscopic stress Lode angle ω considerably affects the macroscopic meridional planes. There is a remarkable consequence in the clearer distinction between different macroscopic stress Lode angles Θ levels in comparison to those results obtained by Benallal, Desmorat and Fournage (2014) for the microscopic von Mises criterion (Fig. 13).

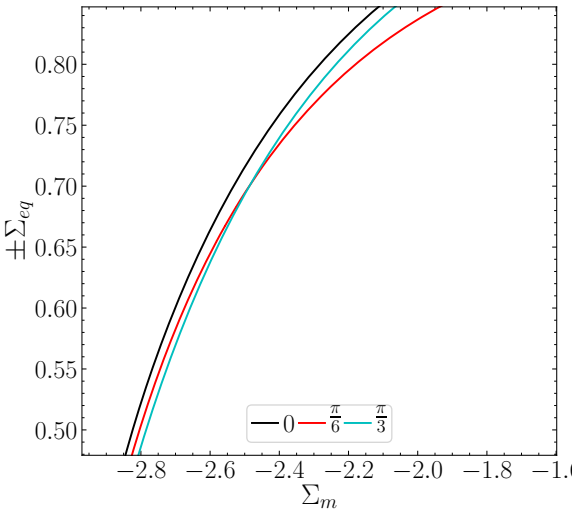

(a) Zoom on the left side

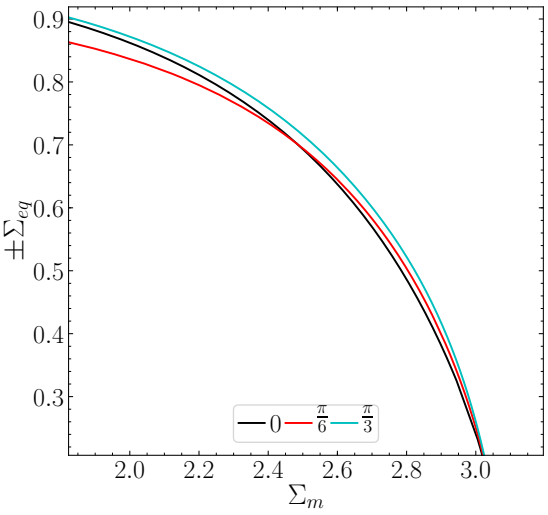

(b) Zoom on the right side

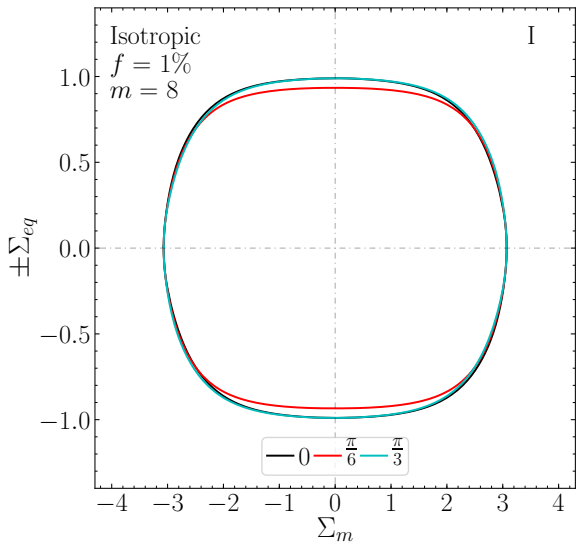

(c) Meridional planes

Figure 15: Macroscopic meridional planes for different stress Lode angles Θ obtained from the Benallal (2017) model.

The shape parameter and the porosity are respectively assumed $m = 8$ and $f = 1\%$. The microscopic yield stress is taken as unitary for the sake of simplicity, $\sigma_0 = 1$. Source: (FERREIRA; PROENÇA; BENALLAL, 2019).

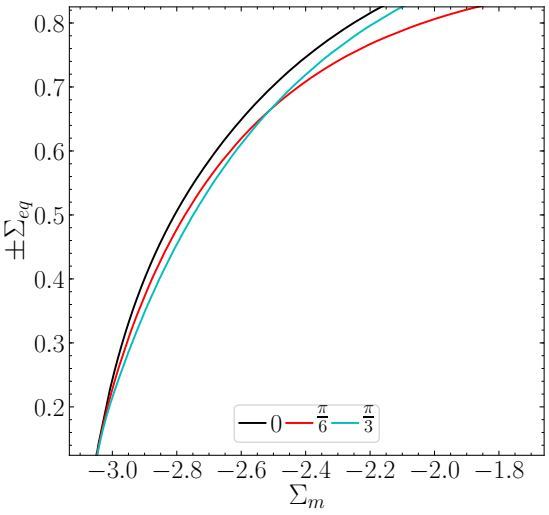

(a) Zoom on the left side

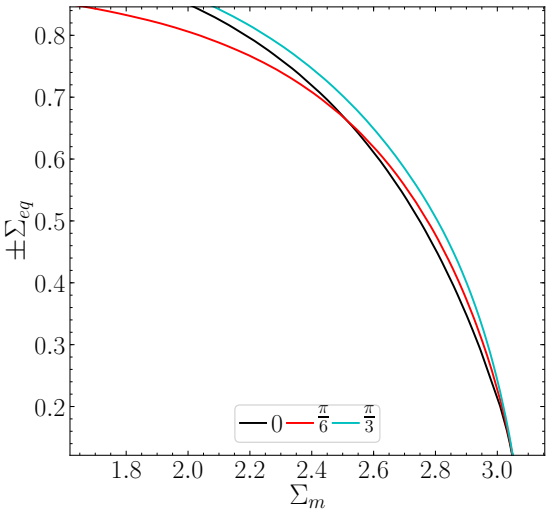

(b) Zoom on the right side

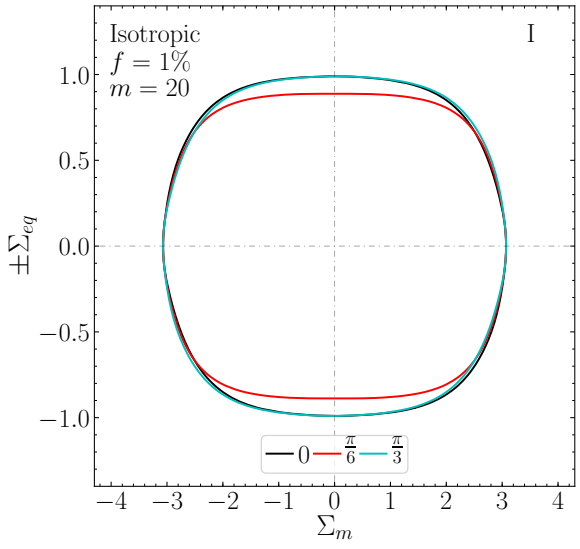

(c) Meridional planes

Figure 16: Macroscopic meridional planes for different stress Lode angles Θ obtained from the Benallal (2017) model.

The shape parameter and the porosity are respectively assumed $m = 20$ and $f = 1\%$. The microscopic yield stress is taken as unitary for the sake of simplicity, $\sigma_0 = 1$. Source: (FERREIRA; PROENÇA; BENALLAL, 2019).

4 EFFECT OF POROUS MORPHOLOGY ON DUCTILE FAILURE

4.1 Introduction

Despite the success of the Gurson model, ever since then many studies have addressed surpassing some of its limitations. One of them is the restriction about void morphology, mainly in the isotropic case of a spherical RVE. In this case, the spherical void is assumed to conserve its morphology throughout the entire deformation process. In other words, the damage evolution is described only in terms of porosity, which means that an eventual shape change is not accounted for.

Important contributions to this field have been accomplished by Gologanu, Leblond and Devaux (1993), Gologanu, Leblond and Devaux (1994) and Gologanu et al. (1997). They approached the case of spheroidal cavities contained in a confocal spheroidal matrix and derived its macroscopic yield criterion by assuming special velocity fields which satisfy homogeneous boundary conditions on the outer surface. These fields were idealized by making an interesting analogy between the velocity in a point with the electric field on the same point lead by an electric charge located in the RVE center. After an extensive mathematical development detailed in their works and important approximations of integral terms by their respective averages in the RVE domain, they proposed a Gurson-like yield criterion expression dependent on both porosity and a shape factor so that the spheroidal void could be defined. Because of its rigorous mathematical aspects, this model is limited to spheroidal voids (both elongated and flatted ones) aligned to the principal directions of axisymmetric macroscopic strain rate field. Gologanu et al. (2001) and Gologanu, Leblond and Devaux (2001) also proposed models for predicting coalescence of initially spherical voids inside cylindrical RVEs under axisymmetric deformation. These voids then might evolve and assume an spheroidal shape.

Another group of significant advances to the consideration of void morphology on ductile rupture of porous materials were developed by Ponte Castañeda and Zaidman (1994), Ponte Castañeda and Zaidman (1996), Zaidman and Ponte Castañeda (1996), Kailasam, Aravas and Ponte Castañeda (2000), Aravas and Ponte Castañeda (2004), Danas and Ponte Castañeda (2009a) and Danas and Ponte Castañeda (2009b). Basically, these works rely on the estimation of effective properties of nonlinear composite materials (which in these cases are porous ones) proposed by Ponte Castañeda (1991) and Ponte Castañeda (1992), which uses an approach based on variational principles to obtain these properties by a specific comparison with a correlated linear composite, and also Ponte Castañeda (2002a) and Ponte Castañeda (2002b), which is based on a second-order variational formulation. The choice of the strain rate field relies on the Eshelby (1957) approach to a problem of an

inclusion contained in an infinite elastic medium. In order to simulate in an elastic medium the incompressibility condition of ductile plasticity, they impose the Poisson parameter to hold $\nu = 1/2$. Although these models comprehend arbitrarily oriented ellipsoidal voids and consider finite strain formulation, the fact that Elsheby's microscopic strain rate field is derived to an infinite elastic media might limit their representativity of plastic materials.

Another important improvement on the Gurson model to account for the growth and coalescence of spheroidal cavities is provided by Pardoen and Hutchinson (2000). Basically, they heuristically extended the approaches of Gologanu et al. (1997) for considering void shapes and Thomason (1993) for taking the onset of coalescence into account. The important feature of their model is that no phenomenological variables – which are difficult to determine experimentally – are therein considered. In addition, only one heuristic parameter q is required, which does not need to be obtained at each analysis, but can be obtained once and for all by FEM cell calculations. They also compared their heuristic criterion with several 3D FEM calculations and confirmed the good agreement between these models.

Monchiet et al. (2006) and Monchiet et al. (2008) extended the models of Gologanu, Leblond and Devaux (1993) and Gologanu, Leblond and Devaux (1994), by following similar approximations and assumptions as those works, in order to the material matrix to follow the anisotropic yield criterion proposed by Hill (1948). Next, Monchiet, Charkaluk and Kondo (2007) and Monchiet, Charkaluk and Kondo (2011) took the Eshelby (1957) displacement field for the problem of an inclusion surrounded by an infinite continuum medium as a trial velocity field to the problem of a hollow spheroidal RVE with perfectly rigid-plastic material matrix. Since this field is not the exact one to the referred RVE problem, this approach also constitutes an upper bound. This model was implemented into a FEM code by Lin et al. (2010) so that notched and round tensile bars could be modeled in detail. Their results showed the improvement provided by this new trial velocity field.

The class of velocity fields as that used in Gologanu, Leblond and Devaux (1993) and Gologanu, Leblond and Devaux (1994) was generalized by Leblond and Gologanu (2008). They found a class of velocity field, related to the problem of a spheroidal RVE with a confocal spheroidal void, which respects the assumption of uniform (i.e. constant) strain rate conditions along every confocal spheroid in the RVE domain. Madou and Leblond (2012a) and Madou and Leblond (2012b) used this velocity field to obtain effective yield criterion of ductile materials with spheroidal voids by asymptotically expanding the expressions of the macroscopic plastic dissipation potential and of the effective stress tensors.

Flandi and Leblond (2005a) and Flandi and Leblond (2005b) proposed a heuristic expression of the macroscopic gauge function (which is an analogous concept defined by Leblond, Perrin and Suquet (1994) of yield functions, albeit used in a viscoplastic materials

context) of porous materials containing spheroidal voids. This expression was imposed to reproduce reference models when particularized to certain cases, as for the perfectly rigid-plastic case of Gologanu, Leblond and Devaux (1993) and Gologanu, Leblond and Devaux (1994). The restriction to spheroidal voids and the heuristic character of the gauge function expression are the drawbacks of this approach, in spite of reasonable agreement numerical unit cell FEM calculations.

In order to provide a contribution to the study of ductile plasticity, this chapter presents a Gurson-based approach to obtain an overall yield criterion of anisotropic porous materials. A spherical RVE containing a centered ellipsoidal void is assumed to represent orthotropic porous media under a rupture process. The material matrix surrounding the void is dependent on the third invariant of microscopic stresses, as in Benallal (2017). The Gurson's trial velocity field is chosen to approximate the solution of that RVE by an upper bound. Although only the void morphology is altered in relation to Benallal's work, the analytical approach as well as some fundamental definitions have to be generalized so that the anisotropic effect induced is the void morphology be adequately considered. The results hereby presented show the consistency of the present formulation and provide important insights for further investigation.

4.2 A Gurson-like RVE with arbitrary centered void morphology

Aiming to propose an advance on the work by Benallal (2017), let us initially consider a spherical RVE whose material matrix and boundary conditions follow the configuration introduced in his work. However, let the centered cavity assume now an ellipsoidal morphology instead of a spherical one. Figure 17 schematizes an arbitrary spherical RVE with an isotropic material matrix defined in Ω and uniform macroscopic strain rate $\dot{\boldsymbol{E}}$ applied to the external contour $\partial\Omega^+$. The inner contour $\partial\Omega^-$, i.e. the void surface, is assumed to be traction-free. A mathematical description of the sets Ω, $\partial\Omega^+$, $\partial\Omega^-$ and $\overline{\Omega}$ is presented in Eq. (4.1).

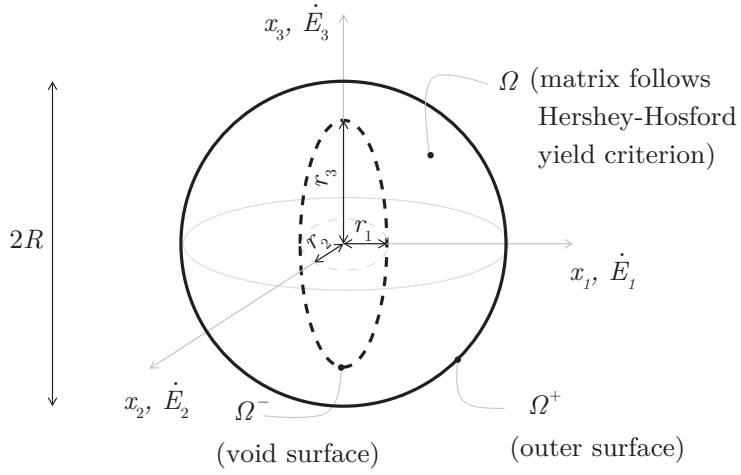

Figure 17: A spherical RVE with an ellipsoidal void inside it.

The ellipsoidal void is centered in the RVE and has principal radii denoted by r_1, r_2 and r_3. The orientation frame of the void morphology coincides with the principal directions of an arbitrary macroscopic strain rate $\dot{\boldsymbol{E}}$. The material matrix in Ω is assumed to follow the Hershey-Hosford microscopic yield criterion (see Eq. (3.63)). Source: the author.

$$
\begin{aligned}
\Omega &= \left\{(x_1,x_2,x_3) | x_1^2+x_2^2+x_3^2 < R \quad \text{and} \quad \left(\frac{x_1}{r_1}\right)^2+\left(\frac{x_2}{r_2}\right)^2+\left(\frac{x_3}{r_3}\right)^2 > 1\right\} \\
\partial\Omega^+ &= \left\{(x_1,x_2,x_3) | x_1^2+x_2^2+x_3^2 = R\right\} \\
\partial\Omega^- &= \left\{(x_1,x_2,x_3) | \left(\frac{x_1}{r_1}\right)^2+\left(\frac{x_2}{r_2}\right)^2+\left(\frac{x_3}{r_3}\right)^2 = 1\right\} \\
\overline{\Omega} &= \left\{(x_1,x_2,x_3) | x_1^2+x_2^2+x_3^2 < R\right\}
\end{aligned}
\tag{4.1}
$$

where $r_i < R$, $i = 1,2,3$.

A crucial aspect of the RVE conceived above is that the principal directions of the applied macroscopic strain rate $\dot{\boldsymbol{E}}$ coincide with those of the ellipsoidal porous. This configuration is in accordance with the results that will be shown in section 4.4. However, as justified in chapter 7, this restriction is only necessary for visualizing the yield surfaces in the principal macroscopic stress space and it is not a limitation of the formulation itself.

An RVE with an ellipsoidal cavity, as illustrated in Fig. 17, can be conveniently described in terms of relative lengths (ℓ_1,ℓ_2,ℓ_3), the porosity f and the external radius R of the RVE. The advantage of using relative lengths (ℓ_1,ℓ_2,ℓ_3) is that they might represent only the ratios between the principal radii of the ellipsoid. Thus, this notation briefly describes how much elongated or flatted an ellipsoid is in each direction (x_1,x_2,x_3). The principal radii (r_1,r_2,r_3) of the ellipsoid are obtained in terms of (ℓ_1,ℓ_2,ℓ_3), f and R as

$$
r_i = \ell_i \sqrt[3]{\frac{f}{\ell_1\ell_2\ell_3}} R \quad i = 1,2,3. \tag{4.2}
$$

For example, an RVE with $(\ell_1, \ell_2, \ell_3) = (1, 4, 8)$, $f = 1\%$ and $R = 1$ (unitary) presents an ellipsoidal cavity whose principal radii give $r_1 \approx 0.067860$, $r_2 \approx 0.271442$ and $r_3 \approx 0.542884$, which satisfies $r_2/r_1 = \ell_2/\ell_1 = 4$ and $r_3/r_1 = \ell_3/\ell_1 = 8$.

The classical definitions of spheroids (i.e. an ellipsoid whose two of the principal radii have the same length) are also useful for describing the void morphology. A spheroid is said to be *prolate* (*oblate*) if one principal radius is greater (less) than the other two. For instance, in terms of relative lengths (ℓ_1, ℓ_2, ℓ_3), a $(8, 1, 1)$ is prolate spheroid and a $(1, 8, 8)$ is an oblate one.

Finally, each of the principal radii of the ellipsoidal void must be less than the external radius R so that the cavity is thoroughly contained in the RVE. This condition in terms of the relative lengths (ℓ_1, ℓ_2, ℓ_3) satisfies

$$l_i \sqrt[3]{\frac{f}{\ell_1 \ell_2 \ell_3}} < 1 \quad i = 1, 2, 3. \tag{4.3}$$

4.3 Deriving the macroscopic yield surface

Since the material matrix defined in the domain Ω of the RVE follows the Hershey-Hosford criterion (Eq. (3.63)) in the same way as that developed in Benallal (2017), the microscopic plastic dissipation potential $\pi(\dot{\boldsymbol{E}})$ holds

$$\pi(\dot{\boldsymbol{\epsilon}}) = \tilde{\pi}(\dot{\epsilon}_{eq}(\dot{\boldsymbol{\epsilon}}))G(\xi(\dot{\boldsymbol{\epsilon}})) = \frac{\sigma_0 \dot{\epsilon}_{eq}}{\sqrt{[g(w(\xi))]^2 + [g'(w(\xi))]^2}} \tag{4.4}$$

where

$$\tilde{\pi}(\dot{\epsilon}_{eq}) = \sigma_0 \dot{\epsilon}_{eq}, \tag{4.5}$$

$$G(\xi(\dot{\boldsymbol{\epsilon}})) = \frac{1}{\sqrt{[g(w(\xi))]^2 + [g'(w(\xi))]^2}}, \tag{4.6}$$

$$\dot{\epsilon}_{eq} = \sqrt{\frac{2}{3}\dot{\boldsymbol{\epsilon}} : \dot{\boldsymbol{\epsilon}}}, \tag{4.7}$$

$$\xi = \frac{1}{3} \arccos\left[\frac{4 \det \dot{\boldsymbol{\epsilon}}}{(\dot{\epsilon}_{eq})^3}\right], \tag{4.8}$$

$$\begin{aligned} g(\omega) = \frac{2}{3}\Bigg\{ \frac{1}{2}\Big[&(\cos\omega_1 - \cos\omega_2)^m + \\ &(\cos\omega_2 - \cos\omega_3)^m + \\ &(\cos\omega_3 - \cos\omega_1)^m \Big] \Bigg\}^{1/m} \end{aligned} \tag{4.9}$$

and $\omega \approx \omega(\xi)$ is obtained by a one-dimensional linear interpolation procedure.

A detailed development of Eq. (4.4) is given in chapter 3 in the present document, as well as in the original work of Benallal (2017).

The macroscopic dissipation potential is then defined as

$$\Pi(\dot{\boldsymbol{E}}) = \frac{1}{V}\int_{\overline{\Omega}} \pi[\dot{\boldsymbol{\epsilon}}(\dot{\boldsymbol{E}})]dV \tag{4.10}$$

and the macroscopic stress tensor $\boldsymbol{\Sigma}$ gives

$$\boldsymbol{\Sigma} = \frac{\partial \Pi}{\partial \dot{\boldsymbol{E}}} = \frac{1}{V}\int_{\overline{\Omega}} \frac{\partial \pi}{\partial \dot{\boldsymbol{E}}} dV, \tag{4.11}$$

where V refers to the volume occupied by the sphere $\overline{\Omega} = \{(x_1, x_2, x_3)/x_1^2 + x_2^2 + x_3^2 < b\}$.

Differently to Benallal (2017), the derivative $\partial\pi/\partial\dot{\boldsymbol{E}}$ hereby cannot be developed only in terms of its invariants $\dot{E}_m$, $\dot{E}_{eq}$ and η. Since some anisotropic effect is expected to be acquired from the potential $\Pi(\dot{\boldsymbol{E}})$ due to the void morphology, the principal directions of $\dot{\boldsymbol{E}}$ also play a role in Eq. (4.11), as illustrated in Fig. 18 and 19. Thus, it is useful to treat the macroscopic strain rate tensor $\dot{\boldsymbol{E}}$ intrinsically (i.e. as a whole tensor) in the development of Eq. (4.11), and not separately in terms of its invariants. The derivative $\partial\pi/\partial\dot{\boldsymbol{E}}$ is then developed as

$$\begin{aligned}\frac{\partial \pi}{\partial \dot{\boldsymbol{E}}} &= \frac{\partial \tilde{\pi}}{\partial \dot{\boldsymbol{E}}} G(\xi) + \tilde{\pi}(\dot{\epsilon}_{eq}) \frac{\partial G}{\partial \dot{\boldsymbol{E}}} \\ &= \frac{\partial \tilde{\pi}}{\partial \dot{\epsilon}_{eq}} \left(\frac{\partial \dot{\epsilon}_{eq}}{\partial \dot{\boldsymbol{\epsilon}}} : \frac{\partial \dot{\boldsymbol{\epsilon}}}{\partial \dot{\boldsymbol{E}}} \right) G(\xi) + \tilde{\pi}(\dot{\epsilon}_{eq}) \frac{\partial G}{\partial \omega} \frac{\partial \omega}{\partial \xi} \left(\frac{\partial \xi}{\partial \dot{\boldsymbol{\epsilon}}} : \frac{\partial \dot{\boldsymbol{\epsilon}}}{\partial \dot{\boldsymbol{E}}} \right)\end{aligned} \tag{4.12}$$

where

$$\frac{\partial \dot{\epsilon}_{eq}}{\partial \dot{\boldsymbol{\epsilon}}} = \frac{2}{3} \frac{\partial \dot{\boldsymbol{\epsilon}}}{\partial \dot{\epsilon}_{eq}}, \tag{4.13}$$

$$\frac{\partial \tilde{\pi}}{\partial \dot{\epsilon}_{eq}} = \sigma_0, \tag{4.14}$$

$$\frac{\partial \omega}{\partial \xi} = \frac{[g(\xi)]^2 + [g'(\xi)]^2}{[g(\xi)]^2 + g(\xi)g''(\xi)}, \tag{4.15}$$

and

$$\frac{\partial \xi}{\partial \dot{\boldsymbol{\epsilon}}} = -\frac{4}{3} \frac{1}{\dot{\epsilon}_{eq} \sin 3\xi} \left[\left(\frac{\dot{\boldsymbol{\epsilon}}}{\dot{\epsilon}_{eq}} \right)^2 - \frac{1}{2}\mathbf{1} - \frac{1}{2}\cos 3\xi \left(\frac{\dot{\boldsymbol{\epsilon}}}{\dot{\epsilon}_{eq}} \right) \right]. \tag{4.16}$$

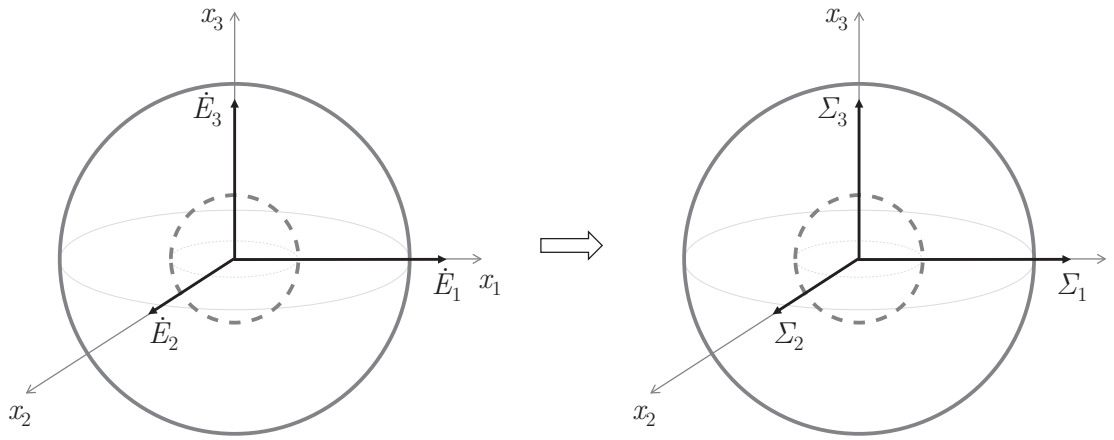

(a) principal directions of $\dot{\boldsymbol{E}}$ coincident with the referential $(\boldsymbol{e}_1, \boldsymbol{e}_2, \boldsymbol{e}_3)$

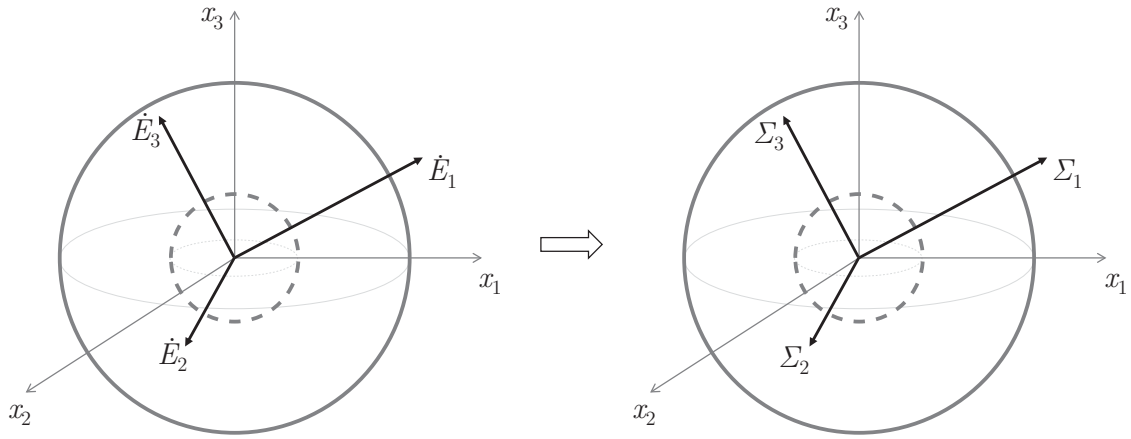

(b) principal directions of $\dot{\boldsymbol{E}}$ not coincident with the referential $(\boldsymbol{e}_1, \boldsymbol{e}_2, \boldsymbol{e}_3)$

Figure 18: Illustration of the influence of the principal directions of the macroscopic strain rate $\dot{\boldsymbol{E}}$ on the macroscopic stress $\boldsymbol{\Sigma}$ for hollow spherical RVEs.

Regardless of the principal directions of the macroscopic strain rate $\dot{\boldsymbol{E}}$, the resultant macroscopic stress $\boldsymbol{\Sigma}$ holds these same directions (i.e. $\Sigma_i/|\Sigma_i| \equiv \dot{E}_i/|\dot{E}|_i$, for $i = 1, 2, 3$). Source: the author.

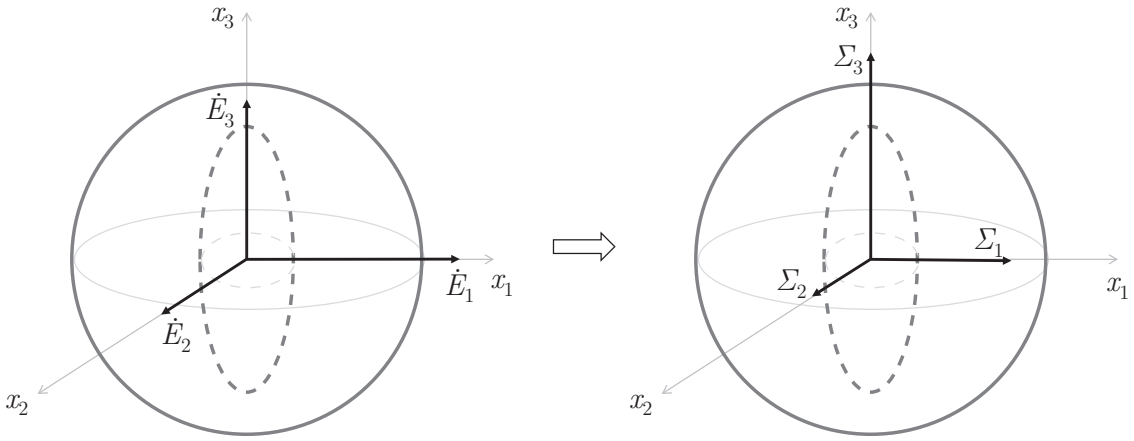

(a) principal directions of $\dot{\boldsymbol{E}}$ coincident with the referential $(\boldsymbol{e}_1, \boldsymbol{e}_2, \boldsymbol{e}_3)$

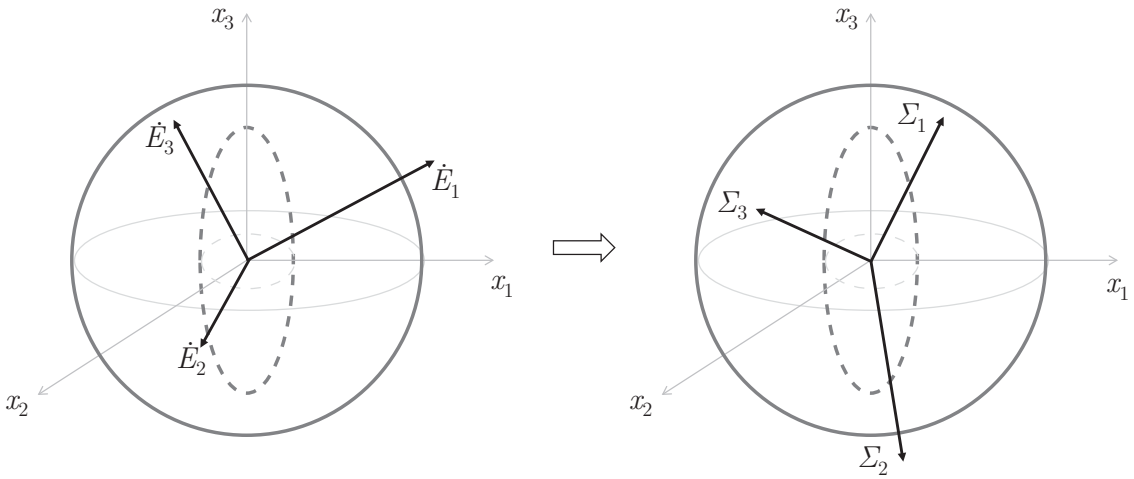

(b) principal directions of $\dot{\boldsymbol{E}}$ not coincident with the referential $(\boldsymbol{e}_1, \boldsymbol{e}_2, \boldsymbol{e}_3)$

Figure 19: Illustration of the influence of the principal directions of the macroscopic strain rate $\dot{\boldsymbol{E}}$ on the macroscopic stress $\boldsymbol{\Sigma}$ for spherical RVEs containing a centered ellipsoidal void.

Fig. 19b illustrates that the principal directions of the macroscopic strain rate $\dot{\boldsymbol{E}}$ do not necessarily coincide with those of the macroscopic stress $\boldsymbol{\Sigma}$ (i.e. $\Sigma_i/|\Sigma_i| \not\equiv \dot{E}_i/|\dot{E}|_i$, for at least one value of $i \in \{1, 2, 3\}$). This coincidence is only assured if $\dot{\boldsymbol{E}}$ is aligned with the void orientation, as in Fig. 19a. Source: the author.

Since the microscopic strain rate field is chosen to be the one proposed by Gurson (1977)

$$\dot{\boldsymbol{\epsilon}}(\dot{\boldsymbol{E}}, r, \varphi, \theta) = \dot{\boldsymbol{E}}' + \dot{E}_m \left(\frac{R}{r}\right)^3 \left[\mathbf{1} - 3\boldsymbol{e}_r(\varphi, \theta) \otimes \boldsymbol{e}_r(\varphi, \theta)\right], \tag{4.17}$$

the derivative $\partial\dot{\boldsymbol{\epsilon}}/\partial\dot{\boldsymbol{E}}$ is obtained intrinsically in terms of $\dot{\boldsymbol{E}}$ as

$$\frac{\partial\dot{\boldsymbol{\epsilon}}}{\partial\dot{\boldsymbol{E}}} = \mathbb{J} + \frac{1}{3}\left(\frac{R}{r}\right)^3 \mathbf{1} \otimes \left\{\mathbf{1} - 3\left[\boldsymbol{e}_r(\varphi, \theta) \otimes \boldsymbol{e}_r(\varphi, \theta)\right]\right\} \tag{4.18}$$

where r is the radius measured from the center point fo the RVE, $\varphi \in [0, 2\pi]$ is the azimuth angle and $\theta \in [0, \pi]$ is the zenith angle, all of them referring to a spherical coordinate system as illustrated in Fig. 10 and

$$\mathbb{J} = \left[\frac{1}{2}(\delta_{ik}\delta_{jl} + \delta_{il}\delta_{jk}) - \frac{1}{3}\delta_{ij}\delta_{kl}\right](\boldsymbol{e}_i \otimes \boldsymbol{e}_j \otimes \boldsymbol{e}_k \otimes \boldsymbol{e}_l). \tag{4.19}$$

One important remark is that the choice of the trial velocity field of Gurson (1977), given by either Eq. (4.17) or (3.49), is a first attempt with the aim of providing a rigorous upper bound approximation to the effective criterion. Further developments with more refined trial velocity fields are previewed in the next steps of the research. For example, (i) the field proposed by Monchiet and Kondo (2012), which is the exact solution of a spherical porous RVE whose material matrix obeys the Hill-Schleicher yield criterion; (ii) the Eshelby (1957) field, in a similar way to Monchiet, Charkaluk and Kondo (2007) and Monchiet, Charkaluk and Kondo (2011); or even (iii) the class of admissible fields given by Leblond and Gologanu (2008) for ellipsoidal RVEs containing confocal ellipsoidal voids. Furthermore, the exact solution of an elastic spherical RVE with a centered spherical inclusion given by Li, Sauer and Wang (2007) – and applied in homogenization procedures by Li, Wang and Sauer (2007) – can also be particularized to the condition of Poisson's coefficient $\nu = 1/2$ to represent the incompressibility condition, similar to the way Benallal, Desmorat and Fournage (2014) explored it in part of their work.

The ellipsoidal morphology of the void requires the integration limits in Eq. (4.11) to be

$$\boldsymbol{\Sigma} = \frac{1}{V}\int_{\overline{\Omega}} \frac{\partial \pi}{\partial \dot{\boldsymbol{E}}} dV = \frac{1}{V}\int_0^{\pi}\int_0^{2\pi}\int_{r_v(\varphi,\theta)}^{R} \frac{\partial \pi}{\partial \dot{\boldsymbol{E}}} r^2 \sin\theta dr d\varphi d\theta \tag{4.20}$$

where $r_v(\varphi, \theta) \in \partial\Omega^-$ is a parametric function that represents the points on the void surface,

$$r_v(\varphi, \theta) = \frac{1}{\sqrt{\left(\dfrac{\cos\varphi \sin\theta}{r_1}\right)^2 + \left(\dfrac{\sin\varphi \sin\theta}{r_2}\right)^2 + \left(\dfrac{\cos\theta}{r_3}\right)^2}}. \tag{4.21}$$

Some details on the numerical implementation of Eq. (4.20) are presented in chapter 7, as well as the level set plots of macroscopic yield surfaces that are discussed in the next section.

4.4 Results and discussion

In order to illustrate the application of the formulation derived in former sections, several RVEs with different principal radii are hereby considered. The correspondent macroscopic yield surfaces are obtained from each of the morphologies listed in Tables 1

to 4. These tables contain the relative lengths (ℓ_1, ℓ_2, ℓ_3) and the principal radii (r_1, r_2, r_3) respectively to each of the ellipsoidal void (including its spherical and spheroidal particularizations) used throughout this section.

A porosity $f = 5\%$ is chosen to represent an arbitrary ductile rupture condition whereby the high deformation fields must lead the microscopical voids to be elongated or flatted in certain directions. Furthermore, this chosen value of porosity has also shown to adequately highlight the differences between properties of each morphology considered here. The other parameters that are assumed are (i) the Hershey-Hosford shape parameter $m = 8$, which refers to a FCC material matrix; (ii) the microscopic yield stress $\sigma_0 = 1$ (unitary) for the sake of simplicity; and (iii) the external radius $R = 1$ (unitary) of the RVE.

Table 1: Spherical voids of RVEs with porosity $f = 5\%$ and external radius $R = 1$ (unitary).

(ℓ_1, ℓ_2, ℓ_3)	r_1	r_2	r_3
(1,1,1)	0.368403	0.368403	0.368403

Source: the author.

Table 2: Prolate spheroidal voids of RVEs with porosity $f = 5\%$ and external radius $R = 1$ (unitary).

(ℓ_1, ℓ_2, ℓ_3)	r_1	r_2	r_3
(2,1,1)	0.584804	0.292402	0.292402
(3,1,1)	0.766309	0.255436	0.255436
(4,1,1)	0.928318	0.232079	0.232079
(1,4,1)	0.232079	0.928318	0.232079
(1,1,4)	0.232079	0.232079	0.928318

Source: the author.

Table 3: Oblate spheroidal voids of RVEs with porosity $f = 5\%$ and external radius $R = 1$ (unitary).

(ℓ_1, ℓ_2, ℓ_3)	r_1	r_2	r_3
(1,4,4)	0.146201	0.584804	0.584804
(1,8,8)	0.092101	0.736806	0.736806
(8,1,8)	0.736806	0.092101	0.736806
(8,8,1)	0.736806	0.736806	0.092101

Source: the author.

The first set of analyses consists of macroscopic yield surfaces obtained from spherical RVEs (as in Fig. 17) with three different void morphologies in it. The first

Table 4: Ellipsoidal voids of RVEs with porosity $f = 5\%$ and external radius $R = 1$ (unitary).

(ℓ_1, ℓ_2, ℓ_3)	r_1	r_2	r_3
(1,2,4)	0.184202	0.368403	0.736806
(1,4,8)	0.116040	0.464159	0.928318
(4,8,1)	0.464159	0.928318	0.116040
(8,1,4)	0.928318	0.116040	0.464159

Source: the author.

morphology type concerns elongated voids and is represented by a (4,1,1) prolate spheroid in Fig. 20. The second one is related to flattened voids, which are represented by an (1,8,8) oblate spheroid in Fig. 21. Finally, with the aim of representing the class of arbitrary ellipsoidal voids in Fig. 22, an (1,4,8) ellipsoid is chosen.

As shown in Fig. 20a-22a, the deviatoric planes $\Sigma_m^f = 0$ coincide with the respective isotropic reference. This fact indicates that the present approach is not able to capture any anisotropic effect for $\Sigma_m^f = 0$, regardless the morphology considered. This limitation arises from the choice of Gurson's microscopic strain rate field $\dot{\boldsymbol{\epsilon}}$ (Eq. (4.17)), since $\dot{E}_m \to 0 \implies \dot{\boldsymbol{\epsilon}}(\dot{\boldsymbol{E}}, r, \varphi, \theta) = \dot{\boldsymbol{\epsilon}}(\dot{\boldsymbol{E}}) = \dot{\boldsymbol{E}}'$. This means that, for any traceless macroscopic strain rate $\dot{\boldsymbol{E}} = \dot{\boldsymbol{E}}'$, the microscopic one $\dot{\boldsymbol{\epsilon}}$ is uniform in Ω. Hence, the choice of $\dot{\boldsymbol{\epsilon}}$ prevents Eq. (4.11) of obtaining any influence of the void morphology.

The macroscopic yield surfaces in Fig. 20 and 21 suggest that spherical RVEs with spheroidal voids mechanically behave as transversely isotropic materials. In a similar way, Fig. 22 indicates the presence of orthotropic symmetries in the macroscopic yield surface resultant of spherical RVEs with ellipsoidal voids. These observations are in agreement with geometrical configurations of the RVEs presented in Fig. 17 and put forward the consistency of the present formulation.

Although the meridional planes in Fig. 20b-22b do not exhibit any significant discrepancy between different levels of θ, a slight vertical asymmetry might be noticed. Albeit discreet, this effect illustrates the influence of the anisotropy induced by the void morphology also on the meridional planes of the macroscopic yield surfaces.

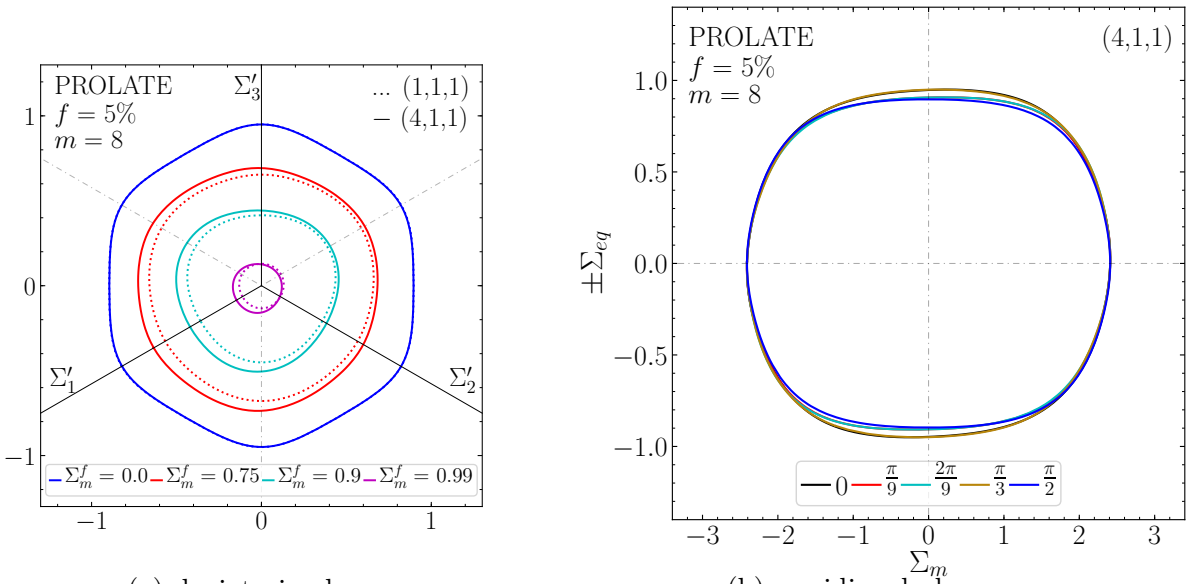

(a) deviatoric planes (b) meridional planes

Figure 20: Macroscopic yield surface obtained from a spherical RVE with a prolate spheroidal void.

Contour plots for different levels of (a) $\Sigma^f_m = \Sigma_m/|\Sigma_m|_{max}$, taking a spherical void $(1,1,1)$ as an isotropic reference (dotted lines); and (b) macroscopic stress Lode angle Θ ($\Sigma_{eq} \geq 0$) and $\Theta + \pi$ ($\Sigma_{eq} < 0$). One assumes $\sigma_0 = 1$ for the sake of simplicity. Source: the author.

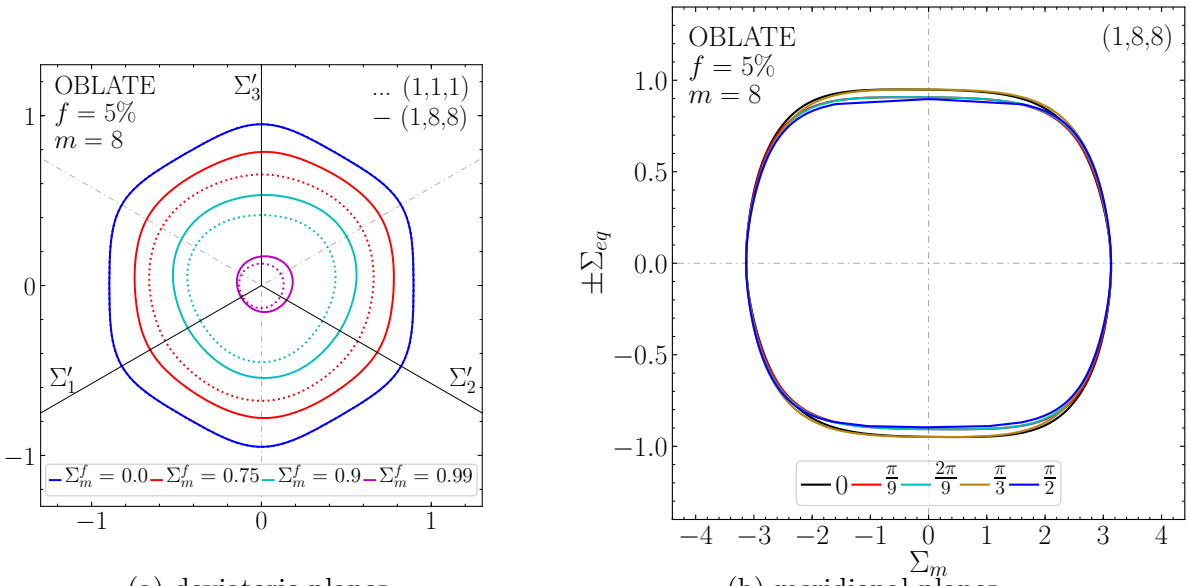

(a) deviatoric planes (b) meridional planes

Figure 21: Macroscopic yield surface obtained from a spherical RVE with an oblate spheroidal void.

Contour plots for different levels of (a) $\Sigma^f_m = \Sigma_m/|\Sigma_m|_{max}$, taking a spherical void $(1,1,1)$ as an isotropic reference (dotted lines); and (b) macroscopic stress Lode angle Θ ($\Sigma_{eq} \geq 0$) and $\Theta + \pi$ ($\Sigma_{eq} < 0$). One assumes $\sigma_0 = 1$ for the sake of simplicity. Source: the author.

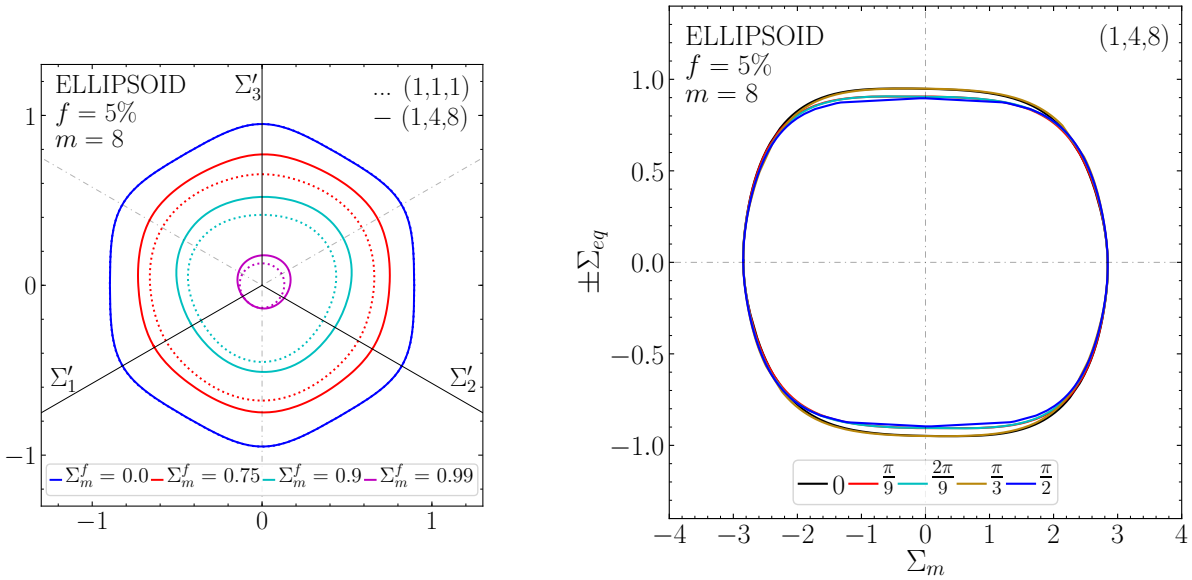

(a) deviatoric planes (b) meridional planes

Figure 22: Macroscopic yield surface obtained from a spherical RVE with an ellipsoidal void. Contour plots for different levels of (a) $\Sigma^f_m = \Sigma_m/|\Sigma_m|_{max}$, taking a spherical void $(1, 1, 1)$ as an isotropic reference (dotted lines); and (b) macroscopic stress Lode angle Θ ($\Sigma_{eq} \geq 0$) and $\Theta + \pi$ ($\Sigma_{eq} < 0$). One assumes $\sigma_0 = 1$ for the sake of simplicity. Source: the author.

The effects of different elongation aspects and orientations on prolate spheroidal, oblate spheroidal and ellipsoidal voids are explored in Fig. 23-25, respectively. In each of these figures, two types of comparisons on the deviatoric plane $\Sigma^f_m = \Sigma_m/|\Sigma_m|_{max} = 0.99$ are proposed. The first one investigates the effect of different relative lengths for the same type of void morphology and porosity. The second one considers three similar voids, whose each respective triple of relative lengths is a cyclic permutation of three fixed values. These permutations simulate the effect of rotating the void so that their resultant orientations are orthogonal to each other.

The elongation of voids in certain directions induced a gain of resistance on those respective directions, in accordance with Fig. 23a-25a. Since $\Sigma^f_m = 0.99 > 0$, it is expected that this gain of resistance would be noticed predominantly on the positive range of the axes on the deviatoric plane (i.e. Σ'_i). This fact is also confirmed in Fig. 23a-25a, which sustain the consistency of the present formulation.

Fig. 23b-25b show that curves related to void orientations that have a relative length in common for a certain direction coincide on its correspondent axis. This observation also illustrates the transversely isotropic and orthotropic behaviors that are induced by spheroidal and ellipsoidal voids, respectively. Moreover, the match of the curves precisely on the expected axis shows the accuracy and consistency of the present implementation.

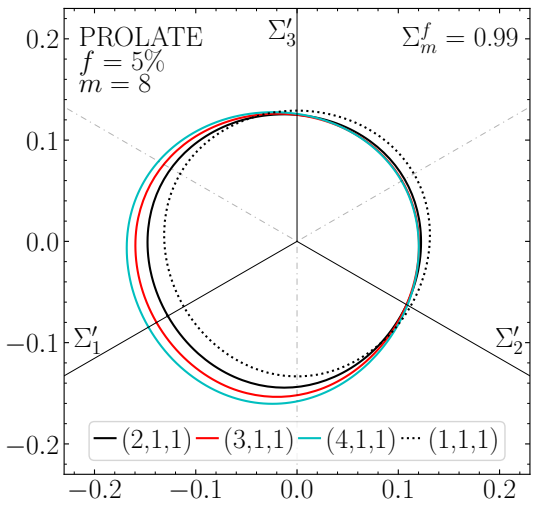

(a) Elongation comparison

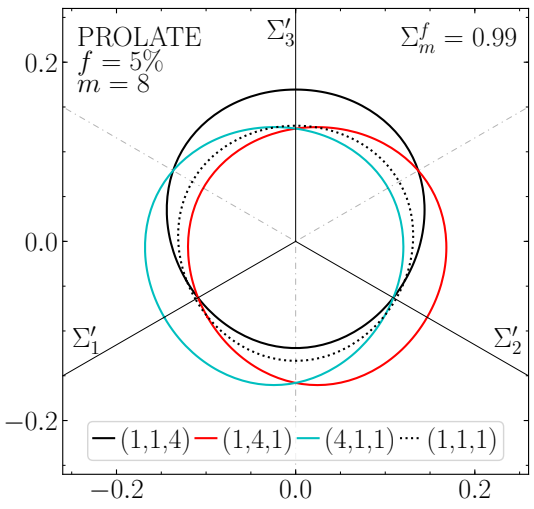

(b) Orientation comparison

Figure 23: Comparisons between deviatoric planes of macroscopic yield surfaces obtained from spherical RVEs with different prolate spheroidal voids.

Contour plots of $\Sigma^f_m = \Sigma_m/|\Sigma_m|_{max} = 0.99$. A spherical void $(1, 1, 1)$ as an isotropic reference (dotted lines). One assumes the microscopic yield stress $\sigma_0 = 1$ for the sake of simplicity. Source: the author.

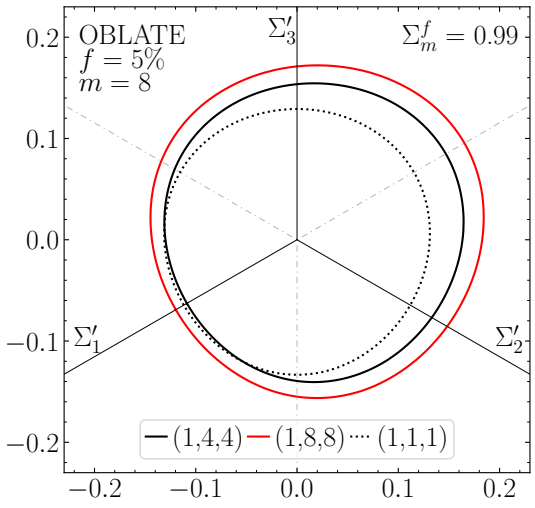

(a) Elongation comparison

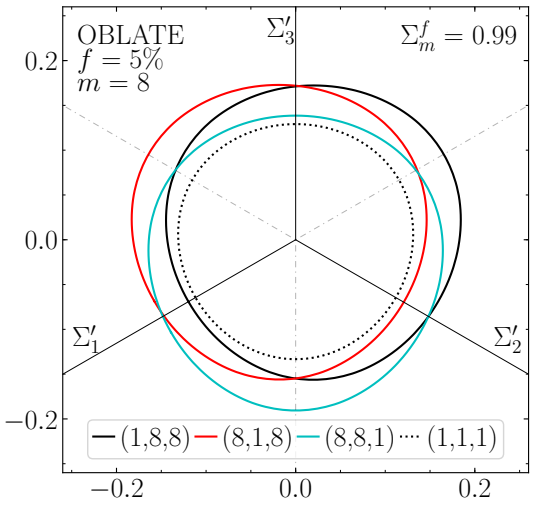

(b) Orientation comparison

Figure 24: Comparisons between deviatoric planes of macroscopic yield surfaces obtained from spherical RVEs with different oblate spheroidal voids.

Contour plots of $\Sigma^f_m = \Sigma_m/|\Sigma_m|_{max} = 0.99$. A spherical void $(1, 1, 1)$ as an isotropic reference (dotted lines). One assumes the microscopic yield stress $\sigma_0 = 1$ for the sake of simplicity. Source: the author.

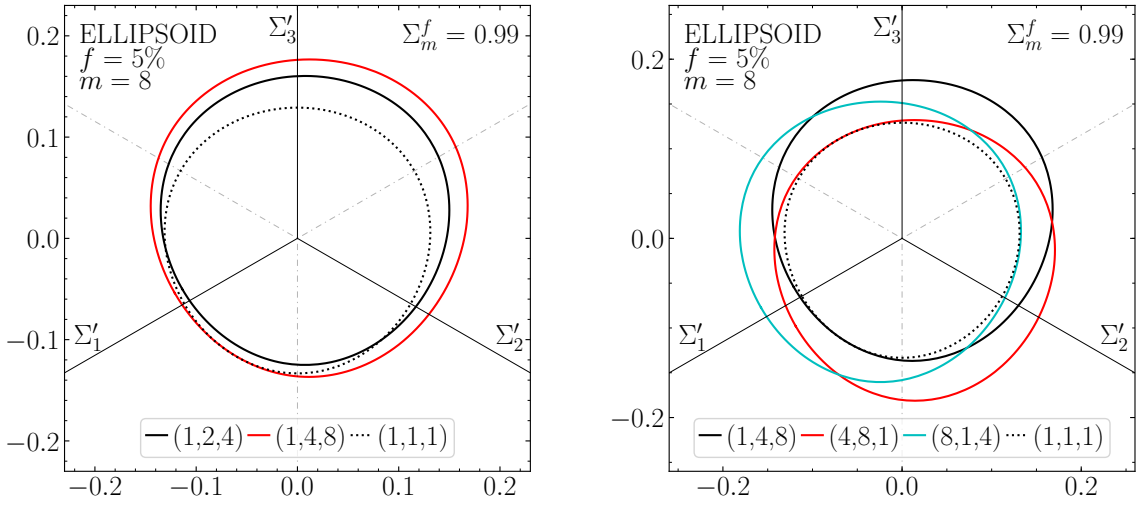

(a) Elongation comparison

(b) Orientation comparison

Figure 25: Comparisons between deviatoric planes of macroscopic yield surfaces obtained from spherical RVEs with different ellipsoidal voids

Contour plots of $\Sigma^f_m = \Sigma_m/|\Sigma_m|_{max} = 0.99$. The isotropic reference $(1, 1, 1)$ is shown as a dotted line. One assumes the microscopic yield stress $\sigma_0 = 1$ for the sake of simplicity. Source: the author.

4.5 Concluding remarks

This chapter has presented a simple way of treating morphology-induced anisotropy on ductile porous materials. The choice of Gurson's trial velocity field and spherical RVE facilitated the analytical developments and possibly its further implementation in multiscale FEM codes. However, this choice limited the anisotropic effects to high triaxialities, which encourages the search for more representative approximations to the trial velocity field and for alternative approaches of modeling anisotropy in ductile failure.

Although it was not possible to derive a closed-form expression for the yield criterion, the development of high-performance scientific computing makes multiscale FEM codes feasible nowadays. Thus, a yield criterion written in an integral form can still be successfully implemented in FEM codes with the advantage of not penalizing the analytical development with further simplifications.

The results obtained in the form of macroscopic yield surfaces have shown to be consistent. Moreover, the identification of transversely isotropic and orthotropy symmetries in the results related to spheroidal and ellipsoidal voids, respectively, unveiled the accuracy of the present implementation. However, further work is required to validate the formulation hereby presented with experimental studies.

5 EFFECTIVE YIELD CRITERIA FOR POROUS ANISOTROPIC MEDIA

This chapter proposes an anisotropic yield criterion for porous ductile materials. The approach consists of representing the morphological microstructure properties by defining a spherical RVE containing a centered spherical void. The material matrix surrounding this void is assumed to be continuous and follows an anisotropic yield criterion proposed by Karafillis and Boyce (1993). A uniform macroscopic strain rate $\dot{\boldsymbol{E}}$ at the external surface of the RVE and a traction-free prescription are imposed as boundary conditions to the RVE problem. The classical Gurson's trial velocity field is chosen to compose the microscopic strain rate as a first attempt, which approximates the solution to the RVE mechanical problem and performs a rigorous upper bound solution to it. The effect of different morphologies of the void is not considered in the following analysis so that any perceptible effect of anisotropy is due exclusively to the matrix behavior. Numerical simulations are hereby presented for four different symmetries of porous ductile materials: Cubic, Transversely Isotropic, Tetragonal and Orthotropic. These results highlight the consistency of the present approach representing the yield criterion of ductile porous materials whose microstructures present specific crystal symmetries.

5.1 The concept of an Isotropic Plastic Equivalent material

Classical yield criteria for anisotropic continuum media have been proposed since Hill (1948), who altered the equivalent stresses of criteria for isotropic criteria (e.g. the von Mises stress) were modified in a certain mathematical way to insert new material coefficients to be experimentally determined. Although this class of yield criteria has been largely used so far in the literature, these approaches usually lack the physical meaning of each coefficient. Besides, the formulations related to these criteria end up being considerably more complex than the classical isotropic ones, as well as being particularized for specific crystal symmetries.

Karafillis and Boyce (1993) proposed a more convenient treatment for formulating yield criteria for anisotropic continuum media, which is based on the concept of an Isotropic Plastic Equivalent (IPE) material. This fictitious IPE material is assumed to undergo auxiliary stress states $\boldsymbol{s}^*$, which are defined by applying a linear transformation $\mathbb{L}$ on the true Cauchy stress tensor $\boldsymbol{\sigma}$, Eq. (5.1). Since stress states are mathematically represented by second-order tensors, the linear transformation $\mathbb{L}$ is defined as a fourth-order one.

$$\boldsymbol{s}^* = \mathbb{L} : \boldsymbol{\sigma} \tag{5.1}$$

The usefulness of the definition of the auxiliary stress tensors relies on the property that an affine transformation preserves convexity (EGGLESTON, 1958). Following this property of convex functions, Karafillis and Boyce (1993) realized that the convexity of an isotropic yield criterion is preserved if its argument, which is a Cauchy true stress tensor $\boldsymbol{\sigma}$, is linearly transformed by the operator $\mathbb{L}$, as in Eq. (5.1). Therefore, since the symmetries of the operator $\mathbb{L}$ might imply a rotation of the principal directions of $\boldsymbol{\sigma}$, an anisotropic yield criterion ψ on the variable $\boldsymbol{\sigma}$ can be defined by an equivalent isotropic one, ϕ, on the auxiliary stress tensor $\boldsymbol{s}^*$, as shown in Eq. (5.2). In other words, an anisotropic yield criterion can be equivalently obtained by using an already known isotropic one, which is then related to an IPE material.

$$\psi(\boldsymbol{\sigma}) = \phi(\boldsymbol{s}^*) = \phi(\mathbb{L} : \boldsymbol{\sigma}) \tag{5.2}$$

The linear operator $\mathbb{L}$ definition requires three general conditions. The first one arises from guaranteeing the symmetry of both $\boldsymbol{\sigma}$ and $\boldsymbol{s}^*$, which implies in the so-called minor symmetry of fourth-order tensors: $\mathbb{L}_{ijkl} = \mathbb{L}_{jikl} = \mathbb{L}_{jilk}$. The second condition minimizes the number of needed anisotropy coefficients to represent an arbitrary crystal symmetry and implies the so-called big symmetry of fourth-order tensors: $\mathbb{L}_{ijkl} = \mathbb{L}_{klij}$. Finally, the last condition is a consequence of the necessity that $\boldsymbol{s}^*$ is traceless regardless of the anisotropy parameters, so that the linear transformation operated by $\mathbb{L}$ over $\boldsymbol{\sigma}$ be defined in the deviatoric space: $\mathbb{L}_{ijkk} = 0$, where implicit sum applies.

The symmetries hereupon cited allow to represent Eq. (5.1) in Voigt notation (see Appendix A) by considering a system of six equations, as shown in Eq. (5.3). The stress tensors $\boldsymbol{\sigma}$ and $\boldsymbol{s}^*$, as well as the linear operator $\mathbb{L}^*$ are depicted as (6×1) vectors and a (6×6) matrix, respectively. Due to major symmetry of $\mathbb{L}$, $\underline{\underline{\boldsymbol{L}}}$ is a symmetric matrix.

$$\begin{Bmatrix} s^*_{11} \\ s^*_{22} \\ s^*_{33} \\ \sqrt{2}s^*_{23} \\ \sqrt{2}s^*_{31} \\ \sqrt{2}s^*_{12} \end{Bmatrix} = \begin{bmatrix} L_{1111} & L_{1122} & L_{1133} & \sqrt{2}L_{1123} & \sqrt{2}L_{1131} & \sqrt{2}L_{1112} \\ L_{1122} & L_{2222} & L_{2233} & \sqrt{2}L_{2223} & \sqrt{2}L_{2231} & \sqrt{2}L_{2212} \\ L_{1133} & L_{2233} & L_{3333} & \sqrt{2}L_{3323} & \sqrt{2}L_{3331} & \sqrt{2}L_{3312} \\ \sqrt{2}L_{1123} & \sqrt{2}L_{2223} & \sqrt{2}L_{3323} & 2L_{2323} & 2L_{2331} & 2L_{2312} \\ \sqrt{2}L_{1131} & \sqrt{2}L_{2231} & \sqrt{2}L_{3331} & 2L_{2331} & 2L_{3131} & 2L_{3112} \\ \sqrt{2}L_{1112} & \sqrt{2}L_{2212} & \sqrt{2}L_{3312} & 2L_{2312} & 2L_{3112} & 2L_{1212} \end{bmatrix} \begin{Bmatrix} \sigma_{11} \\ \sigma_{22} \\ \sigma_{33} \\ \sqrt{2}\sigma_{23} \\ \sqrt{2}\sigma_{31} \\ \sqrt{2}\sigma_{12} \end{Bmatrix} \tag{5.3}$$

The matrix $\underline{\underline{\boldsymbol{L}}}$ in Eq. (5.3) is particularized to orthotropic symmetries in its irreducible form in Eq. (5.4). The condition $\mathbb{L}_{ijkk} = 0$ implies the relations provided by

Eq. (5.5).

$$\underline{\underline{\boldsymbol{L}}} = C \begin{bmatrix} L_{11} & L_{12} & L_{13} & 0 & 0 & 0 \\ L_{12} & L_{22} & L_{23} & 0 & 0 & 0 \\ L_{13} & L_{23} & L_{33} & 0 & 0 & 0 \\ 0 & 0 & 0 & 2L_{44} & 0 & 0 \\ 0 & 0 & 0 & 0 & 2L_{55} & 0 \\ 0 & 0 & 0 & 0 & 0 & 2L_{66} \end{bmatrix}, \tag{5.4}$$

where

$$\begin{aligned} L_{12} &= \frac{L_{33} - L_{11} - L_{22}}{2} \\ L_{13} &= \frac{L_{22} - L_{33} - L_{11}}{2} \\ L_{23} &= \frac{L_{11} - L_{22} - L_{33}}{2}. \end{aligned} \tag{5.5}$$

In the following sections, the concept of IPE materials is used to formulate anisotropic yield criterion having as a basis the Hershey-Hosford isotropic function (Eq.(3.63)). The resultant anisotropic criterion, Eq. (5.6) is then used as the microscopic yield function of the material matrix surrounding the RVE spherical void.

$$\phi(S_1^*, S_2^*, S_3^*) = \left\{ \frac{1}{2} \left[(S_1^* - S_2^*)^m + (S_1^* - S_2^*)^m + (S_1^* - S_2^*)^m \right] \right\}^{1/m} \tag{5.6}$$

5.2 A Gurson-like RVE for modeling porous anisotropic media

Although the framework proposed by Karafillis and Boyce (1993) has been widely and successfully accepted by the literature as an adequate manner to formulate anisotropic yield criteria, it does not include the effect of porosity in microstructures. This effect, however, plays an important role on ductile rupture phenomena according to several experimental studies ((ARGON; IM; SAFOGLU, 1975), (ARGON; IM, 1975), (ARGON, 1976), (ROZOVSKY; HAHN; AVITZUR, 1973), (BEREMIN, 1981)).

In order to overcome this drawback, the present work proposes an approach for considering the effect of porosity on ductile rupture modeling. For this purpose, a spherical RVE containing a centered and also spherical void is assumed to represent the porosity contained in the microstructure of an arbitrary ductile material. The material matrix surrounding the spherical void is then assumed to follow the yield criterion of Eq. (5.6). Since only centered spherical voids are hereby considered, any noticeable anisotropic behavior is certainly due to the yield criterion of the material matrix. An illustration of the RVE conception is put forward in Fig. 26.

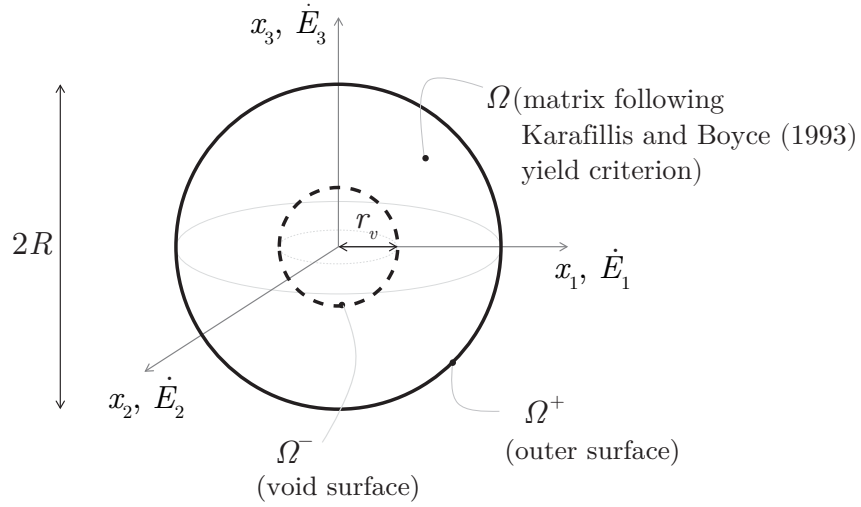

Figure 26: The Gurson-like RVE chosen for modeling anisotropic porous ductile materials.

The material matrix in Ω is assumed to follow the Karafillis and Boyce (1993) anisotropic yield criterion. Source: the author.

The material matrix contained in the domain Ω is assumed to be continuous and to follow the plastic model described in Eq. (5.7), which corresponds to (a) the yield criterion, (b) the associated flow rule, (c) the consistency condition and (d) the irreversibility condition.

$$\phi(\boldsymbol{s}^*) - \sigma_0 \leq 0 \tag{5.7a}$$

$$\dot{\boldsymbol{\epsilon}}^* = \dot{\lambda}\frac{\partial \phi}{\partial \boldsymbol{s}^*} \tag{5.7b}$$

$$\dot{\lambda}\phi(\boldsymbol{s}^*) = 0 \tag{5.7c}$$

$$\dot{\lambda} \geq 0 \tag{5.7d}$$

The attachment between the RVE and its microscopic vicinities is approximated by the prescription of a uniform macroscopic strain rate $\dot{\boldsymbol{E}}$, described in Eq. (3.28), in $\partial\Omega^+$ (see Fig. 26). Furthermore, the inner surface ($\partial\Omega^-$) of the RVE is assumed to be traction-free. Eq. (5.8) summarizes these last boundary conditions below:

$$\dot{\boldsymbol{u}} = \dot{\boldsymbol{E}}\boldsymbol{x} \qquad \forall \boldsymbol{x} \quad on \quad \partial\Omega^+, \tag{5.8a}$$

$$\boldsymbol{\Sigma}\boldsymbol{n}(\boldsymbol{x}) = 0 \qquad \forall \boldsymbol{x} \quad on \quad \partial\Omega^-, \tag{5.8b}$$

where $\boldsymbol{n}(\boldsymbol{x})$ is the normal vector to the inner surface $\partial\Omega^-$ and $\boldsymbol{\Sigma}$ is the resultant macroscopic stress tensor.

As will be discussed later on, the solution of the problem defined by the RVE that undergoes the hereupon conditions is approximated in the sense of Gurson (1977).

According to this work, a convenient upper bound approach consists of taking a trial velocity field $\dot{\boldsymbol{u}}_G(x)$, for $x \in \Omega$, as the solution to the RVE problem. This trial velocity field is kinematically admissible (i.e., it matches external boundary conditions: $\dot{\boldsymbol{u}}_G(x) = \dot{\boldsymbol{E}}\boldsymbol{x}$, for $\boldsymbol{x} \in \partial\Omega^+$) and finally gives rise to the classical Gurson's trial strain rate field $\dot{\boldsymbol{\epsilon}}_G$, as in Eq. (5.9).

$$\dot{\boldsymbol{\epsilon}}_G(\dot{\boldsymbol{E}}, r, \varphi, \theta) = \dot{\boldsymbol{E}}' + \dot{E}_m \left(\frac{R}{r}\right)^3 (\mathbf{1} - 3\boldsymbol{e}_r(\varphi,\theta) \otimes \boldsymbol{e}_r(\varphi,\theta)) \tag{5.9}$$

where r, φ and θ are respectively the radius, the polar angle and the azimuthal angle associated to the spherical coordinate system, as illustrated in Fig. 10.

It is important to highlight that the choice of the trial velocity field of Gurson (1977) consists of a first attempt to obtain an upper bound approximation to the effective criterion. More refined trial velocity fields are required in the next steps of research. For instance, the field proposed by Monchiet and Kondo (2012), which is the exact solution of a spherical porous RVE whose material matrix obeys the Hill-Schleicher yield criterion can be particularized to a RVE whose matrix follows an incompressible plastic flow rule. Additionally, the exact solution of an elastic spherical RVE with a centered and also spherical inclusion given by Li, Sauer and Wang (2007) may be particularized to the condition of Poisson's coefficient $\nu = 1/2$ – to represent the incompressibility condition – and to the case where the inclusion offers no stiffness to the RVE – to consider a void instead of an inclusion.

In the sense of Karafillis and Boyce (1993), a trial strain rate field associated to the concept of an IPE material can be deduced by combining both normality rules concerning the actual strain rate $\dot{\boldsymbol{\epsilon}} = \dot{\lambda}\partial\phi/\partial\boldsymbol{\sigma}$ and $\dot{\boldsymbol{\epsilon}}^* = \partial\phi/\partial\boldsymbol{s}^*$ with Eq. (5.1), as in Eq. (5.10).

$$\dot{\boldsymbol{\epsilon}}^* = \dot{\lambda}\frac{\partial\phi}{\partial\boldsymbol{s}^*} = \dot{\lambda}\frac{\partial\phi}{\partial\boldsymbol{\sigma}} : \frac{\partial\boldsymbol{\sigma}}{\partial\boldsymbol{s}^*} = \dot{\boldsymbol{\epsilon}} : \mathbb{L}^+ \tag{5.10}$$

where $\mathbb{L}^+$ represents the inverse of the fourth-order tensor $\mathbb{L}$ with respect to the deviatoric space.

Thus, the trial velocity field $\dot{\boldsymbol{\epsilon}}^*(\dot{\boldsymbol{E}}^*, r, \varphi\theta)$ concerning the IPE material in the RVE domain Ω is then defined as

$$\dot{\boldsymbol{\epsilon}}^*(\dot{\boldsymbol{E}}, r, \varphi\theta) = \dot{\boldsymbol{\epsilon}} : \mathbb{L}^+ = \dot{\boldsymbol{E}}' : \mathbb{L}^+ + \dot{E}_m \left(\frac{R}{r}\right)^3 (\mathbf{1} - 3\boldsymbol{e}_r(\varphi,\theta) \otimes \boldsymbol{e}_r(\varphi,\theta)) : \mathbb{L}^+ \tag{5.11}$$

In an equivalent manner, a macroscopic IPE material is conveniently idealized. For this purpose, a macroscopic IPE strain rate field is defined as

$$\dot{\boldsymbol{E}}^* = \dot{\boldsymbol{E}}' : \mathbb{L}^+ + \dot{E}_m \mathbf{1}. \tag{5.12}$$

This definition operates a linear transformation only over the deviator $\dot{\boldsymbol{E}}'$, while the hydrostatic parcel $\dot{E}_m\mathbf{1}$ is taken without any changes.

Regarding $\dot{\boldsymbol{E}}^*$, its deviatoric parcel $\dot{\boldsymbol{E}}^{*'}$, Lode angle η^*, equivalent measure E^*_{eq} and unitary deviatoric parcel $\boldsymbol{e}^{*'}$ are

$$\dot{\boldsymbol{E}}^{*'} = \dot{\boldsymbol{E}}^* - \dot{E}_m\mathbf{1} = E^*_{eq}\boldsymbol{e}^{*'}, \tag{5.13}$$

$$E^*_{eq} = \sqrt{\frac{3}{2}\dot{\boldsymbol{E}}^{*'}\dot{\boldsymbol{E}}^{*'}}, \tag{5.14}$$

$$\boldsymbol{e}^{*'} = \begin{bmatrix} \cos\eta^* & 0 & 0 \\ 0 & \cos\left(\eta^* - \dfrac{2\pi}{3}\right) & 0 \\ 0 & 0 & \cos\left(\eta^* + \dfrac{2\pi}{3}\right) \end{bmatrix} \tag{5.15}$$

and

$$\eta^* = \frac{1}{3}\arccos\left(\frac{4\det\dot{\boldsymbol{E}}^{*'}}{(E^*_{eq})^3}\right). \tag{5.16}$$

5.3 Deduction of the macroscopic dissipation potential

The microscopic plastic dissipation potential π associated to a point in RVE domain Ω whose plastic laws hold Eq. (5.7) is defined in Eq. (5.17). It can be defined as a function of the incompressible (i.e. $\operatorname{Tr}\dot{\boldsymbol{\epsilon}} = 0$) microscopic strain rate field $\dot{\boldsymbol{\epsilon}}$ as

$$\pi(\dot{\boldsymbol{\epsilon}}) = \sup_{\sigma\in\Upsilon}\{\boldsymbol{\sigma} : \dot{\boldsymbol{\epsilon}}\} \tag{5.17}$$

where $\Upsilon = \{\boldsymbol{\sigma}|\psi(\boldsymbol{\sigma}) = \phi(\boldsymbol{s}^*) \leq \sigma_0\}$ is a convex set of stress tensors $\boldsymbol{\sigma}$.

Considering the normality rule for the flow of the microscopic plastic strain rate $\dot{\boldsymbol{\epsilon}} = \dot{\lambda}\partial\psi/\partial\boldsymbol{\sigma}$ and the fact that the yield function $\psi(\boldsymbol{\sigma})$ is a homogeneous function of degree one, Eq. (5.17) can be rewritten as

$$\pi(\dot{\boldsymbol{\epsilon}}) = \boldsymbol{\sigma} : \left(\dot{\lambda}\frac{\partial\psi}{\partial\boldsymbol{\sigma}}\right) = \dot{\lambda}\boldsymbol{\sigma} : \frac{\partial\psi}{\partial\boldsymbol{\sigma}} = \dot{\lambda}\psi(\boldsymbol{\sigma}) = \dot{\lambda}\sigma_0, \tag{5.18}$$

An IPE microscopic strain rate $\dot{\boldsymbol{\epsilon}}^*$ as in Eq. (5.11) can be obtained by exploring the normality flow rule by doing

$$\dot{\boldsymbol{\epsilon}} = \dot{\lambda}\frac{\partial\psi}{\partial\boldsymbol{\sigma}} = \dot{\lambda}\frac{\partial\psi}{\partial\boldsymbol{s}^*} : \frac{\partial\boldsymbol{s}^*}{\partial\boldsymbol{\sigma}} = \dot{\lambda}\frac{\partial\phi}{\partial\boldsymbol{s}^*} : \mathbb{L} = \dot{\boldsymbol{\epsilon}}^* : \mathbb{L}, \tag{5.19}$$

where

$$\dot{\boldsymbol{\epsilon}}^* = \dot{\lambda}\frac{\partial \phi}{\partial \boldsymbol{s}^*} = \dot{\boldsymbol{\epsilon}} : \mathbb{L}^+. \tag{5.20}$$

At this point, one assumes that $\mathbb{L}$ has an inverse $\mathbb{L}^+$. Because $\mathbb{L}_{ijkk} = 0$ (pressure independence condition), its inverse $\mathbb{L}^+$ satisfies $\mathbb{L} : \mathbb{L}^+ = \mathbb{J}$, where $\mathbb{J}$ is the deviatoric fourth-order identity defined in Eq. (4.19).

The plastic multiplier rate $\dot{\lambda}$ is obtained as a function of the IPE microscopic strain rate $\dot{\boldsymbol{\epsilon}}^*$ by considering its definition in Eq. (5.20) as

$$\dot{\lambda} = \frac{\dot{\epsilon}^*_{eq}}{\sqrt{\frac{2}{3}\frac{\partial \phi}{\partial \boldsymbol{s}^*} : \frac{\partial \phi}{\partial \boldsymbol{s}^*}}} \tag{5.21}$$

where $\dot{\epsilon}^*_{eq} = \sqrt{\frac{2}{3}\dot{\boldsymbol{\epsilon}}^* : \dot{\boldsymbol{\epsilon}}^*}$.

Let us now consider the particular case of the Hershey-Hosford yield function, Eq. (5.6). The definitions of the deviatoric parcel of principal values of $\boldsymbol{s}^*$

$$\begin{aligned} S_1^* &= \frac{2}{3}s^*_{eq}\cos\left(\omega^*\right) \\ S_2^* &= \frac{2}{3}s^*_{eq}\cos\left(\omega^* - \frac{2\pi}{3}\right) \\ S_3^* &= \frac{2}{3}s^*_{eq}\cos\left(\omega^* + \frac{2\pi}{3}\right) \end{aligned} \tag{5.22}$$

lead us to rewrite that yield criterion as a function of the microscopic stress Lode angle ω^* and of the microscopic von Mises measure of stress, both related to the IPE material defined in the RVE domain Ω as

$$\begin{aligned} \phi(S_1^*, S_2^*, S_3^*) &= \left\{\frac{1}{2}\left[(S_1^* - S_2^*)^m + (S_2^* - S_3^*)^m + (S_3^* - S_1^*)^m\right]\right\}^{1/m} \\ &= s^*_{eq}\frac{2}{3}\left\{\frac{1}{2}\Big[(\cos\omega_1^* - \cos\omega_2^*)^m + \right. \\ &\qquad (\cos\omega_2^* - \cos\omega_3^*)^m + \\ &\qquad \left.(\cos\omega_3^* - \cos\omega_1^*)^m\Big]\right\}^{1/m} \end{aligned} \tag{5.23}$$

where

$$s^*_{eq} = \sqrt{\frac{3}{2}\boldsymbol{s}^* : \boldsymbol{s}^*} \tag{5.24}$$

and

$$g(\omega^*) = \frac{2}{3}\Bigg\{\frac{1}{2}\Big[(\cos\omega_1^* - \cos\omega_2^*)^m + (\cos\omega_2^* - \cos\omega_3^*)^m + (\cos\omega_3^* - \cos\omega_1^*)^m\Big]\Bigg\}^{1/m} \tag{5.25}$$

with

$$\begin{aligned} \omega_1^* &= \omega^*, \\ \omega_2^* &= \omega^* - \frac{2\pi}{3}, \\ \omega_3^* &= \omega^* + \frac{2\pi}{3}. \end{aligned} \tag{5.26}$$

The definition of the plastic multiplier $\dot{\lambda}$ in Eq. (5.21) requires, however, the derivative $\partial\phi/\partial\boldsymbol{s}^*$, which is presented hereafter. The analytical demonstration of the formulae below are omitted here for the sake of conciseness.

$$\frac{\partial\phi}{\partial\boldsymbol{s}^*} = \frac{\partial s_{eq}^*}{\partial\boldsymbol{s}^*} g(\omega^*) + s_{eq}^* \frac{\partial g}{\partial\omega^*}\frac{\partial\omega^*}{\partial\boldsymbol{s}^*}, \tag{5.27}$$

where

$$\frac{\partial s_{eq}^*}{\partial\boldsymbol{s}^*} = \frac{3}{2}\frac{\boldsymbol{s}^*}{s_{eq}^*}, \tag{5.28}$$

$$\begin{aligned} \frac{\partial g}{\partial\omega^*} = -\frac{1}{3}\frac{g(\omega^*)}{g^m(\omega^*)}\Big[&(\cos\omega_1^* - \cos\omega_2^*)^{m-1}(\sin\omega_1^* - \sin\omega_2^*) + \\ &(\cos\omega_2^* - \cos\omega_3^*)^{m-1}(\sin\omega_2^* - \sin\omega_3^*) + \\ &(\cos\omega_3^* - \cos\omega_1^*)^{m-1}(\sin\omega_3^* - \sin\omega_1^*)\Big] \end{aligned} \tag{5.29}$$

$$\frac{\partial\omega^*}{\partial\boldsymbol{s}^*} = -\frac{9}{2s_{eq}^*\sin 3\omega^*}\left[\left(\frac{\boldsymbol{s}^*}{s_{eq}^*}\right)^2 - \frac{2}{9}\mathbf{1} - \frac{1}{3}\cos 3\omega^*\left(\frac{\boldsymbol{s}^*}{s_{eq}^*}\right)\right]. \tag{5.30}$$

After intensive algebraic manipulation, the expression of the plastic multiplier $\dot{\lambda}$ can the be simplified to

$$\dot{\lambda} = \frac{\dot{\epsilon}_{eq}^*}{\sqrt{[g(\omega^*)]^2 + [g'(\omega^*)]^2}}, \tag{5.31}$$

which then finally leads to obtaining the expression of the microscopic plastic dissipation $\pi(\dot{\boldsymbol{\epsilon}}^*)$

$$\pi(\dot{\boldsymbol{\epsilon}}^*) = \sigma_0\dot{\epsilon}_{eq}^* \frac{1}{\sqrt{[g(\omega^*)]^2 + [g'(\omega^*)]^2}} = \tilde{\pi}(\dot{\epsilon}_{eq}^*)G(\omega^*), \tag{5.32}$$

where

$$\tilde{\pi}(\dot{\epsilon}^*_{eq}) = \sigma_0 \dot{\epsilon}^*_{eq} \tag{5.33}$$

and

$$G(\omega^*) \frac{1}{\sqrt{[g(\omega^*)]^2 + [g'(\omega^*)]^2}}. \tag{5.34}$$

Since the present work relies on the prescription of a chosen trial strain rate field $\dot{\boldsymbol{\epsilon}}^*$ to perform an upper bound approach, the expression of π must be dependent only on $\dot{\boldsymbol{\epsilon}}^*$. However, Eq. (5.32) states that the function $G(\omega^*)$ still has the microscopic stress Lode angle as an argument. The following paragraphs of this section show that, in fact, ω^* can be obtained from a prescribed $\dot{\boldsymbol{\epsilon}}^*$.

The definition of the microscopic strain Lode angle ξ^* combined to the normality rule in Eq. (5.19) gives rise to the relation between ξ^* and the derivative $\partial\phi/\partial\boldsymbol{s}^*$

$$\xi^* = \frac{1}{3}\arccos\left(\frac{4\det\dot{\boldsymbol{\epsilon}}^*}{(\dot{\epsilon}^*_{eq})^3}\right) = \frac{1}{3}\arccos\left(\frac{4\det\dfrac{\partial\phi}{\partial\boldsymbol{s}^*}}{\left(\dfrac{2}{3}\dfrac{\partial\phi}{\partial\boldsymbol{s}^*}:\dfrac{\partial\phi}{\partial\boldsymbol{s}^*}\right)^{3/2}}\right). \tag{5.35}$$

A full algebraic simplification procedure allows finally directly relates ξ^* to ω^* in Eq. (5.36). It is important to remark that, albeit the particularization of $\phi(\boldsymbol{s}^*)$ in Eq. (5.23), the following relation is defined for an arbitrary function $g(\omega^*)$ which satisfies the convexity condition in a polar coordinate system $g(\omega^*) + g''(\omega^*) \geq 0$.

$$\xi^* = \omega^* + \arctan\left(\frac{g'(\omega^*)}{g(\omega^*)}\right) \tag{5.36}$$

Although there is no explicit inverse relation of Eq. (5.36), a one-dimensional interpolation approximates a function $\omega^* \approx \omega^*(\xi^*)$. Consequently, the microscopic stress Lode angle ω^* can be numerically obtained from a prescribed microscopic strain rate $\dot{\boldsymbol{\epsilon}}^*$ and then

$$\pi(\dot{\boldsymbol{\epsilon}}^*) \approx \frac{\sigma_0 \dot{\epsilon}^*_{eq}}{\sqrt{[g(\xi^*)]^2 + [g'(\xi^*)]^2}} = \tilde{\pi}(\dot{\epsilon}^*_{eq}) G(\xi^*). \tag{5.37}$$

By definition, the macroscopic plastic dissipation potential $\mathit{\Pi}(\dot{\boldsymbol{E}})$ is given by the average value of $\pi(\dot{\boldsymbol{\epsilon}}^*)$ over the spherical RVE volume.

$$\mathit{\Pi}(\dot{\boldsymbol{E}}) = \frac{1}{\bar{V}} \int_V \pi[\dot{\boldsymbol{\epsilon}}^*(\dot{\boldsymbol{E}})] dV \tag{5.38}$$

5.4 Deriving the effective yield surface

The definition of the macroscopic plastic dissipation potential in Eq. (5.38) then derives the macroscopic stress tensor $\boldsymbol{\Sigma}$ as follows.

$$\boldsymbol{\Sigma} = \frac{\partial \Pi}{\partial \dot{\boldsymbol{E}}} = \frac{1}{V}\int_V \frac{\partial \pi}{\partial \dot{\boldsymbol{E}}} dV = \frac{1}{V}\int_V \left[\frac{\partial \tilde{\pi}}{\partial \dot{\epsilon}^*_{eq}} : \left(\frac{\partial \dot{\epsilon}^*_{eq}}{\partial \dot{\boldsymbol{\epsilon}}^*} : \frac{\partial \dot{\boldsymbol{\epsilon}}^*}{\partial \dot{\boldsymbol{E}}}\right) G(\xi^*) + \tilde{\pi}(\dot{\boldsymbol{\epsilon}}^*) \frac{\partial G}{\partial \omega^*}\frac{\partial \omega^*}{\partial \xi^*}\left(\frac{\partial \xi^*}{\partial \dot{\boldsymbol{\epsilon}}^*} : \frac{\partial \dot{\boldsymbol{\epsilon}}^*}{\partial \dot{\boldsymbol{E}}}\right)\right] dV \tag{5.39}$$

where

$$\frac{\partial \dot{\epsilon}^*_{eq}}{\partial \dot{\boldsymbol{\epsilon}}^*} = \frac{2}{3}\frac{\partial \dot{\boldsymbol{\epsilon}}^*}{\partial \dot{\epsilon}^*_{eq}}, \tag{5.40}$$

$$\frac{\partial \tilde{\pi}}{\partial \dot{\epsilon}^*_{eq}} = \sigma_0, \tag{5.41}$$

$$\frac{\partial \omega^*}{\partial \xi^*} = \frac{[g(\xi^*)]^2 + [g'(\xi^*)]^2}{[g(\xi^*)]^2 + g(\xi^*)g''(\xi^*)}, \tag{5.42}$$

and

$$\frac{\partial \omega^*}{\partial \dot{\boldsymbol{\epsilon}}^*} = -\frac{4}{3}\frac{1}{\dot{\epsilon}^*_{eq}\sin 3\xi^*}\left[\left(\frac{\dot{\boldsymbol{\epsilon}}^*}{\dot{\epsilon}^*_{eq}}\right)^2 - \frac{1}{2}\mathbf{1} - \frac{1}{2}\cos 3\xi^*\left(\frac{\dot{\boldsymbol{\epsilon}}^*}{\dot{\epsilon}^*_{eq}}\right)\right]. \tag{5.43}$$

The derivative $\dfrac{\partial \dot{\boldsymbol{\epsilon}}^*}{\partial \dot{\boldsymbol{E}}}$ has a conceptual importance in Eq. (5.39), since it attaches an IPE variable ($\dot{\boldsymbol{\epsilon}}^*$) to the actual macroscopic strain rate $\dot{\boldsymbol{E}}$. The link between these two tensors can be successfully obtained by defining a macroscopic strain rate field $\dot{\boldsymbol{E}}^*$ related to a hypothetical IPE macroscopic material, given in Eq. (5.12), which then allows to write the derivative $\dfrac{\partial \dot{\boldsymbol{\epsilon}}^*}{\partial \dot{\boldsymbol{E}}}$ as

$$\frac{\partial \dot{\boldsymbol{\epsilon}}^*}{\partial \dot{\boldsymbol{E}}} = \frac{\partial \dot{\boldsymbol{\epsilon}}^*}{\partial \dot{\boldsymbol{E}}^*} : \frac{\partial \dot{\boldsymbol{E}}^*}{\partial \dot{\boldsymbol{E}}} = \mathbb{L}^+ + \frac{1}{3}\left(\frac{R}{r}\right)^3 \mathbf{1} \otimes \left[\mathbb{L}^+ : (\mathbf{1} - 3e_r \otimes e_r)\right]. \tag{5.44}$$

Three specific configurations of $\dot{\boldsymbol{E}}$ are considered to obtain important particularized expressions of $\boldsymbol{\Sigma}$. The first one corresponds to the case of deviatoric $\dot{\boldsymbol{E}}$ (i.e. $\dot{E}_m \to 0$). The second and third ones represent positive and negative hydrostatic $\dot{\boldsymbol{E}}$ (i.e. $\dot{E}_m \to \pm\infty$), respectively. The expressions of $\boldsymbol{\Sigma}$ for each of those situations are

$$\lim_{\dot{E}_m \to 0} \Sigma_m = 0, \tag{5.45}$$

$$\lim_{\dot{E}_m \to 0} \boldsymbol{\Sigma}' = \frac{2\sigma_0(1-f)}{3V}\mathbb{L}^+ : \left\{\boldsymbol{e}^{*'}G(\eta^*) - \frac{2G'(\eta^*)}{|\sin 3\eta^*|}\left[\left(\boldsymbol{e}^{*'}\right)^2 - \frac{1}{2}\mathbf{1} - \frac{1}{2}\cos 3\eta^* \boldsymbol{e}^{*'}\right]\right\}, \tag{5.46}$$

$$\lim_{\dot{E}_m \to \pm\infty} \Sigma_m = \pm \frac{\sigma_0}{3V} \int_V a^*_{eq} G(\xi^*_a) dV \quad \text{and} \tag{5.47}$$

$$\lim_{\dot{E}_m \to \pm\infty} \boldsymbol{\Sigma}' = \frac{2\sigma_0}{3V} \int_V \left\{ \pm \left(\frac{a^*}{a^*_{eq}} \right)^2 G(\xi^*_a) - 2 \frac{G'(\eta^*)}{|\sin 3\xi^*_a|} \left[\left(\frac{a^*}{a^*_{eq}} \right)^2 - \frac{1}{2}\mathbf{1} - \frac{1}{2} \cos 3\xi^*_a \left(\frac{a^*}{a^*_{eq}} \right) \right] \right\} dV, \tag{5.48}$$

where

$$\boldsymbol{a}^* = \mathbb{L}^+ : \left\{ \left(\frac{R}{r} \right)^3 \left[\mathbf{1} - 3\boldsymbol{e}_r(\varphi, \theta) \otimes \boldsymbol{e}_r(\varphi, \theta) \right] \right\}, \tag{5.49}$$

$$a^*_{eq} = \sqrt{\frac{2}{3} \boldsymbol{a}^* : \boldsymbol{a}^*} \tag{5.50}$$

and

$$\xi^*_a = \frac{1}{3} \arccos \left(\frac{4 \det \boldsymbol{a}^*}{(a^*_{eq})^3} \right). \tag{5.51}$$

The fact that both Eq. (5.45) and (5.46) do not involve any integral turns these expressions into a very convenient way for obtaining deviatoric curves on π-plane (i.e. $\{\boldsymbol{\Sigma} / \Sigma_m(\boldsymbol{\Sigma}) = 0\}$). Thus, these curves can be produced with a minimal computational cost, since $\lim_{\dot{E}_m \to 0} \boldsymbol{\Sigma}'$ is directly dependent only on the IPE macroscopic Lode angle $\eta^* \in [0, 2\pi]$ of the strain rate tensor $\dot{\boldsymbol{E}}$.

5.5 Results and discussion

In order to illustrate the ideas provided in the former subsections, macroscopic yield surfaces are obtained for four different microscopic material symmetries: Cubic (C), Transversely Isotropic (TI), Tetragonal (T) and Orthotropic (O). Each of these symmetries is related to specific dependency between coefficients in the tensor $\mathbb{L}$, represented in Voigt notation in Eq. (5.4). These restrictions are schematized in Fig. 27 and were adapted from Royer and Dieulesaint (2000a), Royer and Dieulesaint (2000b), Canova et al. (1985) and Cowin (2013) in order to respect Eq. (5.5) as well. The chosen coefficients of $\mathbb{L}$ for each of those symmetries (C, TI, T and O), additionally to the isotropic one (I), are summarized in Table 5. These coefficients were picked only for academic purposes. Additionally, Karafillis and Boyce (1993) proposed a experimental procedure to identify these coefficients only for a given continuum material. Thus, further work must be devoted in order to propose an experimental method to determine the coefficients of $\mathbb{L}$ for a porous ductile material.

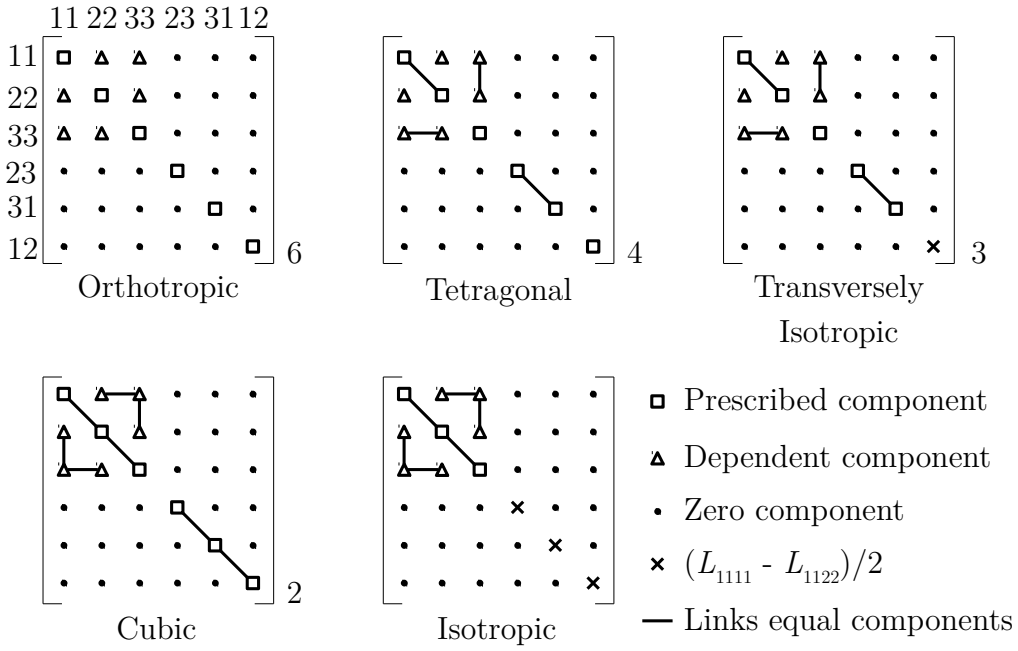

Figure 27: Anisotropy symmetries represented in the linear transformation L used in this section.

The five anisotropy symmetries used in this section are illustrated here (including isotropy) by general schemes of $\underline{\underline{\boldsymbol{L}}}$ on its irreducible forms. The squares represent components that must be prescribed in order to define the linear transformation $\underline{\underline{\boldsymbol{L}}}$. The triangles refer to components that are calculated by using the pressure independence condition described in Eq. (5.5). Every matrix depicted hereby is symmetric. The number of parameters required to define $\underline{\underline{\boldsymbol{L}}}$ for each symmetry is at the right-bottom corner of their respective matrices (except for isotropy, which requires only one parameter). Source: the author.

Table 5: Anisotropy coefficients of the linear transformation $\mathbb{L}$.

Symm.	L_{11}	L_{22}	L_{33}	L_{44}	L_{55}	L_{66}
I	1.0	1.0	1.0	0.75	0.75	0.75
C1	1.0	1.0	1.0	0.875	0.875	0.875
C2	1.0	1.0	1.0	1.0	1.0	1.0
TI1	1.0	1.0	1.2	0.875	0.875	0.7
TI2	1.0	1.2	1.0	0.875	0.7	0.875
TI3	1.2	1.0	1.0	0.7	0.875	0.875
T1	1.0	1.2	1.0	0.875	1.0	0.875
O1	1.0	1.35	1.5	0.875	1.0	0.75

Source: the author.

Every analysis thereafter represents an anisotropic porous material in a ductile fracture regime. Thus, a porosity $f = 1\%$ and a Hershey-Hosford shape parameter $m = 8$ are chosen to simulate this condition for an FCC material matrix. For sake of simplicity, the microscopic yield stress $\sigma_0 = 1$, which does not affect any of the further overall results nor conceptual discussions.

The coefficient C in Eq. (5.4) is chosen so that it satisfies $|| \left(\underline{\underline{\boldsymbol{L}}}^{+} \right) || = ||\underline{\underline{\boldsymbol{J}}}||$ for every considered symmetry. This assumption assures that none of the discrepancy between the isotropic reference (I) and the anisotropic yield surfaces is due to any uniform scale factor. Hence, only the relation between the L_{kk} coefficients, $k = 1, .., 6$, affects the anisotropic curves throughout this section.

Figures 28–31 present both (a) deviatoric and (b) meridional planes of macroscopic yield surfaces for the cubic (C1), transversely isotropic (TI3), tetragonal (T1) and orthotropic (O1) symmetries, respectively. The overall macroscopic behavior matches the microscopic symmetries prescribed for material matrices. For example, while the deviatoric planes shown in Fig. 28a for a cubic material matrix (C1) do not present any relative rotation when compared to the isotropic reference (I), Fig. 29a exhibits a significant one. This rotation effect is due to the difference between the coefficients L_{11}, L_{22} and L_{33}, which privileges the directions 11 and 22 with more rigidity (i.e. for a specific direction, the rigidity and the L_{kk} coefficients are inversely proportional to each other).

The influence of decreasing symmetry planes (i.e. the increasing anisotropy effect) can be noticed by the increasing discrepancy between meridional planes in Figures 28b, 29b, 30b and 31b. For instance, the effect of different coefficients in the linear operator $\mathbb{L}$ in Eq. (5.4) for the orthotropic material matrix (O1) induced the macroscopic yield surface to distinguish its meridional planes for different macroscopic stress Lode angles θ. In the context of the present work, this outcome can be seen as a secondary indicator of the number of symmetry planes for a certain anisotropic matrix.

The analytical predictions described for $\dot{E}_m \to \infty$ in Eq. (5.45) and (5.46) are compared to the numerical results in Figures 28a, 29a, 30a and 31a. They exactly match the deviatoric planes related to a level of $\Sigma_m^f = 0$, which indicates the consistency between the analytical formulation and the computational implementation.

In order to evaluate the influence of different intensities of coefficients for the same material symmetry, Fig. 32 shows the deviatoric planes for the almost hydrostatic level $\Sigma_m^f = 0.99$ related to two macroscopic yield symmetries obtained for two different cubic material matrices (C1 and C2). These results confirm the consistency of the present formulation by providing the same of number symmetry pattern in each curve. In addition, the more different coefficients of the linear operator $\mathbb{L}$ are from the isotropic coefficients, the more further away the anisotropic curves (C1 and C2) are from the isotropic reference.

Analogously, Fig. 33 exhibits macroscopic deviatoric planes for the level $\Sigma_m^f = 0.99$ related to three transversely isotropic material matrices (TI1, TI2, TI3). Because of the permutation of their anisotropy coefficients (see Table 5), TI1, TI2 and TI3 represent anisotropy frames that are orthogonal to each other. This orthogonality is corroborated by the matching of the curves TI1, TI2 and TI3 in specific points on the deviatoric plane. For example, the curves TI1 and TI2 coincide on the axis $\boldsymbol{\Sigma}_1'$, which is referred to the direction

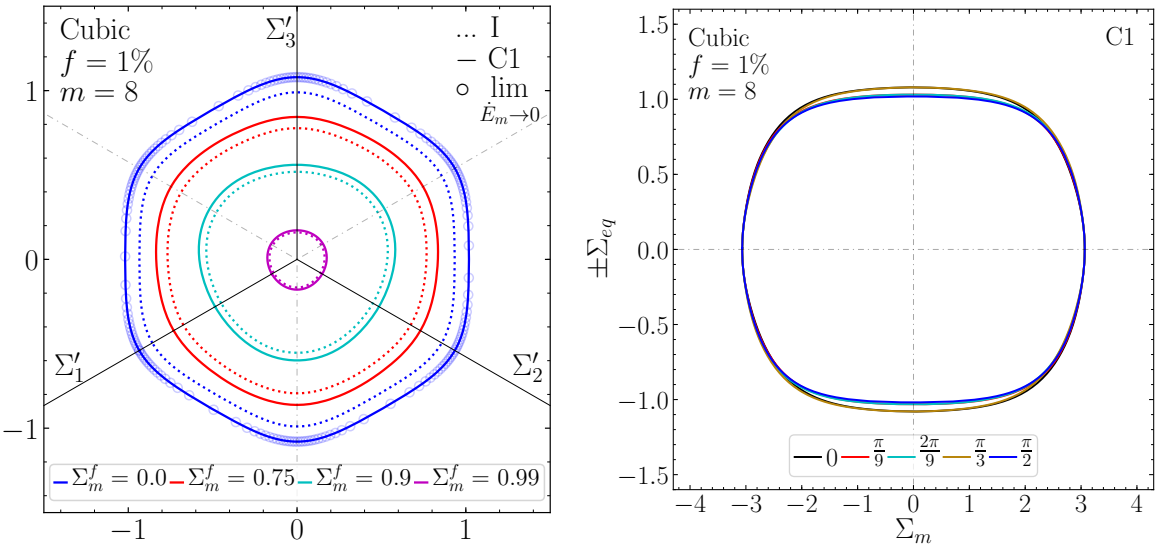

(a) deviatoric planes (b) meridional planes

Figure 28: Macroscopic yield surface for a cubic material with porosity $f = 1\%$ and shape parameter $m = 8$.

Contour plots for different levels of (a) $\Sigma^f_m = \Sigma_m/|\Sigma_m|_{max}$; and (b) macroscopic stress Lode angle θ ($\Sigma_{eq} \geq 0$) and $\theta + \pi$ ($\Sigma_{eq} < 0$). The circles comprise points obtained through Eq. (5.45) and (5.46). In both curves, one assumes $\sigma_0 = 1$ for the sake of simplicity. Source: the author.

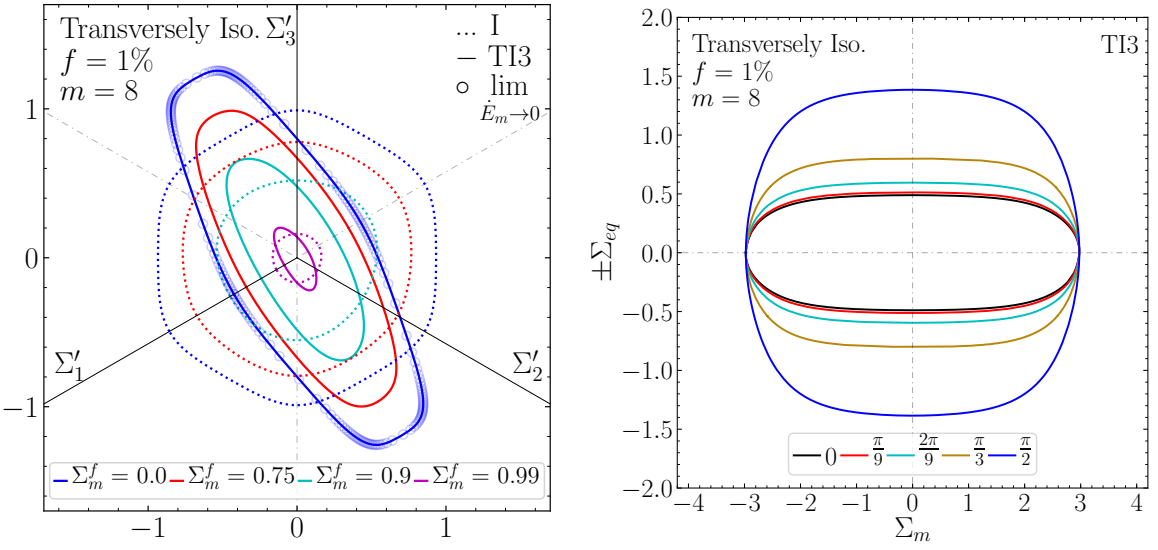

(a) deviatoric planes (b) meridional planes

Figure 29: Macroscopic yield surface for a transversely isotropic material with porosity $f = 1\%$ and shape parameter $m = 8$.

Contour plots for different levels of (a) $\Sigma^f_m = \Sigma_m/|\Sigma_m|_{max}$; and (b) macroscopic stress Lode angle θ ($\Sigma_{eq} \geq 0$) and $\theta + \pi$ ($\Sigma_{eq} < 0$). The circles comprise points obtained through Eq. (5.45) and (5.46). In both curves, one assumes $\sigma_0 = 1$ for the sake of simplicity Source: the author.

where the anisotropic coefficients L_{11} of these materials are the same. The observation of these aspects illustrates the robustness – in the sense of successful applications for a wide

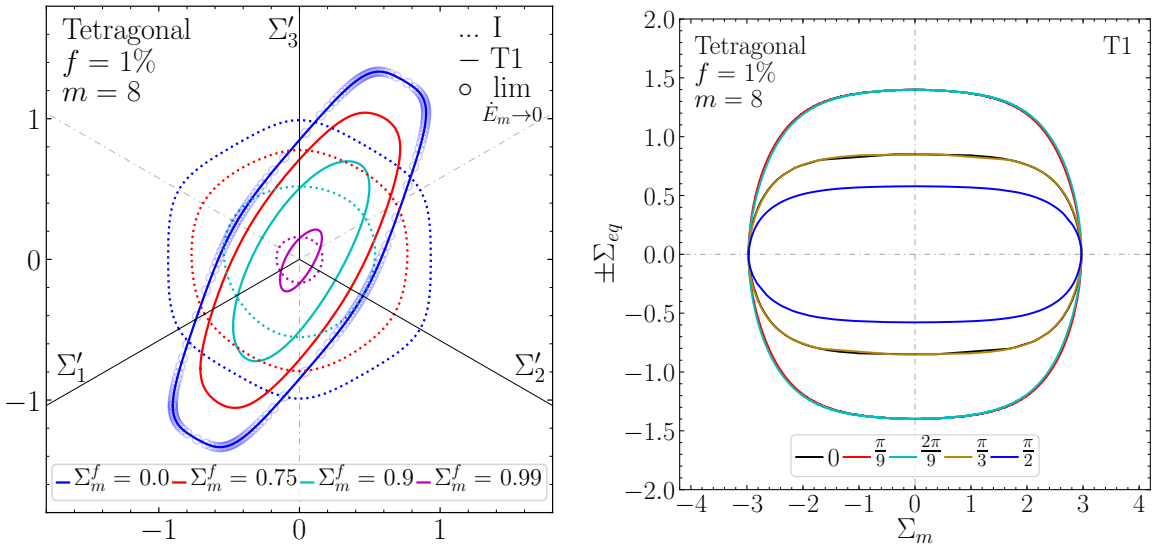

(a) deviatoric planes (b) meridional planes

Figure 30: Macroscopic yield surface for a tetragonal material with porosity $f = 1\%$ and shape parameter $m = 8$.

Contour plots for different levels of (a) $\Sigma^f_m = \Sigma_m/|\Sigma_m|_{max}$; and (b) macroscopic stress Lode angle θ ($\Sigma_{eq} \geq 0$) and $\theta + \pi$ ($\Sigma_{eq} < 0$). The circles comprise points obtained through Eq. (5.45) and (5.46). In both curves, one assumes $\sigma_0 = 1$ for the sake of simplicity Source: the author.

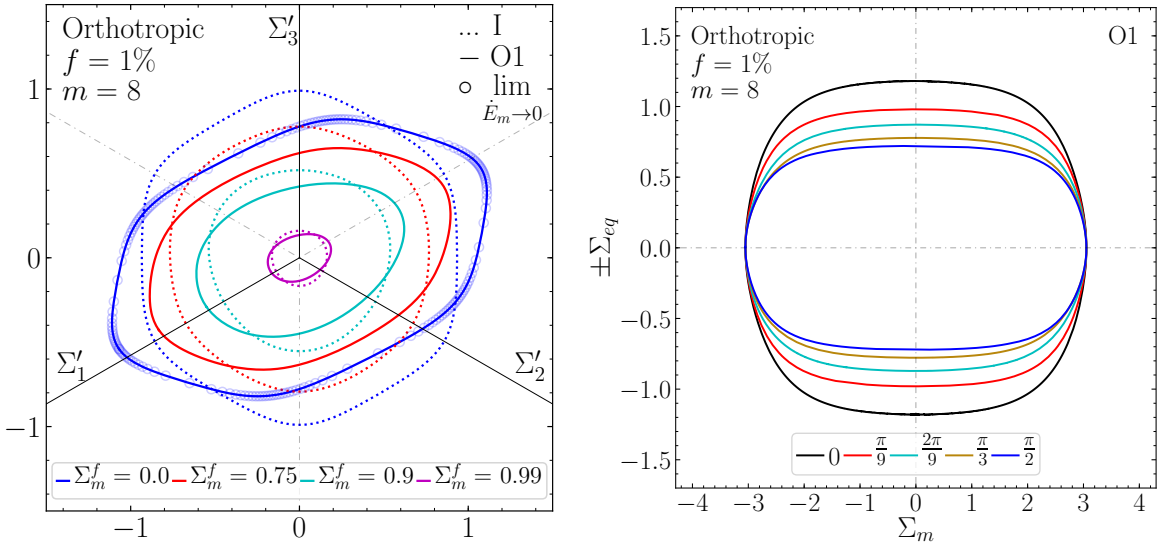

(a) deviatoric planes (b) meridional planes

Figure 31: Macroscopic yield surface for a orthotropic material with porosity $f = 1\%$ and shape parameter $m = 8$.

Contour plots for different levels of (a) $\Sigma^f_m = \Sigma_m/|\Sigma_m|_{max}$; and (b) macroscopic stress Lode angle θ ($\Sigma_{eq} \geq 0$) and $\theta + \pi$ ($\Sigma_{eq} < 0$). The circles comrpise points obtained through Eq. (5.45) and (5.46). In both curves, one assumes $\sigma_0 = 1$ for the sake of simplicity Source: the author.

range of parameters – and consistency of the present formulation even for high intensity effects of anisotropy.

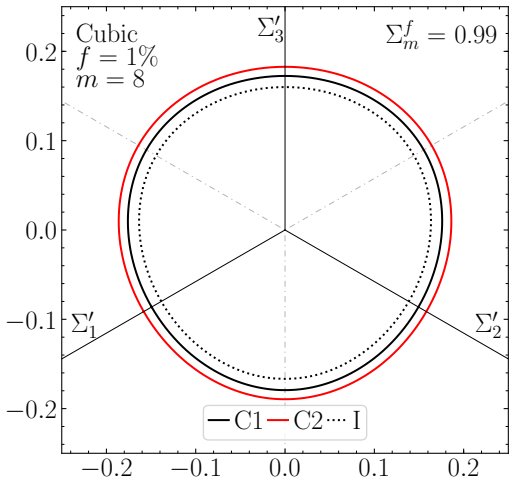

Figure 32: Macroscopic deviatoric planes for two different cubic materials (C1 and C2) with porosity $f = 1\%$ and shape parameter $m = 8$.

Contour plots for a level of $\Sigma^f_m = \Sigma_m/|\Sigma_m|_{max} = 0.99$. An isotropic reference is shown by a dotted line. Source: the author.

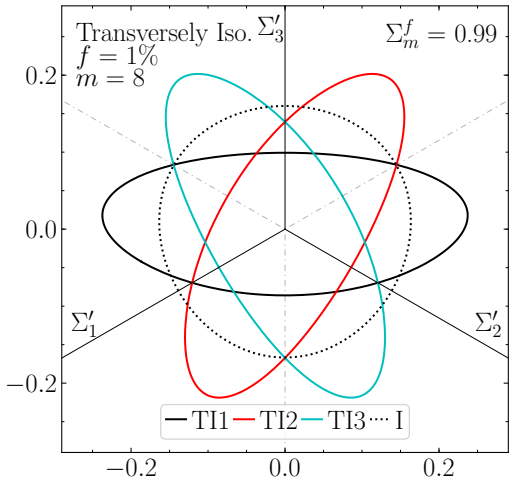

Figure 33: Macroscopic deviatoric planes for three different transversely isotropic materials (TI1, TI2 and TI3) with porosity $f = 1\%$ and shape parameter $m = 8$.

Contour plots for a level of $\Sigma^f_m = \Sigma_m/|\Sigma_m|_{max} = 0.99$. An isotropic reference is shown by a dotted line. Source: the author.

5.6 Concluding remarks

This chapter proposed a formulation to represent yield criteria for anisotropic porous media based on i) the concept of an IPE material introduced by Karafillis and Boyce (1993) to model anisotropy of continuum media and ii) the framework put forward by Gurson (1977) to model ductile porous materials.

The numerical results showed the consistency and robustness, in the sense of the applicability of the formulation for a wide range of conditions, of the formulation for four different symmetries. The results were limited to cases which there was coincidence between the principal directions of macroscopic strain rate and the anisotropic referential due to the extreme computational cost of performing 6-dimensional contour plots for visualizations. Nonetheless, the formulation itself considers arbitrary anisotropic symmetries and can be implemented in general multiscale FEM codes.

The results also revealed that the macroscopic yield criteria preserved the overall symmetries of the RVE material matrix. This fact is due to the spherical shape of the cavity inside the RVE. However, further works can properly combine the anisotropy provided by the material matrix with that acquired from the morphological effects.

The trial velocity field proposed by Gurson (1977) proved to be an adequate choice for the developments hereby. However, further works may also explore more elaborate trial fields in order to obtain better upper bounds to the RVE problem.

6 MODELING OF ORTHOTROPIC RUPTURE OF POROUS ALUMINUM ALLOYS

This chapter presents an approach for modeling anisotropic rupture of porous aluminum alloys. This approach consists of deriving the macroscopic yield surface of a Gurson-like RVE whose material matrix follows the Yld2004-18p yield criterion proposed by Barlat et al. (2005). The RVE is assumed to undergo uniform macroscopic strain rates and the correspondent dissipation potentials are obtained by using Gurson's trial microscopic velocity field as a first attempt, which composes an upper bound procedure. The results point out the consistency of including the porosity parameter on the modeling of rupture in orthotropic aluminum alloys, as well as the need to account for the porosity effect on the resultant macroscopic yield surfaces.

6.1 The Barlat et al. (2005) Yld2004-18p yield criterion

Although Karafillis and Boyce (1993) have formulated a convenient way to represent anisotropic yield surfaces by the concept of IPE material, their approach did not match experimental results of aluminum sheet forming Barlat et al. (2003). In order to overcome this drawback, Barlat et al. (2003) proposed an anisotropic yield function by applying two linear different transformations over a sum of two distinct yield functions. This method doubled the number of material parameters to be experimentally identified, which thus increased the accuracy in representing aluminum alloys. Banabic et al. (2005) also proposed anisotropic yield function based on an extension of Barlat and Lian (1989) model in order to include more material parameters. However, these approaches were restricted to plane stress formulation.

Barlat et al. (2005) then suggested a consistent manner to derive an anisotropic yield surface with more material parameters than Karafillis and Boyce (1993), also based on linear transformations (Eq. (6.2)), which is thus applicable to 3D full stress states. Their framework uses an arbitrary number of linear transformations instead of only one as in Karafillis and Boyce (1993). However, the more linear transformations are considered, the more material coefficients need to be experimentally identified.

Although their formulation is consistent with an arbitrary number of linear transformations, Barlat et al. (2005) restricts their results and formulae to only two. These linear transformations are then applied to the Cauchy stress tensor $\boldsymbol{\sigma}$, defining two auxiliary traceless stress tensors $\boldsymbol{s}^1$ and $\boldsymbol{s}^2$.The linearly transformed stress tensors $\boldsymbol{s}^1$ and $\boldsymbol{s}^2$ are

defined in its full tensor form as the following:

$$\begin{aligned} \boldsymbol{s}^1 &= \left(\mathbb{C}^1 : \mathbb{J}\right) : \boldsymbol{\sigma} = \mathbb{L}^1 : \boldsymbol{\sigma} \\ \boldsymbol{s}^2 &= \left(\mathbb{C}^2 : \mathbb{J}\right) : \boldsymbol{\sigma} = \mathbb{L}^2 : \boldsymbol{\sigma}. \end{aligned} \tag{6.1}$$

where

$$\underline{\underline{\boldsymbol{C}}}^i = \begin{bmatrix} 0 & -c^i_{12} & -c^i_{13} & 0 & 0 & 0 \\ -c^i_{21} & 0 & -c^i_{23} & 0 & 0 & 0 \\ -c^i_{31} & -c^i_{32} & 0 & 0 & 0 & 0 \\ 0 & 0 & 0 & c^i_{44} & 0 & 0 \\ 0 & 0 & 0 & 0 & c^i_{55} & 0 \\ 0 & 0 & 0 & 0 & 0 & c^i_{66} \end{bmatrix} \tag{6.2}$$

$$\underline{\underline{\boldsymbol{L}}}^i = \underline{\underline{\boldsymbol{C}}}^i \underline{\underline{\boldsymbol{J}}} = \frac{1}{3} \begin{bmatrix} b^i_2 + b^i_3 & -c^i_3 & -b^i_2 & 0 & 0 & 0 \\ -b^i_3 & b^i_3 + b^i_1 & -b^i_1 & 0 & 0 & 0 \\ -b^i_2 & -b^i_1 & b^i_1 + b^i_2 & 0 & 0 & 0 \\ 0 & 0 & 0 & 3b^i_4 & 0 & 0 \\ 0 & 0 & 0 & 0 & 3b^i_5 & 0 \\ 0 & 0 & 0 & 0 & 0 & 3b^i_6 \end{bmatrix},$$

$$\begin{aligned} b^i_1 &= (4c^i_{23} + c^i_{31} - 2c^i_{12})/3, \\ b^i_2 &= (4c^i_{31} + c^i_{12} - 2c^i_{23})/3, \\ b^i_3 &= (4c^i_{12} + c^i_{23} - 2c^i_{31})/3, \\ b^i_4 &= c^i_{44}, \\ b^i_5 &= c^i_{55} \text{ and} \\ b^i_6 &= c^i_{66} \end{aligned}$$

and $\underline{\underline{\boldsymbol{C}}}^i$, $\underline{\underline{\boldsymbol{L}}}^i$ and $\underline{\underline{\boldsymbol{J}}}$ correspond to the Voigt notation matrices(see Appendix A) to the 4th-order tensors $\mathbb{C}^i$, $\mathbb{L}^i$ and $\mathbb{J}$, respectively, with $\mathbb{J}$ given by Eq. (4.19). The superscript i in Eq. (6.2) refers to the i-th linear transformation, $i = 1, 2$.

In accordance with their approach, an anisotropic yield criterion was derived by writing an isotropic convex function in terms of the transformed stress tensors $\boldsymbol{s}^1$ and $\boldsymbol{s}^2$. According to Eggleston (1958), a convexity of a function is preserved if its arguments are transformed by affine operators. This guarantees the convexity of the resultant yield function $\phi\left(\boldsymbol{s}^1, \boldsymbol{s}^2\right)$, Eq. (6.3). Because two linear transformations are involved, this approach can give rise to criteria that can take into account up to 18 parameters of anisotropy.

$$\phi(\boldsymbol{\sigma}) = \phi(\boldsymbol{s}^1, \boldsymbol{s}^2) = \phi(S^1_1, S^1_2, S^1_3, S^2_1, S^2_2, S^2_3), \tag{6.3}$$

where S_j^i represents the j-th principal component of $\boldsymbol{s}^i$, $j \in (1,2,3)$.

Based on the transformations defined in Eq. (6.3), Barlat et al. (2005) put forward two yield functions: Yld2004-18p (18 parameters), Eq. (6.4), and Yld2004-13p (13 parameters). Since Yld2004-13p is a modification of Yld2004-18p to decrease the number of material parameters to identify experimentally, the present work explores only Yld2004-18p in the following sections.

$$\begin{aligned}\phi(S_1^1, S_2^1, S_3^1, S_1^2, S_2^2, S_3^2) = \Bigg[\frac{1}{4}\Big(&|S_1^1 - S_1^2|^m + |S_1^1 - S_2^2|^m + |S_1^1 - S_3^2|^m + \\ &|S_2^1 - S_1^2|^m + |S_2^1 - S_2^2|^m + |S_2^1 - S_3^2|^m + \\ &|S_3^1 - S_1^2|^m + |S_3^1 - S_2^2|^m + |S_3^1 - S_3^2|^m\Big)\Bigg]^{1/m} = \sigma_0\end{aligned} \tag{6.4}$$

A minimization of an error function in terms of both predicted and experimental data – indicated by the lower scripts *pr* and *ex* in Eq. (6.5) below – permits to obtain the parameters c_{ij}^1 and c_{ij}^2 for a given material, as shown in Eq. (6.5). They applied this framework to identify the yield function coefficients of two aluminum alloys: a mildly anisotropic, 6111-T4, and a more anisotropic one, 2090-T3, whose parameters are presented in Table 6.

$$err(c_{ij}^1, c_{ij}^2) = \sum_p z_p \left(\frac{\sigma_p^{pr}}{\sigma_p^{ex}} - 1\right)^2 + \sum_q z_q \left(\frac{d_q^{pr}}{d_q^{ex}} - 1\right)^2, \tag{6.5}$$

where p and q denote the number of available experimental results of yield stress, the superscripts indicate whether the value is predicted or experimental, d is the Lankford coefficient, i.e. the ratio between width and thickness true plastic strain of a specimen under uniaxial tensile test and z are special weight values proposed in their work.

Table 6: Yld2004-18p coefficients for 6111-T4 and 2090-T3 aluminium alloys ($m = 8$)

	6111-T4	2090-T3		6111-T4	2090-T3
c_{12}^1	1.241024	-0.069888	c_{12}^2	0.775366	0.981171
c_{13}^1	1.078271	0.936408	c_{13}^2	0.922743	0.476741
c_{21}^1	1.216463	0.079143	c_{21}^2	0.765487	0.575316
c_{23}^1	1.223867	1.003060	c_{23}^2	0.793356	0.866827
c_{31}^1	1.093105	0.524741	c_{31}^2	0.918689	1.145010
c_{32}^1	0.889161	1.363180	c_{32}^2	1.027625	-0.079294
c_{44}^1	0.501909	1.023770	c_{44}^2	1.115833	1.051660
c_{55}^1	0.557173	1.069060	c_{55}^2	1.112273	1.147100
c_{66}^1	1.349094	0.954322	c_{66}^2	0.589787	1.404620

Source: (BARLAT et al., 2005)

6.2 A Gurson-like RVE for modeling porous aluminum alloys

In the same sense of the approach in the last chapter, a modification of the Gurson's RVE is hereby proposed in order to consider the anisotropic behavior of the material matrix, as shown in Fig. 34. The microscopic yield criterion of the material portion Ω surrounding the void is then assumed to behave as the Yld2004-18p criterion proposed by Barlat et al. (2005). Although different void morphologies could be also explored within the following formulation, the present work is restricted to centered spherical cavities so that whatever anisotropic effect is due to the material matrix yield criterion.

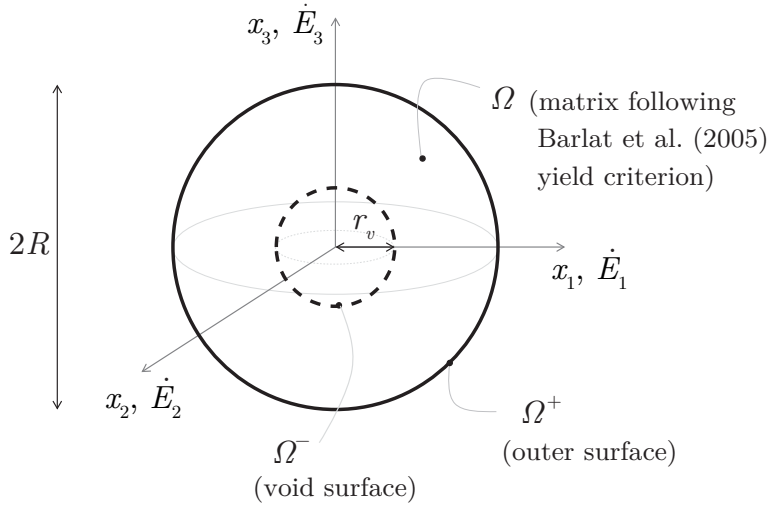

Figure 34: The chosen Gurson-like RVE for modeling porous aluminum alloys.

The material matrix in Ω is assumed to follow the Barlat et al. (2005) anisotropic yield criterion. Source: the author.

In accordance with chapters 3, 4 and 5, the trial strain rate field $\dot{\boldsymbol{\epsilon}}_G$ proposed by Gurson (1977) is still chosen as an approximation to the analytically exact $\dot{\boldsymbol{\epsilon}}$ strain rate field. This approach consists of an upper bound solution to the BVP posed by the hollow spherical RVE, subjected to a macroscopic strain field $\dot{\boldsymbol{E}}$ on $\partial\Omega^+$, whose material matrix follows an incompressible rigid-perfect plasticity model (i.e. Yld2004-18p, normality rule and no hardening). Nonetheless, it is important to remark that more refined trial strain rate fields will be considered in future work. As already commented in chapter 4 and chapter 5, the fields provided by Monchiet and Kondo (2012) and by Li, Sauer and Wang (2007) are believed to result in better upper bound estimates.

6.3 Deduction of the macroscopic dissipation potential

The microscopic plastic dissipation potential π associated to a point in RVE domain Ω whose plastic laws satisfy Eq. (5.7) is defined in Eq. (5.17). It can be defined as a function of the traceless (i.e. $\mathrm{Tr}\,\dot{\boldsymbol{\epsilon}} = 0$) microscopic strain rate field $\dot{\boldsymbol{\epsilon}}$ as

$$\pi(\dot{\boldsymbol{\epsilon}}) = \sup_{\sigma \in \Upsilon} \{\boldsymbol{\sigma} : \dot{\boldsymbol{\epsilon}}\} \tag{6.6}$$

where $\Upsilon = \{\boldsymbol{\sigma} | \psi(\boldsymbol{\sigma}) = \phi(\boldsymbol{s}^1, \boldsymbol{s}^2) \leq \sigma_0\}$ is a convex set of stress tensors $\boldsymbol{\sigma}$.

Taking into account the normality rule for the flow of the microscopic plastic strain rate $\dot{\boldsymbol{\epsilon}} = \dot{\lambda}\partial\psi/\partial\boldsymbol{\sigma}$ and recalling that the yield function $\psi(\boldsymbol{\sigma})$ is a homogeneous function of degree one, Eq. (5.18) is hereby reproduced for the sake of completeness:

$$\pi(\dot{\boldsymbol{\epsilon}}) = \boldsymbol{\sigma} : \left(\dot{\lambda}\frac{\partial\psi}{\partial\boldsymbol{\sigma}}\right) = \dot{\lambda}\boldsymbol{\sigma} : \frac{\partial\psi}{\partial\boldsymbol{\sigma}} = \dot{\lambda}\psi(\boldsymbol{\sigma}) = \dot{\lambda}\sigma_0. \tag{6.7}$$

Two auxiliary IPE strain rate fields $\dot{\boldsymbol{\epsilon}}^1$ and $\dot{\boldsymbol{\epsilon}}^2$ can be conveniently defined by expanding the normality flow rule $\dot{\boldsymbol{\epsilon}} = \dot{\lambda}\dfrac{\partial\psi}{\partial\boldsymbol{\sigma}}$ as

$$\begin{aligned}
\dot{\boldsymbol{\epsilon}} = \dot{\lambda}\frac{\partial\psi}{\partial\boldsymbol{\sigma}} &= \dot{\lambda}\left(\frac{\partial\psi}{\partial\boldsymbol{s}^1} : \frac{\partial\boldsymbol{s}^1}{\partial\boldsymbol{\sigma}} + \frac{\partial\psi}{\partial\boldsymbol{s}^2} : \frac{\partial\boldsymbol{s}^2}{\partial\boldsymbol{\sigma}}\right) \\
&= \dot{\lambda}\left(\frac{\partial\phi}{\partial\boldsymbol{s}^1} : \mathbb{L}^1 + \frac{\partial\phi}{\partial\boldsymbol{s}^2} : \mathbb{L}^2\right) \\
&= \left\{ \begin{array}{cc} \dot{\lambda}\dfrac{\partial\phi}{\partial\boldsymbol{s}^1} & \dot{\lambda}\dfrac{\partial\phi}{\partial\boldsymbol{s}^2} \end{array} \right\} : \left\{ \begin{array}{c} \mathbb{L}^1 \\ \mathbb{L}^2 \end{array} \right\} \\
&= \left\{ \begin{array}{cc} \dot{\boldsymbol{\epsilon}}^1 & \dot{\boldsymbol{\epsilon}}^2 \end{array} \right\} : \left\{ \begin{array}{c} \mathbb{L}^1 \\ \mathbb{L}^2 \end{array} \right\} \\
&= \left\{ \begin{array}{cc} \dot{\boldsymbol{\epsilon}}^1 & \dot{\boldsymbol{\epsilon}}^2 \end{array} \right\} : \mathbb{L}
\end{aligned} \tag{6.8}$$

Although the linear operator $\mathbb{L}$ is represented by a rectangular 12×6 matrix in Voigt notation (see Appendix A), the relation in Eq. (6.8) can be inverted by the Moore-Penrose generalized inversion procedure, which may generate infinite possible solutions to this problem. The choice of this inverse matrix for numerical implementation is discussed in section 6.5. By now, it is sufficient to assume that this inversion is possible and that it satisfies

$$\begin{aligned}
\dot{\boldsymbol{\epsilon}}^1 &= \dot{\lambda}\frac{\partial\phi}{\partial\boldsymbol{s}^1} = \dot{\boldsymbol{\epsilon}} : \left(\underline{\underline{\boldsymbol{L}}}^+\right)^1 \\
\dot{\boldsymbol{\epsilon}}^2 &= \dot{\lambda}\frac{\partial\phi}{\partial\boldsymbol{s}^2} = \dot{\boldsymbol{\epsilon}} : \left(\underline{\underline{\boldsymbol{L}}}^+\right)^2,
\end{aligned} \tag{6.9}$$

where $(\mathbb{L}^+)^1$ and $(\mathbb{L}^+)^2$ are represented by 6×6 matrix in Voigt notation.

The definition of the equivalent measures $\dot{\boldsymbol{\epsilon}}^1$ and $\dot{\boldsymbol{\epsilon}}^2$ conduces to a convenient expression of $\dot{\lambda}$, Eq. (6.10). Accordingly to the next subsections, this definition defines the microscopic plastic dissipation potential π as a function only of the microscopic strain rates $\dot{\boldsymbol{\epsilon}}^1$ and $\dot{\boldsymbol{\epsilon}}^2$.

$$\dot{\lambda} = \frac{\sqrt{(\dot{\epsilon}^1_{eq})^2 + (\dot{\epsilon}^2_{eq})^2}}{\sqrt{\frac{2}{3}\left(\frac{\partial \phi}{\partial \boldsymbol{s}^1} : \frac{\partial \phi}{\partial \boldsymbol{s}^1} + \frac{\partial \phi}{\partial \boldsymbol{s}^2} : \frac{\partial \phi}{\partial \boldsymbol{s}^2}\right)}}, \tag{6.10}$$

where

$$\dot{\epsilon}^1_{eq} = \sqrt{\frac{2}{3}\dot{\boldsymbol{\epsilon}}^1 : \dot{\boldsymbol{\epsilon}}^1} = \dot{\lambda}\sqrt{\frac{2}{3}\frac{\partial \phi}{\partial \boldsymbol{s}^1} : \frac{\partial \phi}{\partial \boldsymbol{s}^1}}$$
$$\dot{\epsilon}^2_{eq} = \sqrt{\frac{2}{3}\dot{\boldsymbol{\epsilon}}^2 : \dot{\boldsymbol{\epsilon}}^2} = \dot{\lambda}\sqrt{\frac{2}{3}\frac{\partial \phi}{\partial \boldsymbol{s}^2} : \frac{\partial \phi}{\partial \boldsymbol{s}^2}}.$$

Until this paragraph, the microscopic plastic dissipation potential cannot yet be described as a function solely on $\dot{\boldsymbol{\epsilon}}^1$ and $\dot{\boldsymbol{\epsilon}}^2$, once π also depends on the derivatives $\partial\phi/\partial\boldsymbol{s}^1$ and $\partial\phi/\partial\boldsymbol{s}^2$. The following subsections demonstrate that, in fact, Eq. (6.11) can be fully determined by prescribing only the microscopic strain rates, which is a condition for implementing the present criterion.

$$\pi = \sigma_0\dot{\lambda} = \frac{\sigma_0\sqrt{(\dot{\epsilon}^1_{eq})^2 + (\dot{\epsilon}^2_{eq})^2}}{\sqrt{\frac{2}{3}\left(\frac{\partial \phi}{\partial \boldsymbol{s}^1} : \frac{\partial \phi}{\partial \boldsymbol{s}^1} + \frac{\partial \phi}{\partial \boldsymbol{s}^2} : \frac{\partial \phi}{\partial \boldsymbol{s}^2}\right)}} \tag{6.11}$$

6.3.1 Eliminating the dependency of the microscopic plastic dissipation on the microscopic equivalent stresses

Accordingly to Eq. (6.5), the Yld2004-18p criterion expression can be written in concisely as:

$$\phi(\boldsymbol{s}^1, \boldsymbol{s}^2) = \phi(S^1_1, S^1_2, S^1_3, S^2_1, S^2_2, S^2_3) = \left[\frac{1}{4}\sum_{j=1}^{3}\sum_{i=1}^{3}|S^1_i - S^2_j|^m\right]^{1/m}. \tag{6.12}$$

The principal stress components S^1_i and S^2_j hold analogous definitions to those presented in chapter 5. Thus, their components are defined in terms of the von Mises stress and the Lode Angle related to the auxiliary stress state tensors $\boldsymbol{s}^1 = \mathbb{L}^1 : \boldsymbol{\sigma}$ and

$\boldsymbol{s}^2 = \mathbb{L}^2 : \boldsymbol{\sigma}$:

$$\begin{aligned} S_1^i &= \frac{2}{3} s_{eq}^i \cos(\omega_1^i) \\ S_2^i &= \frac{2}{3} s_{eq}^i \cos(\omega_2^i) \\ S_3^i &= \frac{2}{3} s_{eq}^i \cos(\omega_3^i), \end{aligned} \tag{6.13}$$

where

$$\begin{aligned} \omega_1^i &= \omega^i \\ \omega_2^i &= \omega^i - \frac{2\pi}{3} \\ \omega_3^i &= \omega^i + \frac{2\pi}{3} \\ \omega^i &= \frac{1}{3} \arccos\left(\frac{27}{2} \frac{\det \boldsymbol{s}^i}{(s_{eq}^i)^3} \right) \\ s_{eq}^i &= \sqrt{\frac{3}{2} \boldsymbol{s}^i : \boldsymbol{s}^i}, \end{aligned}$$

for $i = 1, 2$.

By combining Eq. (6.12) with Eq. (6.13) and defining an auxiliary angle $\alpha = \arctan\left(s_{eq}^2 / s_{eq}^1\right)$, $\alpha \in (0, \pi/2)$, the yield criterion $\phi(\boldsymbol{s}^1, \boldsymbol{s}^2)$ is now expressed as a function of five arguments:

$$\begin{aligned} \phi(s_{eq}^1, s_{eq}^2, \omega^1, \omega^2, \alpha) &= \sqrt{(s_{eq}^1)^2 + (s_{eq}^2)^2} \left\{ \frac{2}{3} \left[\left(\frac{1}{4} \sum_{j=1}^{3} \sum_{i=1}^{3} |\cos\alpha \cos\omega_j^1 - \sin\alpha \cos\omega_k^2|^m \right) \right]^{1/m} \right\} \\ &= \tilde{s}_{eq}(s_{eq}^1, s_{eq}^2) g(\omega^1, \omega^2, \alpha), \end{aligned} \tag{6.14}$$

where

$$\begin{aligned} \tilde{s}_{eq}(s_{eq}^1, s_{eq}^2) &= \sqrt{(s_{eq}^1)^2 + (s_{eq}^2)^2} \\ g(\omega^1, \omega^2, \alpha) &= \frac{2}{3} \left[\left(\frac{1}{4} \sum_{j=1}^{3} \sum_{i=1}^{3} |\cos\alpha \cos\omega_i^1 - \sin\alpha \cos\omega_j^2|^m \right) \right]^{1/m} \end{aligned} \tag{6.15}$$

The yield function ϕ shows to be a function on five independent variables $(s_{eq}^1, s_{eq}^2, \omega^1, \omega^2, \alpha)$. It is convenient to deal with this formula as being a product of two independent functions: $\tilde{s}_{eq}(s_{eq}^1, s_{eq}^2)$ and $g(\omega^1, \omega^2, \alpha)$, as expressed in Eq. (6.15). Therefore, the derivative of the

yield function ϕ with respect to $\boldsymbol{s}^k$, $k = 1, 2$, can be deduced as shown below:

$$\begin{aligned}\frac{\partial \phi}{\partial \boldsymbol{s}^k} = &\left(\frac{\partial \tilde{s}_{eq}}{\partial s^1_{eq}}\frac{\partial s^1_{eq}}{\partial \boldsymbol{s}^k} + \frac{\partial \tilde{s}_{eq}}{\partial s^2_{eq}}\frac{\partial s^2_{eq}}{\partial \boldsymbol{s}^k}\right) g(\omega^1, \omega^2, \alpha) + \\ &\tilde{s}_{eq}(s^1_{eq}, s^2_{eq})\left(\frac{\partial g}{\partial \omega^1}\frac{\partial \omega^1}{\partial \boldsymbol{s}^k} + \frac{\partial g}{\partial \omega^2}\frac{\partial \omega^2}{\partial \boldsymbol{s}^k} + \frac{\partial g}{\partial \alpha}\frac{\partial \alpha}{\partial \boldsymbol{s}^k}\right).\end{aligned} \tag{6.16}$$

The complete expressions of the derivatives contained in Eq. (6.16) are detailed in Appendix C. After a full analytical simplification procedure, which is omitted here for the sake of clarity, the microscopic plastic dissipation potential π is written concisely as

$$\begin{aligned}\pi &= \frac{\sigma_0\sqrt{(\dot{\epsilon}^1_{eq})^2 + (\dot{\epsilon}^2_{eq})^2}}{\sqrt{g^2 + g_\alpha^2 + (g_1 \sec\alpha)^2 + (g_2 \csc\alpha)^2}} \\ &= \tilde{\pi}(\dot{\epsilon}^1_{eq}, \dot{\epsilon}^2_{eq}) G(\omega^1, \omega^2, \alpha),\end{aligned} \tag{6.17}$$

where

$$\tilde{\pi}(\dot{\epsilon}^1_{eq}, \dot{\epsilon}^2_{eq}) = \sigma_0\sqrt{(\dot{\epsilon}^1_{eq})^2 + (\dot{\epsilon}^2_{eq})^2} \tag{6.18}$$

$$G(\omega^1, \omega^2, \alpha) = \frac{1}{\sqrt{g^2 + g_\alpha^2 + (g_1 \sec\alpha)^2 + (g_2 \csc\alpha)^2}} \tag{6.19}$$

and $g_1 = \dfrac{\partial g}{\partial \omega^1}$, $g_2 = \dfrac{\partial g}{\partial \omega^2}$ and $g_\alpha = \dfrac{\partial g}{\partial \alpha}$.

Although the dependency of the microscopic dissipation potential π on the microscopic equivalent stresses s^1_{eq} and s^2_{eq} has been eliminated, Eq. (6.17) still hinges on three stress variables: the microscopic stress Lode angles ω^1 and ω^2 and the auxiliary stress angle α. The following subsection links these three stress variables with those analogous ones of strain rates $\dot{\boldsymbol{\epsilon}}^1$ and $\dot{\boldsymbol{\epsilon}}^2$.

6.3.2 Relations between the microscopic stress angles (ω^1, ω^2, α) and microscopic strain rate angles (ξ^1, ξ^2, β)

In a similar way to the definition of the strain Lode angles which has been used so far in the present work, Eq. (6.20) puts forward the definitions of the Lode angles ξ^1 and

ξ^2, as well as the auxiliary angle β.

$$\begin{aligned}\xi^1 &= \frac{1}{3}\arccos\left(\frac{4\det\dot{\boldsymbol{\epsilon}}^1}{(\dot{\epsilon}^1_{eq})^3}\right)\\ \xi^2 &= \frac{1}{3}\arccos\left(\frac{4\det\dot{\boldsymbol{\epsilon}}^2}{(\dot{\epsilon}^2_{eq})^3}\right)\\ \beta &= \arctan\left(\frac{\dot{\epsilon}^2_{eq}}{\dot{\epsilon}^1_{eq}}\right),\end{aligned} \tag{6.20}$$

where $\xi^1 \in [0, \pi/3]$, $\xi^2 \in [0, \pi/3]$ and $\beta \in (0, \pi/2)$.

By applying the normality rule (Eq. (6.42)) in Eq. (6.20), the resultant expressions of ξ^1, ξ^2, and β become

$$\begin{aligned}\xi^1 &= \frac{1}{3}\arccos\left(\frac{4\det\dfrac{\partial\phi}{\partial\boldsymbol{s}^1}}{\left(\dfrac{2}{3}\dfrac{\partial\phi}{\partial\boldsymbol{s}^1}:\dfrac{\partial\phi}{\partial\boldsymbol{s}^1}\right)^{3/2}}\right)\\ \xi^2 &= \frac{1}{3}\arccos\left(\frac{4\det\dfrac{\partial\phi}{\partial\boldsymbol{s}^2}}{\left(\dfrac{2}{3}\dfrac{\partial\phi}{\partial\boldsymbol{s}^2}:\dfrac{\partial\phi}{\partial\boldsymbol{s}^2}\right)^{3/2}}\right)\\ \beta &= \arctan\left(\frac{\sqrt{\dfrac{\partial\phi}{\partial\boldsymbol{s}^2}:\dfrac{\partial\phi}{\partial\boldsymbol{s}^2}}}{\sqrt{\dfrac{\partial\phi}{\partial\boldsymbol{s}^1}:\dfrac{\partial\phi}{\partial\boldsymbol{s}^1}}}\right).\end{aligned} \tag{6.21}$$

A full simplification of the Eq. (6.21) through the expressions of $\partial\phi/\partial\boldsymbol{s}^1$ and $\partial\phi/\partial\boldsymbol{s}^2$ given in Appendix C gives rise to the relation between the strain rate angles (ξ^1, ξ^2, β)

and stress angles $(\omega^1, \omega^2, \alpha)$ in Eq. (6.22).

$$\begin{aligned}
\xi^1 &= \omega^1 + \arctan\left(\frac{g_1}{\cos\alpha(g\cos\alpha - g_\alpha \sin\alpha)}\right) \\
\xi^2 &= \omega^2 + \arctan\left(\frac{g_2}{\sin\alpha(g\sin\alpha + g_\alpha \cos\alpha)}\right) \\
\beta &= \arctan\left(\sqrt{\frac{(g_2\csc\alpha)^2 + (g\sin\alpha + g_\alpha\cos\alpha)^2}{(g_1\sin\alpha)^2 + (g\cos\alpha - g_\alpha\sin\alpha)^2}}\right)
\end{aligned} \tag{6.22}$$

Although there is no explicit way to invert these relations in order to express the stress angles as functions of the strain rate angles, this can be accomplished numerically by a 4-dimensional interpolation technique (i.e. interpolation of functions whose domain is defined in a three-dimensional euclidian space). A procedure for interpolating a structured n-dimensional set of points is proposed in Appendix B and allows to approximate the relation between the stress angles $(\omega^1, \omega^2, \alpha)$ and strain rate angles (ξ^1, ξ^2, β):

$$\begin{aligned}
\omega^1 &\approx \omega^1(\xi^1, \xi^2, \beta) \\
\omega^2 &\approx \omega^2(\xi^1, \xi^2, \beta) \\
\alpha &\approx \alpha(\xi^1, \xi^2, \beta).
\end{aligned} \tag{6.23}$$

6.3.3 Defining a microscopic plastic dissipation potential dependent only on the microscopic strain rates

Once the dependency of the microscopic plastic dissipation potential π on the stress variables s^1_{eq} and s^2_{eq} has been eliminated and a numerical relation between the stress angles $(\omega^1, \omega^2, \alpha)$ and strain rate angles (ξ^1, ξ^2, β) has been presented in the last subsections, π can now be rewritten as a function solely on the strain rate variables, as shown in Eq. (6.24).

$$\pi(\dot\epsilon^1_{eq}, \dot\epsilon^2_{eq}, \xi^1, \xi^2, \beta) = \frac{\sigma_0\sqrt{(\dot\epsilon^1_{eq})^2 + (\dot\epsilon^2_{eq})^2}}{\sqrt{g^2 + g_\alpha^2 + (g_1\sec\alpha)^2 + (g_2\csc\alpha)^2}}, \tag{6.24}$$

where $g = g(\omega^1, \omega^2, \alpha)$, $g_1 = g_1(\omega^1, \omega^2, \alpha)$, $g_2 = g_2(\omega^1, \omega^2, \alpha)$, $g_\alpha = g_\alpha(\omega^1, \omega^2, \alpha)$. Besides, in accordance with Eq. (6.23), $\omega^1 \approx \omega^1(\xi^1, \xi^2, \beta)$, $\omega^2 \approx \omega^2(\xi^1, \xi^2, \beta)$ and $\alpha \approx \alpha(\xi^1, \xi^2, \beta)$.

Finally, $\pi(\dot{\epsilon}^1_{eq}, \dot{\epsilon}^2_{eq}, \xi^1, \xi^2, \beta)$ is rewritten in Eq. (6.25) in an alternative form as a product of two different functions $\tilde{\pi}(\dot{\epsilon}^1_{eq}, \dot{\epsilon}^2_{eq})$ and $G(\xi^1, \xi^2, \beta)$, which are defined in Eq. (6.26).

$$\pi(\dot{\epsilon}^1_{eq}, \dot{\epsilon}^2_{eq}, \xi^1, \xi^2, \beta) = \tilde{\pi}(\dot{\epsilon}^1_{eq}, \dot{\epsilon}^2_{eq}) G(\xi^1, \xi^2, \beta), \tag{6.25}$$

where

$$\begin{aligned} \tilde{\pi}(\dot{\epsilon}^1_{eq}, \dot{\epsilon}^2_{eq}) &= \sigma_0 \sqrt{(\dot{\epsilon}^1_{eq})^2 + (\dot{\epsilon}^2_{eq})^2} \\ G(\xi^1, \xi^2, \beta) &= \frac{1}{\sqrt{g^2 + g_\alpha^2 + (g_1 \sec\alpha)^2 + (g_2 \csc\alpha)^2}}. \end{aligned} \tag{6.26}$$

6.4 Deriving the macroscopic yield surface

The macroscopic plastic dissipation potential $\Pi(\dot{\boldsymbol{E}})$ is still defined as the average value of the microscopic one, $\pi(\dot{\epsilon}^1_{eq}, \dot{\epsilon}^2_{eq}, \xi^1, \xi^2, \beta)$ over the volume occupied by the RVE, as presented in the chapters 3, 4 and 5. However, the derivation of the macroscopic stress tensors now requires a more complex approach, since the microscopic plastic dissipation potential π is now dependent on five independent variables instead of only two, as within the formulation for a macroscopic yield criterion based on the model by Karafillis and Boyce (1993) for the material matrix (see Eq. (5.39)). Eq. (6.27) describes the general expression for deriving the macroscopic stress tensors $\boldsymbol{\Sigma}$ as a first derivative of $\Pi(\dot{\boldsymbol{E}})$ with respect to $\dot{\boldsymbol{E}}$.

$$\begin{aligned} \boldsymbol{\Sigma} = \frac{\partial \Pi}{\partial \dot{\boldsymbol{E}}} &= \frac{\partial}{\partial \dot{\boldsymbol{E}}} \left(\frac{1}{V} \int_V \tilde{\pi}(\dot{\epsilon}^1_{eq}, \dot{\epsilon}^2_{eq}) G(\xi^1, \xi^2, \beta) dV \right) \\ &= \frac{1}{V} \int_V \left(\frac{\partial \tilde{\pi}}{\partial \dot{\boldsymbol{E}}} G(\xi^1, \xi^2, \beta) + \tilde{\pi}(\dot{\epsilon}^1_{eq}, \dot{\epsilon}^2_{eq}) \frac{\partial G}{\partial \dot{\boldsymbol{E}}} \right) dV \end{aligned} \tag{6.27}$$

Equations (6.28) and (6.29) exhibit the general approach for evaluating the derivatives in Eq. (6.27). Due to the number of variables which $\tilde{\pi}$ and G are dependent on, their derivatives with respect to the macroscopic strain rate $\dot{\boldsymbol{E}}$ are described here in a adapted matrix notation. Each matrix or vector component shown below does not necessarily represent a scalar value: they might also symbolize either a second-order tensor or even a

fourth-order one.

$$\frac{\partial \tilde{\pi}}{\partial \dot{\boldsymbol{E}}} = \left\{ \begin{array}{cc} \dfrac{\partial \tilde{\pi}}{\partial \dot{\epsilon}^1_{eq}} & \dfrac{\partial \tilde{\pi}}{\partial \dot{\epsilon}^2_{eq}} \end{array} \right\} \left[\begin{array}{cc} \dfrac{\partial \dot{\epsilon}^1_{eq}}{\partial \dot{\boldsymbol{\epsilon}}^1} & \dfrac{\partial \dot{\epsilon}^1_{eq}}{\partial \dot{\boldsymbol{\epsilon}}^2} \\ \dfrac{\partial \dot{\epsilon}^2_{eq}}{\partial \dot{\boldsymbol{\epsilon}}^1} & \dfrac{\partial \dot{\epsilon}^2_{eq}}{\partial \dot{\boldsymbol{\epsilon}}^2} \end{array} \right] : \left\{ \begin{array}{c} \dfrac{\partial \dot{\boldsymbol{\epsilon}}^1}{\partial \dot{\boldsymbol{E}}} \\ \dfrac{\partial \dot{\boldsymbol{\epsilon}}^2}{\partial \dot{\boldsymbol{E}}} \end{array} \right\} \tag{6.28}$$

$$\frac{\partial G}{\partial \dot{\boldsymbol{E}}} = \left\{ \begin{array}{ccc} \dfrac{\partial G}{\partial \omega^1} & \dfrac{\partial G}{\partial \omega^2} & \dfrac{\partial G}{\partial \alpha} \end{array} \right\} \left[\begin{array}{ccc} \dfrac{\partial \omega^1}{\partial \xi^1} & \dfrac{\partial \omega^1}{\partial \xi^2} & \dfrac{\partial \omega^1}{\partial \beta} \\ \dfrac{\partial \omega^2}{\partial \xi^1} & \dfrac{\partial \omega^2}{\partial \xi^2} & \dfrac{\partial \omega^2}{\partial \beta} \\ \dfrac{\partial \alpha}{\partial \xi^1} & \dfrac{\partial \alpha}{\partial \xi^2} & \dfrac{\partial \alpha}{\partial \beta} \end{array} \right] \left[\begin{array}{cc} \dfrac{\partial \xi^1}{\partial \dot{\boldsymbol{\epsilon}}^1} & \dfrac{\partial \xi^1}{\partial \dot{\boldsymbol{\epsilon}}^2} \\ \dfrac{\partial \xi^2}{\partial \dot{\boldsymbol{\epsilon}}^1} & \dfrac{\partial \xi^2}{\partial \dot{\boldsymbol{\epsilon}}^2} \\ \dfrac{\partial \beta}{\partial \dot{\boldsymbol{\epsilon}}^1} & \dfrac{\partial \beta}{\partial \dot{\boldsymbol{\epsilon}}^2} \end{array} \right] : \left\{ \begin{array}{c} \dfrac{\partial \dot{\boldsymbol{\epsilon}}^1}{\partial \dot{\boldsymbol{E}}} \\ \dfrac{\partial \dot{\boldsymbol{\epsilon}}^2}{\partial \dot{\boldsymbol{E}}} \end{array} \right\} \tag{6.29}$$

The derivatives in Eq. (6.28) and (6.29) are listed in section C.2 and section C.3, respectively.

6.5 Some details on the operations involving the rectangular linear operator L

According to the normality flow rule, the microscopic strain rate tensor $\dot{\boldsymbol{\epsilon}}$ can be written as

$$\begin{aligned} \dot{\boldsymbol{\epsilon}} &= \lambda \frac{\partial \phi}{\partial \boldsymbol{\sigma}} = \lambda \frac{\partial \phi}{\partial \boldsymbol{s}^1} : \frac{\partial \boldsymbol{s}^1}{\partial \boldsymbol{\sigma}} + \lambda \frac{\partial \phi}{\partial \boldsymbol{s}^1} : \frac{\partial \boldsymbol{s}^1}{\partial \boldsymbol{\sigma}} \\ &= \dot{\boldsymbol{\epsilon}}^1 : \mathbb{L}^2 + \dot{\boldsymbol{\epsilon}}^2 : \mathbb{L}^2. \end{aligned} \tag{6.30}$$

Equation (6.30) is equivalently rewritten following Voigt notations (see Appendix A) in Eq. (6.31) by taking into account both minor and major symmetries ($L_{ijkl} = L_{klij}$ and $L_{ijkl} = L_{jilk}$, respectively):

$$\underline{\dot{\boldsymbol{\epsilon}}} = \left[\begin{array}{cc} \underline{\underline{\boldsymbol{L}}}^1 & \underline{\underline{\boldsymbol{L}}}^2 \end{array} \right] \left\{ \begin{array}{c} \underline{\dot{\boldsymbol{\epsilon}}}^1 \\ \underline{\dot{\boldsymbol{\epsilon}}}^2 \end{array} \right\} = \underline{\underline{\boldsymbol{L}}} \left\{ \begin{array}{c} \underline{\dot{\boldsymbol{\epsilon}}}^1 \\ \underline{\dot{\boldsymbol{\epsilon}}}^2 \end{array} \right\}. \tag{6.31}$$

At this point, it is convenient to rewrite Eq. (6.17) as

$$\pi(\dot{\boldsymbol{\epsilon}}^1, \dot{\boldsymbol{\epsilon}}^2) = \sigma_0 \frac{\sqrt{\dfrac{2}{3}} \left\| \left\{ \begin{array}{c} \underline{\dot{\boldsymbol{\epsilon}}}^1 \\ \underline{\dot{\boldsymbol{\epsilon}}}^2 \end{array} \right\} \right\|}{\sqrt{g^2 + g_\alpha^2 + (g_1 \sec \alpha)^2 + (g_2 \csc \alpha)^2}}, \tag{6.32}$$

where $\dot{\epsilon}^1_{eq} = \sqrt{\frac{2}{3}}||\dot{\boldsymbol{\epsilon}}^1||$ and $\dot{\epsilon}^2_{eq} = \sqrt{\frac{2}{3}}||\dot{\boldsymbol{\epsilon}}^2||$.

Since the macroscopic plastic dissipation potential Π gives better upper bound estimates for lower values of dissipation (according to the kinematic theorem of Limit Analysis), the choice of the inverse of the matrix $\underline{\underline{\boldsymbol{L}}}$ is made by keeping this fact in mind. Thus, the problem of finding a proper inverse of $\underline{\underline{\boldsymbol{L}}}$ can be defined as a minimization of an auxiliary function

$$\mathcal{F} = \left\| \underline{\underline{\boldsymbol{L}}} \left\{ \begin{array}{c} \underline{\dot{\boldsymbol{\epsilon}}}^1 \\ \underline{\dot{\boldsymbol{\epsilon}}}^2 \end{array} \right\} - \dot{\boldsymbol{\epsilon}} \right\|^2 + \kappa^2 \left\| \left\{ \begin{array}{c} \underline{\dot{\boldsymbol{\epsilon}}}^1 \\ \underline{\dot{\boldsymbol{\epsilon}}}^2 \end{array} \right\} \right\|^2, \tag{6.33}$$

where $\kappa \in \mathbb{R}|\beta > 0$.

According to Ben-Israel and Greville (2003), the function $\mathcal{F}$ is minimized uniquely by

$$\left\{ \begin{array}{c} \underline{\dot{\boldsymbol{\epsilon}}}^1 \\ \underline{\dot{\boldsymbol{\epsilon}}}^2 \end{array} \right\} = (\underline{\underline{\boldsymbol{L}}}^a \underline{\underline{\boldsymbol{L}}} + \kappa^2 \underline{\underline{\boldsymbol{I}}})^{-1} \underline{\underline{\boldsymbol{L}}}^a \dot{\boldsymbol{\epsilon}}, \tag{6.34}$$

where $\underline{\underline{\boldsymbol{L}}}^a$ is the conjugate transpose matrix of $\underline{\underline{\boldsymbol{L}}}$ and $||\{\dot{\boldsymbol{\epsilon}}^1 \;\; \dot{\boldsymbol{\epsilon}}^2\}^T||$ *monotonically decreases with decreasing* κ.

Following Ben-Israel and Greville (2003),

$$\lim_{\kappa \to 0} (\underline{\underline{\boldsymbol{L}}}^a \underline{\underline{\boldsymbol{L}}} + \kappa^2 \underline{\underline{\boldsymbol{I}}})^{-1} \underline{\underline{\boldsymbol{L}}}^a = \underline{\underline{\boldsymbol{L}}}^+, \tag{6.35}$$

where $\underline{\underline{\boldsymbol{L}}}^+ \in \mathbb{M}(n,m)$ is the Moore-Penrose unique inverse of the matrix $\underline{\underline{\boldsymbol{L}}} \in \mathbb{M}(m,n)$ that respects the following properties defined by Penrose and Todd (1956):

$$\underline{\underline{\boldsymbol{L}}} \; \underline{\underline{\boldsymbol{L}}}^+ \; \underline{\underline{\boldsymbol{L}}} = \underline{\underline{\boldsymbol{L}}}, \tag{6.36}$$

$$\underline{\underline{\boldsymbol{L}}}^+ \; \underline{\underline{\boldsymbol{L}}}^+ \; \underline{\underline{\boldsymbol{L}}}^+ = \underline{\underline{\boldsymbol{L}}}^+, \tag{6.37}$$

$$(\underline{\underline{\boldsymbol{L}}} \; \underline{\underline{\boldsymbol{L}}}^+)^a = \underline{\underline{\boldsymbol{L}}} \; \underline{\underline{\boldsymbol{L}}}^+, \qquad \text{and} \tag{6.38}$$

$$(\underline{\underline{\boldsymbol{L}}}^+ \; \underline{\underline{\boldsymbol{L}}})^a = \underline{\underline{\boldsymbol{L}}}^+ \; \underline{\underline{\boldsymbol{L}}}. \tag{6.39}$$

The Moore-Penrose inverse $\underline{\underline{\boldsymbol{L}}}^+$ can be obtained by the Single Value Decomposition (SVD) procedure – among others (see Ben-Israel and Greville (2003) and Campbell and Meyer (2009)) – by decomposing the original matrix $\underline{\underline{\boldsymbol{L}}}$ as

$$\underline{\underline{\boldsymbol{L}}} = \underline{\underline{\boldsymbol{U}}} \; \underline{\underline{\boldsymbol{L}}}_{\mathcal{S}} \; \underline{\underline{\boldsymbol{V}}}^*, \tag{6.40}$$

where $\underline{\underline{\boldsymbol{U}}}$ is a $m \times m$ unitary matrix, $\underline{\underline{\boldsymbol{L}}}$ is a $m \times n$ matrix, $\underline{\underline{\boldsymbol{V}}}^*$ is a $n \times n$ unitary matrix, $\underline{\underline{\boldsymbol{L}}}_{\mathcal{S}}$ is a matrix whose diagonal components are nonnegative, while its other components are zero, and

$$\underline{\underline{\boldsymbol{L}}}^+ = \underline{\underline{\boldsymbol{U}}}\ \underline{\underline{\boldsymbol{L}}}^+_{\mathcal{S}}\ \underline{\underline{\boldsymbol{V}}}^*, \tag{6.41}$$

where $\underline{\underline{\boldsymbol{L}}}^+_{\mathcal{S}}$ is obtained by replacing each nonzero diagonal component of $\underline{\underline{\boldsymbol{L}}}_{\mathcal{S}}$ by its correspondent reciprocal value. Additionally, in the particular case of the present chapter, $m = 12$ and $n = 6$.

Accordingly, the relation in Eq. (6.31) can be thus inverted as in Eq. (6.42) so that the norm $||\{\dot{\boldsymbol{\epsilon}}^1 \ \ \dot{\boldsymbol{\epsilon}}^2\}||^T$ is minimized:

$$\left\{ \begin{array}{c} \underline{\dot{\boldsymbol{\epsilon}}}^1 \\ \underline{\dot{\boldsymbol{\epsilon}}}^2 \end{array} \right\} = \underline{\underline{\boldsymbol{L}}}^+ \dot{\boldsymbol{\epsilon}} \tag{6.42}$$

Although the solution of Eq. (6.42) minimizes both $\mathcal{F}$ and $||\dot{\boldsymbol{\epsilon}}^1 \dot{\boldsymbol{\epsilon}}^{2T}||$, it does not necessarily minimizes the microscopic plastic dissipation of $\pi(\dot{\boldsymbol{\epsilon}}^1, \dot{\boldsymbol{\epsilon}}^2)$ in Eq. (6.32) – it only minimizes its numerator. The denominator, which is a function of the microscopic strain rate Lode angles ξ^1 and ξ^2 as well as of the auxiliary angle $\beta = \dot{\epsilon}^2_{eq}/\dot{\epsilon}^1_{eq}$, is a much more complex function to be optimized. Therefore, the choice of an inverse for the rectangular matrix $\underline{\underline{\boldsymbol{L}}}$ consists in an additional upper bound approximation.

The inverses $\left(\underline{\underline{\boldsymbol{L}}}^+\right)^1$ and $\left(\underline{\underline{\boldsymbol{L}}}^+\right)^2$ are finally obtained by separating the 12×6 matrix $\underline{\underline{\boldsymbol{L}}}^+$ into two 6×6 blocks:

$$\left\{ \begin{array}{c} \underline{\dot{\boldsymbol{\epsilon}}}^1 \\ \underline{\dot{\boldsymbol{\epsilon}}}^2 \end{array} \right\} = \underline{\underline{\boldsymbol{L}}}^+ \underline{\dot{\boldsymbol{\epsilon}}} = \left[\begin{array}{c} \left(\underline{\underline{\boldsymbol{L}}}^+\right)^1 \\ \left(\underline{\underline{\boldsymbol{L}}}^+\right)^2 \end{array} \right] \underline{\dot{\boldsymbol{\epsilon}}}. \tag{6.43}$$

Coherently to the previous chapters in the present text and to section 6.2, $\dot{\boldsymbol{\epsilon}}$ is approximated by the trial microscopic strain rate $\dot{\boldsymbol{\epsilon}}_G(\dot{\boldsymbol{E}})$ proposed by Gurson (1977). This choice consists of a rigorous upper bound approach for the minimization problem of the macroscopic plastic dissipation potential $\Pi(\dot{\boldsymbol{E}})$, and leads to the following implementation of $\dot{\boldsymbol{\epsilon}}^1$ and $\dot{\boldsymbol{\epsilon}}^2$:

$$\begin{aligned} \underline{\dot{\boldsymbol{\epsilon}}}^1(\dot{\boldsymbol{E}}) &= \left(\underline{\underline{\boldsymbol{L}}}^+\right)^1 \underline{\dot{\boldsymbol{\epsilon}}}_G(\dot{\boldsymbol{E}}) \\ \underline{\dot{\boldsymbol{\epsilon}}}^2(\dot{\boldsymbol{E}}) &= \left(\underline{\underline{\boldsymbol{L}}}^+\right)^2 \underline{\dot{\boldsymbol{\epsilon}}}_G(\dot{\boldsymbol{E}}). \end{aligned} \tag{6.44}$$

It is important to recall one more time that further developments concerning this research will consider more refined trial velocity fields, as those of Monchiet, Charkaluk

and Kondo (2007), Monchiet, Charkaluk and Kondo (2011), Monchiet and Kondo (2012) and Li, Sauer and Wang (2007).

Recalling that $\dot{\boldsymbol{E}}$ is fully determined by the prescription of both normalized macroscopic strain triaxiality H and Lode angle η (Eq. (3.28)), each point of the macroscopic yield surface in the space of macroscopic stresses is related to a pair (H, η). Hence, one must evaluate Eq. (6.27) for as many pairs (H, η) as possible in their respective domains so that the points comprehend the entire macroscopic yield surface. Due to the computational cost of each integration in Eq. (6.27), only a reduced set of $\boldsymbol{\Sigma}$ is calculated for each macroscopic yield surface, which is thus correspondent to the prescribed set of pairs (H, η). Further details of these discretizations are given in section 7.2.

Along the same lines as the previous chapters, although the implementation is not restricted to the coincidence between the principal directions of the material matrix symmetry and the macroscopic strain rate $\dot{\boldsymbol{E}}$, the graphical visualization based on contour level plots of the macroscopic yield surfaces is. This limitation derives from the fact that if there is no coincidence between those principal directions, each point of that surface would be defined in a 6-dimensional space, since the shear components of stress would not result in zero. Thus, a contour level plot for 6-dimensional would be required, which implies an extreme computational cost. Nevertheless, an N-dimensional contour plot procedure is proposed in Appendix B for further developments in high performance computing.

6.6 Results and discussion

Following the formulation detailed in previous sections, two macroscopic yield surfaces are obtained by modeling a Gurson-like RVE whose material matrix follows the Yld2004-18p yield criterion. They are intended to insert the porosity effect in the yield surfaces of 6111-T4 and 2090-T3 aluminum alloys presented by Barlat et al. (2005). The material matrix coefficients of the RVE are assumed to be those identified by Barlat et al. (2005) and listed in Table 6. The shape parameter of the Hershey-Hosford equation is chosen to be $m = 8$, which is in correspondence to a FCC crystal structure. A porosity of 1% is chosen to represent a critical value for general ductile fracture configurations, as indicated by Benzerga, Besson and Pineau (1999). According to section 6.2, only centered spherical voids are hereby considered so that every noticeable anisotropic behavior is due to the material matrix model.

Figures 35 and 36 respectively compare the anisotropic macroscopic yield surface of a porous 6111-T4 and 2090-T3 aluminum alloy to a porous isotropic reference. In accordance with the material matrix behaviors, the macroscopic yield surfaces for 6111-T4 (B1) and 2090-T3 (B2) present a mildly and strongly anisotropic behavior, respectively. Figures 35a and 36a compares the macroscopic yield surfaces (B1 and B2) to an isotropic

reference (I). Although Fig. 35b and 36b do not contain the isotropic reference, a more significant effect of anisotropy can be noticed by the discrepancy between meridional planes related to different macroscopic stress Lode angles θ. Both deviatoric and meridional planes match the expectations about the intensity of the anisotropic effect of the microscopic yield criterion on the overall behavior.

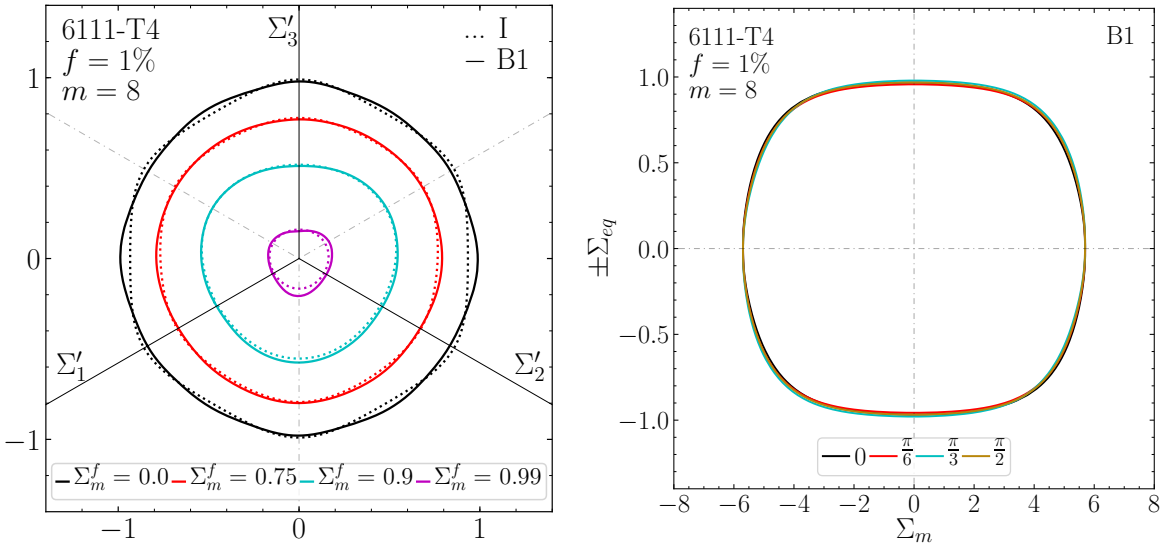

(a) deviatoric planes

(b) meridional planes

Figure 35: macroscopic yield surface for the 6111-T4 aluminum alloy with porosity $f = 1\%$ and shape parameter $m = 8$.

Contour plots for different levels of (a) $\Sigma^f_m = \Sigma_m/|\Sigma_m|_{max}$; and (b) macroscopic stress Lode angle θ ($\Sigma_{eq} \geq 0$) and $\theta + \pi$ ($\Sigma_{eq} < 0$). In both curves, one assumes $\sigma_0 = 1$ for the sake of simplicity. Source: the author.

In the deviatoric planes in Fig. 35a and Fig. 36a, the misalignment of the anisotropic curves naturally becomes more significant as the macroscopic hydrostatic stress Σ_m increases. Although it cannot be analytically shown for the formulation in this chapter due to the complexity of Eq. (6.27), this effect is believed to be analogous to the one observed in section 5.5, where it has been demonstrated that once the macroscopic IPE stress $\boldsymbol{\Sigma}^{*\prime}$ was proved to be centered on the deviatoric plane related to $\Sigma_m = 0$, the linear transformation $\boldsymbol{\Sigma}' = \mathbb{L}^+ : \boldsymbol{\Sigma}^*$ could not result in a misaligned $\boldsymbol{\Sigma}'$ for $\Sigma_m = 0$.

A stronger anisotropic effect might also be noticed in Fig. 36b in comparison with Fig. 35b, since discrepancies between meridional planes related to different macroscopic stress Lode angles θ are more marked in the first than in the last one. Furthermore, the meridional planes are not expected to be asymmetric, since the i) function $g(\omega^1, \omega^2\, \alpha)$ is symmetric with respect to ω^1 and ω^2 (i.e. $g(\omega^1, \omega^2, \alpha) = g(-\omega^1, \omega^2, \alpha) = g(\omega^1, -\omega^2, \alpha)$); ii) the trial strain rate fields $\dot{\boldsymbol{\epsilon}}^1$ and $\dot{\boldsymbol{\epsilon}}^2$ are symmetrically distributed inside the domain Ω of the RVE (see Fig. 34); and iii) the void shape shares symmetric planes with the material anisotropy.

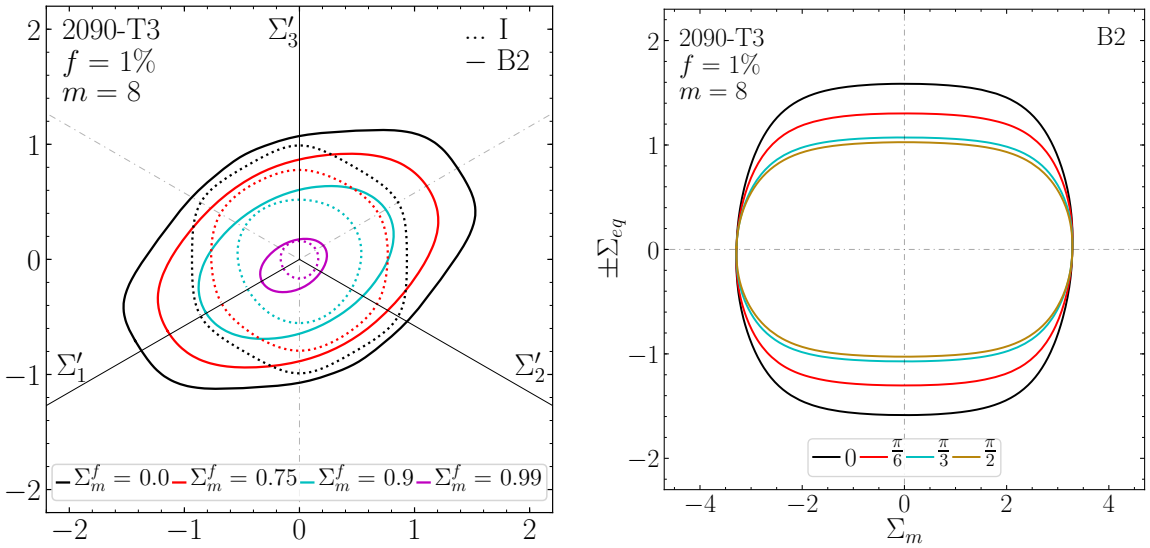

(a) deviatoric planes (b) meridional planes

Figure 36: macroscopic yield surface for the 2090-T3 aluminum alloy with porosity $f = 1\%$. Contour plots for different levels of (a) $\Sigma_m^f = \Sigma_m/|\Sigma_m|_{max}$; and (b) macroscopic stress Lode angle θ ($\Sigma_{eq} \geq 0$) and $\theta + \pi$ ($\Sigma_{eq} < 0$). In both curves, one assumes $\sigma_0 = 1$ for the sake of simplicity. Source: the author.

In order to verify the consistency of the present formulation, Fig. 37 compares the deviatoric planes related to $\Sigma_m = 0$ for the 6111-T4 and 2090-T3 porous aluminum alloys with the correspondent ones with no porosity (i.e. $f = 0$). The yield surface of the nonporous models are multiplied here by a scalar factor of $(1 - f)$, so that the amplification effect due to the porosity could be negligible.

Both Fig. 37a and 37b show that the combination of two linear transformations on the microscopic stress tensor carried out throughout the formulation proposed in this chapter alters the general aspect of the macroscopic yield surfaces slightly. Hence, the outcome of inserting the porosity effect in the Yld2004-18p criterion proposed by Barlat et al. (2005) is a change in the overall shape of the yield function, even in the contour level of $\Sigma_m = 0$, which has preserved its form in the last two other approaches presented in chapter 4 and chapter 5.

6.7 Concluding remarks

The formulation proposed in this chapter has revealed to be a consistent way of inserting the porosity effect in the yield criterion Yld2004-18p proposed by Barlat et al. (2005). Furthermore, the macroscopic yield surfaces obtained hereupon are in accordance with convexity requirements for general yield criteria for ductile media.

Differently from the results shown in chapter 5, there was a slight discrepancy

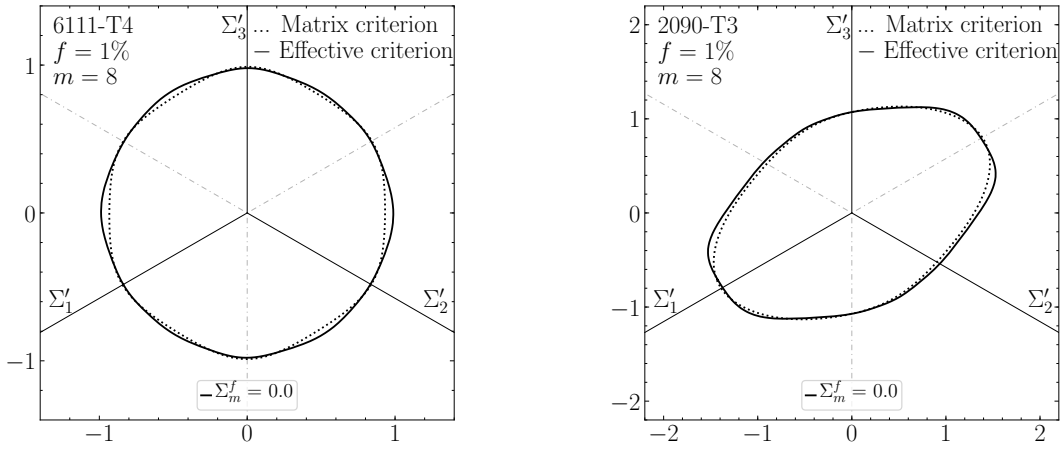

(a) 6111-T4 (b) 2090-T3

Figure 37: Comparison between deviatoric planes of macroscopic yield surface of porous aluminum alloys and microscopic yield surface for continuum aluminum alloys.

Each figure depicts a comparison between deviatoric planes for $\Sigma^f_m = \Sigma_m/|\Sigma_m|_{max} = 0$ of i) the macroscopic yield surface obtained by contour plots (continuous lines) and ii) the microscopic yield surface obtained directly by the Yld2004-18p model multiplied by a scalar factor $(1 - f)$ (dashed lines). One assumes $\sigma_0 = 1$ for the sake of simplicity. Source: the author.

between the deviatoric planes for $\Sigma_m = 0$ of the macroscopic yield surface and the microscopic one. This difference is believed to be due to the effect of applying two linear transformations instead of just one in the RVE general formulation, even though it was not possible to demonstrate it analytically.

Finally, although the overall results have shown to be in accordance with the expectations, the next steps of research must consist of (i) using more refined trial velocity fields with the aim of obtaining better upper bound approximations; and (ii) further experimental works to properly validate the approach presented hereby: differently to those tests made by Barlat et al. (2005), the *porosity* must also be controlled over the course of experiments from now on.

7 SOME ASPECTS ON THE NUMERICAL IMPLEMENTATION

7.1 Numerical integration

The linearization of the microscopic plastic dissipation potential $\pi(\dot{\boldsymbol{\epsilon}}_G)$ (Eq. (3.51)) in the original Gurson (1975) model allowed the macroscopic stress state to be obtained analytically, since the volume integral in Eq. (3.51) – and implicitly in Eq. (3.52) – could be solved analytically. However, the anisotropic extensions proposed in chapter 4, chapter 5 and chapter 6 require the macroscopic stress tensors $\boldsymbol{\Sigma} = \partial \Pi / \partial \dot{\boldsymbol{E}}$ to be numerically obtained (i.e. by using some approximation technique). Thus, a numerical integration procedure based on the Gauss quadrature was implemented to solve integrals in the form

$$\boldsymbol{\Sigma} = \frac{1}{V} \int_{\Omega} \frac{\partial \pi}{\partial \dot{\boldsymbol{E}}} dV. \tag{7.1}$$

The spherical shape of the RVEs suggests that a spherical *coordinate system* (Fig. 10) should be conveniently used. Thus, the integration in Eq. (7.1) is rewritten as

$$\boldsymbol{\Sigma} = \frac{1}{V} \int_{r_v}^{R} \int_{0}^{2\pi} \int_{0}^{\pi} \frac{\partial \pi}{\partial \dot{\boldsymbol{E}}} r^2 \sin\theta \, d\theta \, d\varphi \, dr, \tag{7.2}$$

where

$$r(x_1, x_2, x_3) = \sqrt{x_1^2 + x_2^2 + x_3^2}, \tag{7.3}$$

$$\varphi(x_1, x_2, x_3) = \arctan \frac{x_2}{x_1}, \tag{7.4}$$

$$\theta(x_1, x_2, x_3) = \arctan \frac{x_3}{\sqrt{x_1^2 + x_2^2 + x_3^2}},$$

$$x_1(r, \varphi, \theta) = r \sin\theta \cos\varphi, \tag{7.5}$$

$$x_2(r, \varphi, \theta) = r \sin\theta \sin\varphi, \tag{7.6}$$

$$x_3(r, \varphi, \theta) = r \cos\theta \qquad \text{and} \tag{7.7}$$

$$dV = dx_1 dx_2 dx_3 = r^2 \sin\theta \, d\theta \, d\varphi \, dr. \tag{7.8}$$

Although a spherical coordinate system is convenient for evaluating a certain function at a point in the RVE domain, the *referential frame* associated to that point is also dependent on the point position. This means that, during a numerical integration procedure of Eq. (7.2), each elementary parcel of the macroscopic stress tensor $\boldsymbol{\Sigma}$ would be calculated for a different referential frame. Therefore, the integrand function (i.e. $\partial \pi / \partial \dot{\boldsymbol{E}}$

in Eq. (7.2)) must be rotated to a fixed frame of reference so that each parcel of $\boldsymbol{\Sigma}$ is obtained in the same referential: the cartesian one. The corrected integration then holds

$$\boldsymbol{\Sigma} = \frac{1}{V}\int_{r_v}^{R}\int_{0}^{2\pi}\int_{0}^{\pi} \boldsymbol{M}(\varphi,\theta)\cdot\frac{\partial\pi}{\partial\dot{\boldsymbol{E}}}\cdot\boldsymbol{M}^T(\varphi,\theta)r^2\sin\theta d\theta d\varphi dr, \tag{7.9}$$

where the rotation tensor $M(\varphi,\theta)$ is given by

$$\boldsymbol{M}(\varphi,\theta) = \begin{bmatrix} \cos\varphi\sin\theta & \cos\varphi\cos\theta & -\sin\varphi \\ \sin\varphi\sin\theta & \sin\varphi\cos\theta & \cos\varphi \\ \cos\theta & -\sin\theta & 0 \end{bmatrix}. \tag{7.10}$$

The final expression for the numerical integration of Eq. (7.9) for (N_1, N_2, N_3) integration points in the directions (θ, φ, r), respectively, and in terms of the natural coordinates (ρ^i, ρ^j, ρ^k) given by the Gauss quadrature, reads

$$\boldsymbol{\Sigma} \approx \frac{1}{V}\sum_{k=1}^{N_3}\sum_{j=1}^{N_2}\sum_{i=1}^{N_1} w_3^k w_2^j w_1^i \left[\boldsymbol{M}(\varphi^j,\theta^i)\cdot\frac{\partial\pi}{\partial\dot{\boldsymbol{E}}}(r^k,\varphi^j,\theta^i)\cdot\boldsymbol{M}^T(\varphi^j,\theta^k)\right](r^k)^2\sin\theta^i J_\rho, \tag{7.11}$$

where (w^i, w^j, w^k) are the Gauss weights associated to the natural coordinates (ρ^i, ρ^j, ρ^k); J_ρ is the jacobian determinant to map the Gauss natural coordinate system (ρ^i, ρ^j, ρ^k) to the spherical one (r, φ, θ); and the variables $(r^k, \varphi^j, \theta^i)$ are the spherical coordinates described in terms of the Gauss natural coordinate system (ρ^i, ρ^j, ρ^k):

$$r^k = r^k(\rho^i,\rho^j,\rho^k) = \frac{1}{2}[R - r_v(\varphi^j(\rho^j),\theta^i(\rho^i))](\rho^k+1) + r_v(\varphi^j(\rho^j),\theta^i(\rho^i)), \tag{7.12}$$

$$\varphi^j = \varphi^j(\rho^j) = \pi(\rho^j+1), \tag{7.13}$$

$$\theta^i = \theta^i(\rho^i) = \frac{\pi}{2}(\rho^i+1), \tag{7.14}$$

$$J_\rho = J_\rho(\rho^i,\rho^j,\rho^k) = \frac{\pi^2}{4}[R - r_v(\varphi^j(\rho^j),\theta^i(\rho^i))] \qquad \text{and} \tag{7.15}$$

$$r_v(\varphi^j(\rho^j),\theta^i(\rho^i)) = \frac{1}{\sqrt{\left(\frac{\cos\varphi^j\sin\theta^i}{r_1}\right)^2 + \left(\frac{\sin\varphi^j\sin\theta^i}{r_2}\right)^2 + \left(\frac{\cos\theta^i}{r_3}\right)^2}}. \tag{7.16}$$

The void radius $r_v = r_v(\varphi,\theta)$ is assumed to be dependent on the angles φ and θ because of the possibility of it being an ellipsoid, as in chapter 4. However, for the subsequent chapter 5 and chapter 6, the void is assumed to be spherical and hence the void radius is constant.

The results provided in chapter 4, chapter 5 and chapter 6 were obtained by using Gauss quadrature of $(N_1, N_2, N_3) = (40, 40, 40)$ integration points. However, the isotropic

results obtained to illustrate Benallal, Desmorat and Fournage (2014) and Benallal (2017) models required only $(N_1, N_2, N_3) = (15, 15, 15)$ points to be accurately integrated – $40^3/15^3 \approx 28402$, which has a strong impact on the computational cost.

7.2 Discretization of the η and H subspaces

The trial strain rate field $\dot{\boldsymbol{\epsilon}}_G(r, \varphi, \theta)$ in Eq. (3.49) is also a function of two macroscopic strain rate invariants: $\dot{E}_m$ (or H) and η. This means that $\dot{\boldsymbol{\epsilon}}_G$ not only varies in the space (i.e. in the RVE domain), but also following two additional variables (H, η). Moreover, the numerical integration framework given by Eq. (7.11) is related to only a given pair (H, η), which are purposely implicit in that equation. Therefore, the integration in Eq. (7.11) results in solely *one* stress tensor – i.e. one point on the macroscopic yield surface. In order to obtain the whole surface, the invariants (H, η) of $\dot{\boldsymbol{E}}$ must be treated also as variables and thus require a discretization.

According to the definition of the macroscopic strain rate triaxiality (Eq. (3.33)), $H \in [-\infty, \infty]$. Therefore, its discretization cannot be effectively performed, since it is an unbounded domain. To address this issue, a change of variables is hereby proposed. This change does not affect the formulation itself – neither destroys the conceptual meaning of the triaxiality. The advantage of that change of variables is that the idealized triaxiality variable $\tilde{H} \in [-1/\sqrt{3}, 1/\sqrt{3}]$. Thus, a traditional discretization procedure can be applied. The new strain rate triaxiality variable is

$$\tilde{H} = \frac{H}{\sqrt{\frac{3}{2} + 3H^2}} \tag{7.17}$$

and

$$\lim_{H \to -\infty} \tilde{H} = -\frac{1}{\sqrt{3}}, \tag{7.18}$$

$$\lim_{H \to 0} \tilde{H} = 0 \qquad \text{and} \tag{7.19}$$

$$\lim_{H \to \infty} \tilde{H} = \frac{1}{\sqrt{3}} \tag{7.20}$$

It is important to remark that due to the *perfectly* rigid-plastic material matrix of the RVE and to the small strains theory used throughout this formulation, the resultant macroscopic stress tensor $\boldsymbol{\Sigma}$ given in Eq. (7.11) is independent on the intensity of $\dot{\boldsymbol{E}}$ (i.e. on the norm $||\dot{\boldsymbol{E}}||$). Therefore, $\boldsymbol{\Sigma}$ depends only on the *directions* of $\dot{\boldsymbol{E}}$, given by its triaxiality H and Lode angle η. An auxiliary macroscopic strain rate $\tilde{\dot{\boldsymbol{E}}}$ can then be defined

in terms of $\tilde{H}$ and η in such way that its euclidean norm be unitary:

$$\tilde{\boldsymbol{E}} = \frac{\dot{\boldsymbol{E}}}{||\dot{\boldsymbol{E}}||} = \sqrt{\frac{2}{3}(1-3\tilde{H}^2)}\boldsymbol{e}'(\eta) + \tilde{H}\mathbf{1}, \tag{7.21}$$

where $\boldsymbol{e}'(\eta)$ is the unitary deviatoric strain tensor given by Eq. (3.32).

A generalization of the macroscopic strain rate Lode angle η is also hereby proposed for convenience. Because the classical definition of the Lode angle in Eq. (3.34), $\eta \in [0, \pi/3]$ so that the ordination $\dot{E}_1 \geq \dot{E}_2 \geq \dot{E}_3$, with $\dot{E}_1 > \dot{E}_3$, can be respected. This is particularly inconvenient for the anisotropic analyses treated hereby in which the principal directions of $\dot{\boldsymbol{E}}$ coincide with the material referential frame (x_1, x_2, x_3). In these analyses, full yield surfaces (i.e. including cases where the stress ordination is not respected) can be obtained only by extending the range of the Lode angle (both η and Θ) to $[0, 2\pi]$. This extension avoids the need to account for permutations of the principal directions that are required to obtain full (i.e. closed, not limited to the sector $\Sigma_1 \geq \Sigma_2 \geq \Sigma_3$, $\Sigma_1 > \Sigma_3$) yield surfaces. An illustration of the extended Lode angle $\tilde{\eta}$ is provided in Fig. 38. This angle can be defined as

$$\tilde{\eta} = sign\frac{1}{3}\arccos\left(\frac{4\det\dot{\boldsymbol{E}}'}{(\dot{E}_{eq})^3}\right) + \frac{2k\pi}{3}, \quad k \in \mathbb{Z} \tag{7.22}$$

where

$$sign = +1 \quad k = 0 \quad \text{for} \dot{E}_1 \geq \dot{E}_2 \geq \dot{E}_3,\ \dot{E}_1 > \dot{E}_3, \tag{7.23a}$$
$$sign = -1 \quad k = 1 \quad \text{for} \dot{E}_2 \geq \dot{E}_1 \geq \dot{E}_3,\ \dot{E}_2 > \dot{E}_3, \tag{7.23b}$$
$$sign = +1 \quad k = 1 \quad \text{for} \dot{E}_2 \geq \dot{E}_3 \geq \dot{E}_1,\ \dot{E}_2 > \dot{E}_1, \tag{7.23c}$$
$$sign = -1 \quad k = 2 \quad \text{for} \dot{E}_3 \geq \dot{E}_2 \geq \dot{E}_1,\ \dot{E}_3 > \dot{E}_1, \tag{7.23d}$$
$$sign = +1 \quad k = 2 \quad \text{for} \dot{E}_3 \geq \dot{E}_1 \geq \dot{E}_2,\ \dot{E}_3 > \dot{E}_2, \tag{7.23e}$$
$$sign = -1 \quad k = 3 \quad \text{for} \dot{E}_1 \geq \dot{E}_3 \geq \dot{E}_2,\ \dot{E}_1 > \dot{E}_2. \tag{7.23f}$$

Although specific anisotropy symmetries implies their respective yield surfaces to present certain symmetry planes as well, as shown by Canova et al. (1985), the results hereby presented were obtained by varying the macroscopic strain rate parameters in their whole range: $\tilde{H} \in [-1/\sqrt{3}, 1/\sqrt{3}]$ and $\tilde{\eta} \in [0, 2\pi]$. Two numerical criteria were then implemented to discretize those variables.

Basically, the Lode angle $\tilde{\eta}$ is uniformly divided in the range $[0, 2\pi]$ in $N_{\tilde{\eta}}$ points. Differently, the triaxiality $\tilde{H}$ is divided by following a heuristic criterion so that the stress points on meridional planes could be as equally spaced as possible for a fixed number of points $N_{\tilde{H}}$. This criterion uses the analytical expressions Eq. (3.54), provided by Gurson (1975), to calculate the values of $\tilde{H}$ for which the macroscopic stress points $(\Sigma_m^G, \Sigma_{eq}^G)$

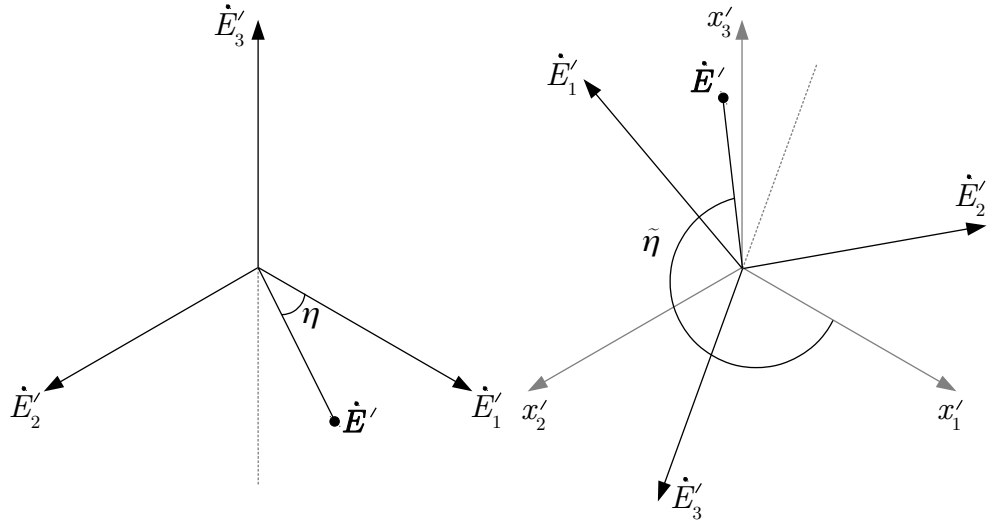

Figure 38: A generalization of the Lode angle concept to arbitrary material referential system. On the left, a deviatoric macroscopic strain rate $\dot{\boldsymbol{E}}'$ is illustrated lying on the deviatoric plane. The Lode angle $\eta \in [0, \pi/3]$ is then illustrated as the angle formed by the deviatoric axis $\dot{E}'_1$ and $\dot{\boldsymbol{E}}'$. On the right, the principal macroscopic axes $(\dot{E}'_1, \dot{E}'_2, \dot{E}'_3)$ are positioned in a material deviatoric referential system (x'_1, x'_2, x'_3). A reinterpretation of the Lode angle is then proposed: the angle $\tilde{\eta} \in [0, 2\pi]$ is measured from the deviatoric material axis x'_1 to $\dot{\boldsymbol{E}}'$. Source: the author.

obtained by the original Gurson (1975) model can be equally spaced. That discretization of $\tilde{H}$ is thus assumed to be a reasonable estimate for the optimum set of triaxialities that should imply equally spaced (Σ_m, Σ_{eq}) in macroscopic meridional planes.

The results presented in chapter 4, chapter 5 and chapter 6 were obtained by prescribing $N_{\tilde{\eta}} = 180$ and $N_{\tilde{H}} = 221$ (i.e. $180 \cdot 221 = 39780$ pairs $(\tilde{\eta}, \tilde{H})$) for each macroscopic yield surface. For each of those pairs, a numerical integration of Eq. (7.11) based on the Gauss quadrature with $40 \cdot 40 \cdot 40 = 64000$ points were therefore performed, as indicated in section 7.1.

7.3 From macroscopic strain rates to macroscopic stresses: Contour (level set) plots

The procedure of obtaining macroscopic stress $\boldsymbol{\Sigma}$ points by evaluating Eq. (7.11) for a given number of pairs $(\eta, \tilde{H})$ results in a set of points of $\boldsymbol{\Sigma}$ that certainly lie on the macroscopic yield surface. However, this set of stress points must be interpolated in some way so that an arbitrary stress state that does not necessarily coincide with any of the points in this set – but that also lies on the yield surface – could be approximately obtained by interpolation. Hence, the interpolation procedure would profit from the yield surface points that would have already been obtained to avoid the need of evaluating the demanding integration in Eq. (7.11) to obtain new points.

This interpolation procedure is particularly required to obtain meridional and deviatoric level-set curves – as extensively used in chapter 4, chapter 5 and chapter 6. These curves represent the intersections of the macroscopic yield surface with the following planes: i) meridional ($\Theta = \bar{\Theta}$, where $\bar{\Theta}$ is a prescribed level of Θ); and ii) deviatoric ($\Sigma_m = \bar{\Sigma}_m$, where $\bar{\Sigma}_m$ is a prescribed value of Σ_m), as illustrated in Fig. 7 and 8.

Generally, contour (or level-set) plots of an arbitrary surface, represented by a finite set Γ of points lying on it, can be numerically derived by firstly dividing the surface domain into elements (or subdomains). These subdomains can be defined, for example, by subsets composed of adjacent points in Γ, as illustrated in Fig. 39. Secondly, an interpolation procedure must be performed to obtain the approximated position of new points lying on a prescribed regular grid in each of those subdomains (Fig. 40). This interpolation procedure must consider a natural (i.e. dimensionless) coordinate system (ι_1, ι_2) (Fig. 41) from which shape functions $\chi_i(\iota_1, \iota_2)$ for $i = 1, 2, 3, 4$ can be deduced, as in Eq. (7.24). The expressions of the interpolated macroscopic stress $\boldsymbol{\Sigma}$, strain rate Lode angle η and triaxiality $\tilde{H}$ are given in Eq. (7.25). Finally, the algorithm must search in each point of the regular grids inside each subdomain for those that respect a prescribed level-set condition (e.g. $\Theta = \bar{\Theta}$ for meridional planes or $\Sigma_m = \bar{\Sigma}_m$ for deviatoric planes).

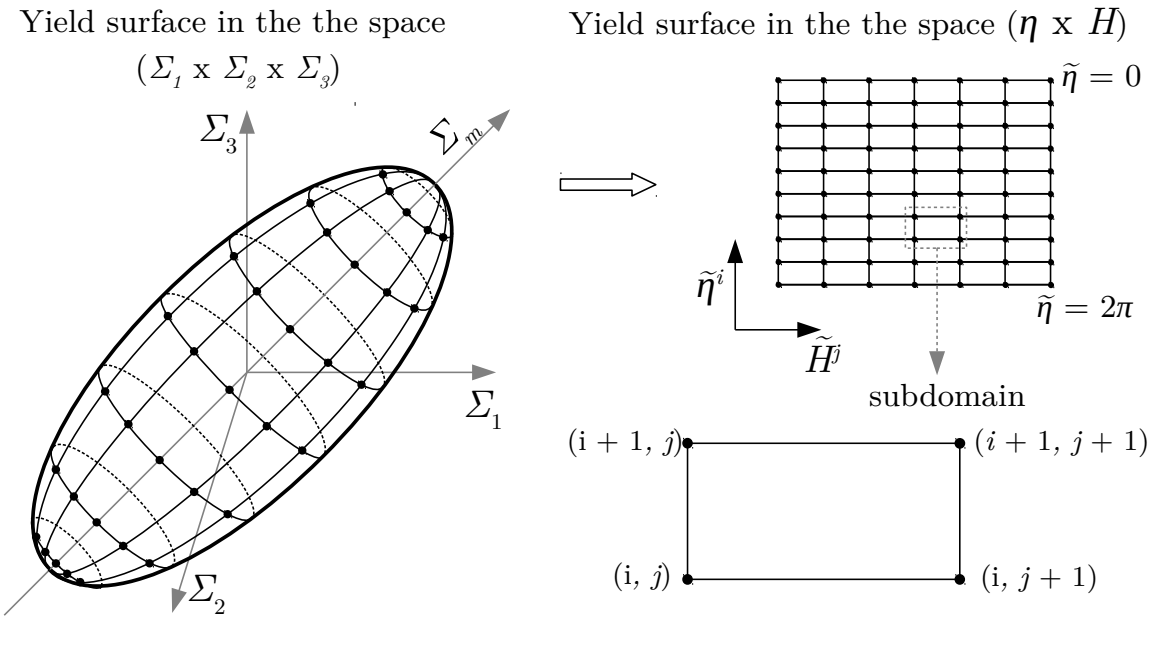

Figure 39: Illustration of a subdomain of the yield surface in the space of the macroscopic strain rates.

Source: the author.

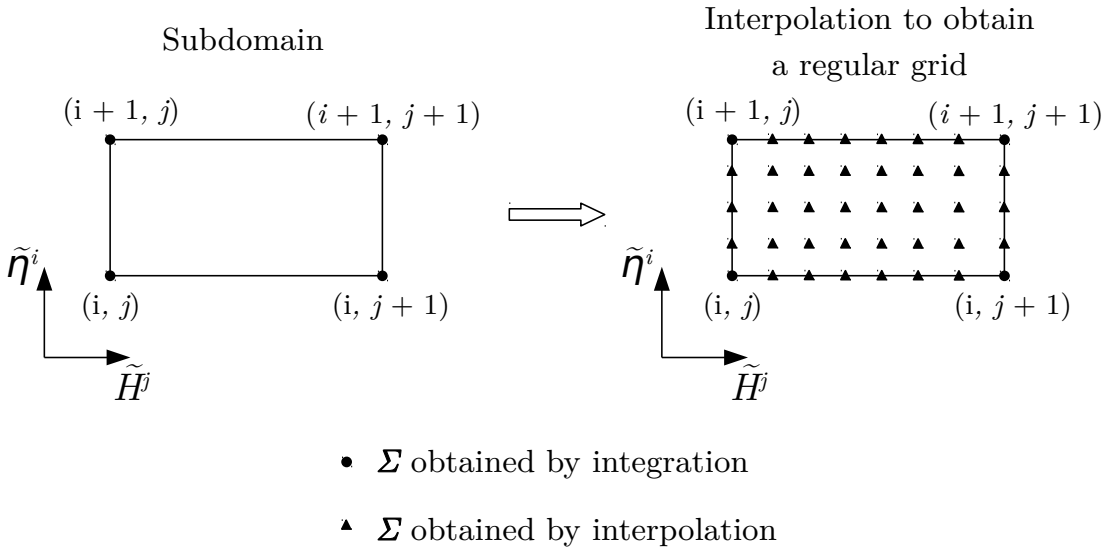

Figure 40: Interpolation in a subdomain to obtain a regular grid of approximated points lying on the yield surface.

Source: the author.

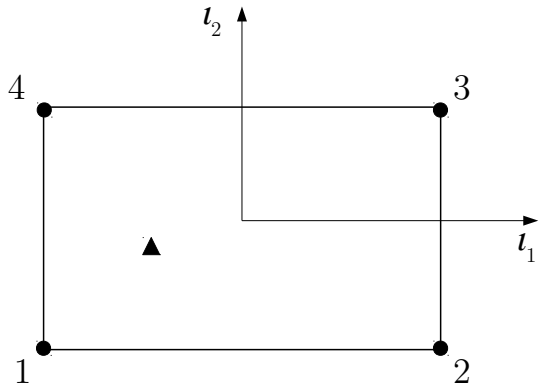

Figure 41: Natural coordinate system (ι_1, ι_2) in a quadrilateral subdomain.

Source: the author.

$$\chi_1(\iota_1, \iota_2) = \frac{1}{4}(\iota_1 + 1)(\iota_2 - 1) \tag{7.24a}$$

$$\chi_2(\iota_1, \iota_2) = \frac{1}{4}(\iota_1 - 1)(\iota_2 - 1) \tag{7.24b}$$

$$\chi_3(\iota_1, \iota_2) = \frac{1}{4}(\iota_1 - 1)(\iota_2 + 1) \tag{7.24c}$$

$$\chi_4(\iota_1, \iota_2) = \frac{1}{4}(\iota_1 + 1)(\iota_2 + 1) \tag{7.24d}$$

$$\boldsymbol{\Sigma}^{\blacktriangle} \approx \boldsymbol{\Sigma}^{\blacktriangle}(\iota_1, \iota_2) = \boldsymbol{\Sigma}_1^{\bullet}\chi_1(\iota_1, \iota_2) + \boldsymbol{\Sigma}_2^{\bullet}\chi_2(\iota_1, \iota_2) + \boldsymbol{\Sigma}_3^{\bullet}\chi_3(\iota_1, \iota_2) + \boldsymbol{\Sigma}_4^{\bullet}\chi_4(\iota_1, \iota_2) \quad (7.25a)$$

$$\tilde{\eta}^{\blacktriangle} \approx \tilde{\eta}^{\blacktriangle}(\iota_1, \iota_2) = \tilde{\eta}_1^{\bullet}\chi_1(\iota_1, \iota_2) + \tilde{\eta}_2^{\bullet}\chi_2(\iota_1, \iota_2) + \tilde{\eta}_3^{\bullet}\chi_3(\iota_1, \iota_2) + \tilde{\eta}_4^{\bullet}\chi_4(\iota_1, \iota_2) \quad (7.25b)$$

$$\tilde{H}^{\blacktriangle} \approx \tilde{H}^{\blacktriangle}(\iota_1, \iota_2) = \tilde{H}_1^{\bullet}\chi_1(\iota_1, \iota_2) + \tilde{H}_2^{\bullet}\chi_2(\iota_1, \iota_2) + \tilde{H}_3^{\bullet}\chi_3(\iota_1, \iota_2) + \tilde{H}_4^{\bullet}\chi_4(\iota_1, \iota_2) \quad (7.25c)$$

For two-dimensional surfaces described in three-dimensional spaces, commercial and community codes were implemented to perform contour plots within practically instantaneous computations. However, these codes do not account for an important peculiarity that arises from the anisotropic yield surfaces obtained hereby. They are not capable of identifying the equivalence of a stress Lode angles $\Theta = 0 \equiv 2\pi$. Besides, the set of points of anisotropic yield surfaces does not necessarily follow a strict increasing (or strict decreasing) order of Θ, which aggravates the apparent discontinuity between adjacent values of $\Theta = 2\pi - d\Theta_1$ and $\Theta = d\Theta_2$, where $d\Theta_1$ and $d\Theta_2$ are sufficiently small.

Thus, an adapted contour function was implemented in Python programming language. This code accounts for the periodicity of the parameters to be prescribed as level-set conditions. The meridional and deviatoric curves throughout this document were obtained by using this implementation.

8 CONCLUSION AND FURTHER WORK

Within the assumptions considered in this work – the choice of the trial field and RVE geometry –, the modeling of different void morphologies in a Gurson-like spherical RVE has shown to be adequate only for high triaxialities. Additionally, these effects could only be noticeable for porosities greater than 1%. This weak influence of the void morphology on the macroscopic anisotropy is actually due to the Gurson's trial microscopic strain rate field $\dot{\boldsymbol{\epsilon}}_G$, which was conceived for isotropic models considering spherical voids. Notwithstanding, the results show a consistent formulation that accurately captures the influence of ellipsoidal void orientations and motivated the study of matrix-induced anisotropy.

The results obtained when including the anisotropy of the matrix lying on the same kind of assumptions seem encouraging and need to be improved by more elaborate kinematically admissible velocity fields associated to anisotropic materials. In these analyses, the resultant macroscopic yield surfaces are sensitive to the anisotropic parameters regardless of the material symmetry involved in them.

The generalization of the microscopic yield criterion to include yield functions such as those of Barlat et al. (2005) leads to indefinitely increasing the number of anisotropy parameters to characterize porous ductile materials. In the examples shown hereby, yield surfaces of two aluminum alloys are obtained by inserting the effect of a hypothetical porosity $f = 1\%$. In both cases, the porosity affected the overall aspect of the yield surfaces even for purely deviatoric loads (i.e. traceless loads whose principal directions coincide with those of the material symmetry). This fact encourages further experimental investigation on the characterization of porous aluminum alloys based on the formulation herein provided.

In order to be able to apply loads whose principal directions do not coincide with the anisotropic symmetry orientations, these formulations must be implemented in a high performance computing language – such as High Performance Fortran (HPF), for example, which is optimized for clustering and multithreading computers. This is required due to the necessity of varying the *principal directions* of the macroscopic strain rate – and not only its triaxiality and Lode angle –, which substantially increases the computation time. In these cases, the resultant yield surface must be described in terms of the six components of the stress tensor, and not only by its three invariants. Consequently, a six-dimensional level-set plot based on Appendix B must be applied so that those yield surfaces could be appropriately visualized in two-dimensional plots. This improvement should also allow trigonal, monoclinic and triclinic anisotropy symmetries to be considered in those formulations.

Another further step consists of implementing a porosity evolution law associated to anisotropic ductile materials. Initially, its formulation must be based solely on the void growth mechanism by considering the same definition as Gurson (1977) based on mass conservation law: $\dot{f} = (1 - f)\,\mathrm{Tr}\,\dot{\boldsymbol{E}}$. However, the challenging aspect is that the macroscopic hydrostatic strain rate $\dot{E}_m$ must now be obtained from an anisotropic surface described by a set of points, instead of an analytical closed expression.

The complementation of the present effective yield criteria with a future implementation of a porosity evolution law will make possible to apply the resultant model in multiscale three-dimensional FEM codes for ductile fracture propagation analyses. Although this future multiscale implementation will demand a high performance computational approach, most of the simplifications commonly assumed to make the development of closed-form expression feasible can be overcome.

BIBLIOGRAPHY

AGARWAL, H.; GOKHALE, A. M.; GRAHAM, S.; HORSTEMEYER, M. F. Anisotropy of intermetallic particle cracking damage evolution in an al-mg-si base wrought aluminum alloy under uniaxial compression. **Metallurgical and Materials Transactions A**, The Minerals, Metals & Materials Society, v. 33, p. 3443–3448, Nov. 2002. ISSN 1073-5623.

AGOGINO, A. M. Notch effects, stress state, and ductility. **Journal of Engineering Materials and Technology**, The American Society of Mechanical Engineers, v. 100, p. 348–355, 1978. ISSN 0094-4289.

ANDERSSON, H. Analysis of a model for void growth and coalescence ahead of a moving crack tip. **Journal of the Mechanics and Physics of Solids**, Elsevier Science, v. 25, p. 217–233, 1977. ISSN 0022-5096.

ARAVAS, N.; PONTE CASTAÑEDA, P. Numerical methods for porous metals with deformation-induced anisotropy. **Computer Methods in Applied Mechanics and Engineering**, Elsevier Science, v. 193, p. 3767–3805, 2004.

ARGON, A. S. Formation of cavities from nondeformable second-phase particles in low temperature ductile fracture. **Journal of Engineering Materials and Technology**, The American Society of Mechanical Engineers, v. 98, p. 60–68, 1976. ISSN 0094-4289.

ARGON, A. S.; IM, J. Separation of second phase particles in spheroidized 1045 steel, cu-0.6pct cr alloy, and maraging steel in plastic straining. **Metallurgical and Materials Transactions A**, The Minerals, Metals & Materials Society, v. 6, p. 839–851, Apr. 1975. ISSN 1073-5623.

ARGON, A. S.; IM, J.; SAFOGLU, R. Cavity formation from inclusions in ductile fracture. **Metallurgical and Materials Transactions A**, The Minerals, Metals & Materials Society, v. 6, p. 825–837, Apr. 1975. ISSN 1073-5623.

ASARO, R. J. Geometrical effects in the inhomogeneous deformation of ductile single crystals. **Acta Metallurgica**, Elsevier Science, v. 27, p. 445–453, 1979. ISSN 0001-6160.

ASHBY, M. F. Work hardening of dispersion-hardened crystals. **Philosophical Magazine**, Taylor and Francis Group, v. 14, p. 1157–1178, 1966. ISSN 1478-6435.

ASHBY, M. F. The deformation of plastically non-homogeneous materials. **Philosophical Magazine**, Taylor and Francis Group, v. 21, p. 399–424, 1970.

ASHBY, M. F.; JOHNSON, L. On the generation of dislocations at misfitting particles in a ductile matrix. **Philosophical Magazine**, Taylor and Francis Group, v. 20, p. 1009–1022, 1969.

BABOUT, L.; BRECHET, Y.; MAIRE, E.; FOUGÈRES, R. On the competition between particle fracture and particle decohesion in metal matrix composites. **Acta Materialia**, Elsevier Science, v. 52, p. 4517–4525, 2004. ISSN 1359-6454.

BANABIC, D.; ARETZ, H.; COMSA, D. S.; PARAIANU, L. An improved analytical description of orthotropy in metallic sheets. **International Journal of Plasticity**, Elsevier Science, v. 21, p. 493–512, 2005. ISSN 0749-6419.

BAO, Y.; WIERZBICKI, T. On fracture locus in the equivalent strain and stress triaxiality space. **International Journal of Mechanical Sciences**, Elsevier Science, v. 46, p. 81–98, 2004. ISSN 0020-7403.

BARLAT, F.; ARETZ, H.; YOON, J.; KARABIN, M.; BREM, J.; DICK, R. Linear transfomation-based anisotropic yield functions. **International Journal of Plasticity**, Elsevier Science, v. 21, p. 1009–1039, 2005. ISSN 0749-6419.

BARLAT, F.; BREM, J. C.; YOON, J. W.; CHUNG, K.; DICK, R. E.; LEGE, D. J.; POURBOGHRAT, F.; CHOI, S.-H.; CHU, E. Plane stress yield function for aluminum alloy sheets—part 1: theory. **International Journal of Plasticity**, Elsevier Science, v. 19, p. 1297–1319, 2003. ISSN 0749-6419.

BARLAT, F.; LIAN, K. Plastic behavior and stretchability of sheet metals. part i: A yield function for orthotropic sheets under plane stress conditions. **International Journal of Plasticity**, Elsevier Science, v. 5, p. 51–66, 1989. ISSN 0749-6419.

BARSOUM, I.; FALESKOG, J. Micromechanics of rupture in combined tension and shear. **Key Engineering Materials**, v. 345-346, p. 681–684, 2007.

BARSOUM, I.; FALESKOG, J. Rupture mechanisms in combined tension and shear—experiments. **International Journal of Solids and Structures**, Elsevier Science, v. 44, p. 1768–1786, 2007. ISSN 0020-7683.

BARSOUM, I.; FALESKOG, J. Rupture mechanisms in combined tension and shear—micromechanics. **International Journal of Solids and Structures**, Elsevier Science, v. 44, p. 5481–5498, 2007. ISSN 0020-7683.

BARSOUM, I.; FALESKOG, J. Micromechanical analysis on the influence of the lode parameter on void growth and coalescence. **International Journal of Solids and Structures**, Elsevier Science, v. 48, p. 925–938, 2011. ISSN 0020-7683.

BARSOUM, I.; FALESKOG, J.; PINGLE, S. The influence of the lode parameter on ductile failure strain in steel. **Procedia Engineering**, v. 10, p. 69–75, 2011. ISSN 1877-7058.

BEELEY, P. **Foundry Technology**. 2. ed. [S.l.]: Butterwooth–Heinemann, 2001.

BEN-ISRAEL, A.; GREVILLE, T. N. E. **Generalized Inverses: Theory and Applications**. 2nd. ed. New York: Springer-Verlag, 2003.

BENALLAL, A. Constitutive equations for porous solids with matrix behaviour dependent on the second and third stress invariants. **International Journal of Impact Engineering**, Elsevier Science, v. 108, p. 47–62, Oct. 2017.

BENALLAL, A.; DESMORAT, R.; FOURNAGE, M. An assessment of the role of the third stress invariant in the gurson approach for ductile fracture. **European Journal of Mechanics - A/Solids**, Elsevier Science, v. 47, p. 400–414, Sept. 2014. ISSN 0997-7538.

BENZERGA, A.; BESSON, J.; PINEAU, A. Anisotropic ductile fracture: Part ii: theory. **Acta Materialia**, Elsevier Science, v. 52, p. 4639–4650, 2004. ISSN 1359-6454.

BENZERGA, A. A. **Rupture ductile des tôles anisotropes**. 2000. 540 p. Doctoral dissertation (Sciences des Matériaux) — École des Mines de Paris, Paris, 2000.

BENZERGA, A. A.; BESSON, J.; PINEAU, A. Coalescence-controlled anisotropic ductile fracture. **Journal of Engineering Materials and Technology**, The American Society of Mechanical Engineers, v. 121, p. 221–229, Apr. 1999. ISSN 0094-4289.

BENZERGA, A. A.; BESSON, J.; PINEAU, A. Anisotropic ductile fracture: Part i: experiments. **Acta Materialia**, Elsevier Science, v. 52, p. 4623–4638, 2004. ISSN 1359-6454.

BENZERGA, A. A.; LEBLOND, J.-B. Ductile fracture by void growth to coalescence. In: VAN DER GIESSEN, E AND AREF, H. **Advances in Applied Mechanics**. [S.l.]: Academic Press, 2010. v. 44, p. 169–305. ISBN 9780123808783.

BEREMIN, F. M. Cavity formation from inclusions in ductile fracture of a508 steel. **Metallurgical and Materials Transactions A**, The Minerals, Metals & Materials Society, v. 12, p. 723–731, May 1981. ISSN 1073-5623.

BERNARD, G.; GRUMBACH, M.; MOLIEXE, F. Inclusions in steel plates and mechanical anisotropy. **Metals Technology**, v. 2, p. 512–521, Jan. 1975. ISSN 0307-1693.

BESSON, J. Continuum models of ductile fracture: A review. **International Journal of Damage Mechanics**, Sage Publications, v. 19, p. 3–52, 2010. ISSN 1056-7895.

BESSON, J.; CAILLETAUD, G.; CHABOCHE, J.-L.; FOREST, S. **Non-Linear Mechanics of Materials**. 1. ed. [S.l.]: Springer Netherlands, 2010. (Solid Mechanics and Its Applications 167).

BOURCIER, R.; KOSS, D.; SMELSER, R.; RICHMOND, O. The influence of porosity on the deformation and fracture of alloys. **Acta Metallurgica**, Elsevier Science, v. 34, p. 2443–2453, 1986. ISSN 0001-6160.

BROEK, D. The role of inclusions in ductile fracture and fracture toughness. **Engineering Fracture Mechanics**, Elsevier Science, v. 5, p. 55–66, 1973. ISSN 0013-7944.

BROWN, L. M.; EMBURY, J. D. The initiation and growth of voids at second phase particles. In: INST. OF METALS, 3., 1973, London. **Proc. 3rd Int. Conf. on Strength of Metals and Alloys**. London, 1973.

CAMPBELL, S. L.; MEYER, C. D. **Generalized Inverses of Linear Transformations**. London: Society for Industrial and Applied Mathematics, 2009. (Classics in Applied Mathematics).

CANOVA, G. R.; KOCKS, U. F.; TOMÉ, C. N.; JONAS, J. J. The yield surface of textured polycrystals†. **Journal of the Mechanics and Physics of Solids**, Elsevier Science, v. 33, p. 371–397, 1985. ISSN 0022-5096.

CAZACU, O.; REVIL-BAUDARD, B.; CHANDOLA, N.; KONDO, D. New analytical criterion for porous solids with tresca matrix under axisymmetric loadings. **International Journal of Solids and Structures**, Elsevier Science, v. 51, p. 861–874, Feb. 2014. ISSN 0020-7683.

CHENG, L.; MONCHIET, V.; MORIN, L.; SAXCé, G. de; KONDO, D. An analytical lode angle dependent damage model for ductile porous materials. **Engineering Fracture Mechanics**, Elsevier Science, v. 149, p. 119–133, Nov. 2015. ISSN 0013-7944.

CHIN, G. Y.; HOSFORD, W.; BACKOFEN, W. Ductile fracture of aluminum. **Trans. Metall. Soc.**, AIME, v. 230, p. 437–449, 1964. ISSN 0921-5093.

COWIN, S. C. **Continuum Mechanics of Anisotropic Materials**. New York: Springer-Verlag, 2013. XIII, 425 p.

COX, T. B.; LOW, J. R. An investigation of the plastic fracture of aisi 4340 and 18 nickel-200 grade maraging steels. **Metallurgical and Materials Transactions B**, The Minerals, Metals & Materials Society, v. 5, p. 1457–1470, June 1974. ISSN 1073-5615.

DANAS, K.; PONTE CASTAÑEDA, P. A finite-strain model for anisotropic viscoplastic porous media: I – theory. **European Journal of Mechanics - A/Solids**, Elsevier Science, v. 28, p. 387–401, 2009. ISSN 0997-7538.

DANAS, K.; PONTE CASTAÑEDA, P. A finite-strain model for anisotropic viscoplastic porous media: Ii – applications. **European Journal of Mechanics - A/Solids**, Elsevier Science, v. 28, p. 402–416, 2009. ISSN 0997-7538.

DANAS, K.; PONTE CASTAÑEDA, P. Influence of the lode parameter and the stress triaxiality on the failure of elasto-plastic porous materials. **International Journal of Solids and Structures**, Elsevier Science, v. 49, p. 1325–1342, 2012. ISSN 0020-7683.

DOWLING, N. E. **Mechanical Behavior of Materials**. 4. ed. [S.l.]: Pearson Education, 2013.

DUNAND, M.; MOHR, D. Effect of lode parameter on plastic flow localization after proportional loading at low stress triaxialities. **Journal of the Mechanics and Physics of Solids**, Elsevier Science, v. 66, p. 133–153, May 2014. ISSN 0022-5096.

EGGLESTON, H. G. **Convexity**. 1. ed. [S.l.]: Cambridge University Press, 1958. (Cambridge Tracts in Mathematics and Mathematical Physics).

ESHELBY, J. D. The determination of the elastic field of an ellipsoidal inclusion, and related problems. **Proceedings Mathematical Physical & Engineering Sciences**, The Royal Society, v. 241, p. 376–396, 1957. ISSN 1364-5021.

FERREIRA, A. R.; PROENÇA, S. P. B.; BENALLAL, A. An extended gurson model based approach for constitutive modeling of orthotropic porous solids (to be published). In: MECSOL 2019 7TH INTERNATIONAL SYMPOSIUM ON SOLID MECHANICS, 7., 2019, São Carlos. **Proceedings of MECSOL 2019 7th International Symposium on Solid Mechanics**. São Carlos, 2019.

FLANDI, L.; LEBLOND, J.-B. A new model for porous nonlinear viscous solids incorporating void shape effects – i: Theory. **European Journal of Mechanics - A/Solids**, Elsevier Science, v. 24, p. 537–551, 2005. ISSN 0997-7538.

FLANDI, L.; LEBLOND, J.-B. A new model for porous nonlinear viscous solids incorporating void shape effects – ii: Numerical validation. **European Journal of Mechanics - A/Solids**, Elsevier Science, v. 24, p. 552–571, 2005. ISSN 0997-7538.

GARRISON JR, W. M.; MOODY, N. R. Ductile fracture. **Journal of Physics and Chemistry of Solids**, Elsevier Science, v. 48, p. 1035–1074, 1987. ISSN 0022-3697.

GHAHREMANINEZHAD, A.; RAVI-CHANDAR, K. Ductile failure behavior of polycrystalline al 6061-t6. **International Journal of Fracture**, Springer Netherlands, v. 174, p. 177–202, Apr. 2012. ISSN 0376-9429.

GHAHREMANINEZHAD, A.; RAVI-CHANDAR, K. Ductile failure behavior of polycrystalline al 6061-t6 under shear dominant loading. **International Journal of Fracture**, Springer Netherlands, v. 180, p. 23–39, Mar. 2013. ISSN 0376-9429.

GOLOGANU, M.; LEBLOND, J.-B.; DEVAUX, J. Approximate models for ductile metals containing non-spherical voids–case of axisymmetric prolate ellipsoidal cavities. **Journal of the Mechanics and Physics of Solids**, Elsevier Science, v. 41, p. 1723–1754, 1993. ISSN 0022-5096.

GOLOGANU, M.; LEBLOND, J.-B.; DEVAUX, J. Approximate models for ductile metals containing non-spherical voids–case of axisymmetric oblate ellipsoidal cavities. **Journal of Engineering Materials and Technology**, Elsevier Science, v. 116, p. 290–297, 1994.

GOLOGANU, M.; LEBLOND, J.-B.; DEVAUX, J. Theoretical models for void coalescence in porous ductile solids. ii. coalescence "in columns". **International Journal of Solids and Structures**, Elsevier Science, v. 38, p. 5595–5604, 2001. ISSN 0020-7683.

GOLOGANU, M.; LEBLOND, J.-B.; PERRIN, G.; DEVAUX, J. Recent extensions of gurson's model for porous ductile metals. In: P. SUQUET (ED.). **Continuum Micromechanics**. New York: Springer-Verlag Wien, 1997, (CISM International Centre for Mechanical Sciences, v. 377). p. 61–130. ISBN 978-3-211-82902-8,978-3-7091-2662-2.

GOLOGANU, M.; LEBLOND, J.-B.; PERRIN, G.; DEVAUX, J. Theoretical models for void coalescence in porous ductile solids. i. coalescence "in layers". **International Journal of Solids and Structures**, Elsevier Science, v. 38, p. 5581–5594, 2001. ISSN 0020-7683.

GURLAND, J. Observations on the fracture of cementite particles in a spheroidized 1.05% c steel deformed at room temperature. **Acta Metallurgica**, Elsevier Science, v. 20, p. 735–741, 1972. ISSN 0001-6160.

GURSON, A. L. **Plastic flow and fracture behavior of ductile materials incorporating void nucleation, growth and interaction**. June 1975. 238 p. Doctoral dissertation (Applied Mechanics) — Brown University, Providence, June 1975.

GURSON, A. L. Continuum theory of ductile rupture by void nucleation and growth: Part i–yield criteria and flow rules for porous ductile media. **Journal of Engineering Materials and Technology**, The American Society of Mechanical Engineers, v. 99, p. 2–15, Jan. 1977.

HAHN, G. T.; KANNINEN, M. F.; ROSENFIELD, A. R. Fracture toughness of materials. **Annual Review of Materials Science**, Annual Reviews, v. 2, p. 381–404, Aug. 1972. ISSN 0084-6600.

HALTOM, S.; KYRIAKIDES, S.; RAVI-CHANDAR, K. Ductile failure under combined shear and tension. **International Journal of Solids and Structures**, Elsevier Science, v. 50, p. 1507–1522, May 2013. ISSN 0020-7683.

HANCOCK, J.; MACKENZIE, A. On the mechanisms of ductile failure in high-strength steels subjected to multi-axial stress-states. **Journal of the Mechanics and Physics of Solids**, Elsevier Science, v. 24, p. 147–160, 1976. ISSN 0022-5096.

HENRY, J. On the mode of testing building materials, and an account of the marble used in the extension of the united states capitol. **The American Association for the Advancement of Science**, G.P. Putnam & co, v. 9, p. 102–112, Aug. 1855.

HERSHEY, A. V. The plasticity of an isotropic aggregate of anisotropic face-centered cubic crystals. **Journal of Applied Mechanics**, The American Society of Mechanical Engineers, v. 21, p. 241–249, 1954.

HILL, R. A theory of the yielding and plastic flow of anisotropic metals. **Proceedings Mathematical Physical & Engineering Sciences**, The Royal Society, v. 193, p. 281–297, 1948. ISSN 1364-5021.

HILL, R. Elastic properties of reinforced solids: Some theoretical principles. **Journal of the Mechanics and Physics of Solids**, Elsevier Science, v. 11, p. 357–372, 1963. ISSN 0022-5096.

HILL, R. The essential structure of constitutive laws for metal composites and polycrystals. **Journal of the Mechanics and Physics of Solids**, Elsevier Science, v. 15, p. 79–95, 1967. ISSN 0022-5096.

HOSFORD, W. F. A generalized isotropic yield criterion. **Journal of Applied Mechanics**, The American Society of Mechanical Engineers, v. 39, p. 607–609, 1972. ISSN 0021-8936.

HUTCHINSON, J. W.; TVERGAARD, V. Comment on "influence of the lode parameter and the stress triaxiality on the failure of elasto-plastic porous materials" by k. danas and p. ponte castañeda. **International Journal of Solids and Structures**, Elsevier Science, v. 49, p. 3484–3485, 2012. ISSN 0020-7683.

JOHNSON, G. R.; COOK, W. H. Fracture characteristics of three metals subjected to various strains, strain rates, temperatures and pressures. **Engineering Fracture Mechanics**, Elsevier Science, v. 21, p. 31–48, 1985. ISSN 0013-7944.

KAILASAM, M.; ARAVAS, N.; PONTE CASTAÑEDA, P. Porous metals with developing anisotropy: Constitutive models, computational issues and applications to deformation processing. **Computer Modeling in Engineering & Sciences**, Tech Science Press, v. 1, p. 105–118, 2000. ISSN 0020-7683.

KARAFILLIS, A. P.; BOYCE, M. A general anisotropic yield criterion using bounds and a transformation weighting tensor. **Journal of the Mechanics and Physics of Solids**, Elsevier Science, v. 41, p. 1859–1886, 1993. ISSN 0022-5096.

KOPLIK, J.; NEEDLEMAN, A. Void growth and coalescence in porous plastic solids. **International Journal of Solids and Structures**, Elsevier Science, v. 24, p. 835–853, 1988. ISSN 0020-7683.

LEBLOND, J.; PERRIN, G.; SUQUET, P. Exact results and approximate models for porous viscoplastic solids. **International Journal of Plasticity**, Elsevier Science, v. 10, p. 213–235, 1994. ISSN 0749-6419.

LEBLOND, J.-B.; GOLOGANU, M. External estimate of the yield surface of an arbitrary ellipsoid containing a confocal void. **Comptes Rendus Mécanique**, Elsevier, v. 336, p. 813–819, 2008.

LENTZ, J. S. Evaluation of steel plate quality by through thickness testing. **Journal of Pressure Vessel Technology**, The American Society of Mechanical Engineers, v. 100, p. 77–84, 1978. ISSN 0094-9930.

LI, S.; SAUER, R. A.; WANG, G. The eshelby tensors in a finite spherical domain—part i: Theoretical formulations. **Journal of Applied Mechanics**, The American Society of Mechanical Engineers, v. 74, p. 770–783, 2007. ISSN 0021-8936.

LI, S.; WANG, G.; SAUER, R. A. The eshelby tensors in a finite spherical domain—part ii: Applications to homogenization. **Journal of Applied Mechanics**, The American Society of Mechanical Engineers, v. 74, p. 784–797, 2007. ISSN 0021-8936.

LIN, J.; KANIT, T.; MONCHIET, V.; SHAO, J.-F.; KONDO, D. Numerical implementation of a recent improved gurson-type model and application to ductile fracture. **Computational Materials Science**, Elsevier Science, v. 47, p. 0–906, 2010. ISSN 0927-0256.

LUDTKA, G. M.; LAUGHLIN, D. E. The influence of microstructure and strength on the fracture mode and toughness of 7xxx series aluminum alloys. **Metallurgical and Materials Transactions A**, The Minerals, Metals & Materials Society, v. 13, p. 411–425, Mar. 1982. ISSN 1073-5623.

MADOU, K.; LEBLOND, J.-B. A gurson-type criterion for porous ductile solids containing arbitrary ellipsoidal voids—i: Limit-analysis of some representative cell. **Journal of the Mechanics and Physics of Solids**, Elsevier Science, v. 60, p. 1020–1036, 2012. ISSN 0022-5096.

MADOU, K.; LEBLOND, J.-B. A gurson-type criterion for porous ductile solids containing arbitrary ellipsoidal voids—ii: Determination of yield criterion parameters. **Journal of the Mechanics and Physics of Solids**, Elsevier Science, v. 60, p. 1037–1058, 2012. ISSN 0022-5096.

MANDEL, J. **Plasticité classique et viscoplasticité**. [S.l.]: Springer Wein, 1972. (CISM Lecture Notes).

MARINO, B.; MUDRY, F.; PINEAU, A. Experimental study of cavity growth in ductile rupture. **Engineering Fracture Mechanics**, Elsevier Science, v. 22, p. 989–996, 1985. ISSN 0013-7944.

MCCLINTOCK, F. A. A criterion for ductile fracture by the growth of holes. **Journal of Applied Mechanics**, The American Society of Mechanical Engineers, v. 35, p. 363–371, 1968. ISSN 0021-8936.

MCCLINTOCK, F. A. Erratum: 'a criterion for ductile fracture by the growth of holes' (journal of applied mechanics, 1968, 35, pp. 363–371). **Journal of Applied Mechanics**, The American Society of Mechanical Engineers, v. 35, p. 617, 1968. ISSN 0021-8936.

MCCLINTOCK, F. A.; KAPLAN, S. M.; BERG, C. A. Ductile fracture by hole growth in shear bands. **International Journal of Fracture**, Springer Netherlands, v. 2, p. 614–627, 1966.

MONCHIET, V.; CAZACU, O.; CHARKALUK, E.; KONDO, D. Macroscopic yield criteria for plastic anisotropic materials containing spheroidal voids. **International Journal of Plasticity**, Elsevier Science, v. 24, p. 1158–1189, 2008. ISSN 0749-6419.

MONCHIET, V.; CHARKALUK, E.; KONDO, D. An improvement of gurson-type models of porous materials by using eshelby-like trial velocity fields. **Comptes Rendus Mécanique**, Elsevier Science, v. 335, p. 32–41, 2007. ISSN 1631-0721.

MONCHIET, V.; CHARKALUK, E.; KONDO, D. A micromechanics-based modification of the gurson criterion by using eshelby-like velocity fields. **European Journal of Mechanics - A/Solids**, Elsevier Science, v. 30, p. 940–949, 2011. ISSN 0997-7538.

MONCHIET, V.; GRUESCU, C.; CHARKALUK, E.; KONDO, D. Approximate yield criteria for anisotropic metals with prolate or oblate voids. **Comptes Rendus Mécanique**, Elsevier Science, v. 334, p. 431–439, 2006. ISSN 1631-0721.

MONCHIET, V.; KONDO, D. Exact solution of a plastic hollow sphere with a mises–schleicher matrix. **International Journal of Engineering Science**, Elsevier Science, v. 51, p. 168–178, 2012. ISSN 0020-7225.

MOODY, N. R.; GREULICH, F. A. Hydrogen-induced slip band fracture in an fe-ni-co superalloy. **Scripta Metallurgica**, Elsevier Science, v. 19, p. 1107–1111, 1985.

NAHSHON, K.; HUTCHINSON, J. Modification of the gurson model for shear failure. **European Journal of Mechanics - A/Solids**, Elsevier Science, v. 27, p. 1–17, 2008. ISSN 0997-7538.

NEMAT-NASSER, S.; HORI, M. E. **Micromechanics: Overall Properties of Heterogeneous Materials**. [S.l.]: Academic Press, Elsevier, 1993. (North-Holland Series in Applied Mathematics and Mechanics 37).

NOELL, P. J.; CARROLL, J. D.; BOYCE, B. L. The mechanisms of ductile rupture. **Acta Materialia**, Elsevier Science, v. 161, p. 83–98, Dec. 2018.

PARDOEN, T.; DELANNAY, F. Assessment of void growth models from porosity measurements in cold-drawn copper bars. **Metallurgical and Materials Transactions A**, The Minerals, Metals & Materials Society, v. 29, p. 1895–1909, July 1998. ISSN 1073-5623.

PARDOEN, T.; HUTCHINSON, J. W. An extended model for void growth and coalescence. **Journal of the Mechanics and Physics of Solids**, Elsevier Science, v. 48, p. 2467–2512, 2000. ISSN 0022-5096.

PEGEL, B.; SCHLAUBITZ, K.; BURCK, P.; LUFT, A.; BRENNER, B.; REITZENSTEIN, W. On the localization of plastic deformation in bcc single crystals. **Scripta Metallurgica**, Elsevier Science, v. 14, p. 47–52, 1980. ISSN 0036-9748.

PENROSE, R.; TODD, J. A. On best approximate solutions of linear matrix equations. **Mathematical Proceedings of the Cambridge Philosophical Society**, Cambridge University Press, v. 52, p. 17–19, Jan. 1956. ISSN 0305-0041.

PONTE CASTAÑEDA, P. The effective mechanical properties of nonlinear isotropic composites. **Journal of the Mechanics and Physics of Solids**, Elsevier Science, v. 39, p. 45–71, 1991. ISSN 0022-5096.

PONTE CASTAÑEDA, P. New variational principles in plasticity and their application to composite materials. **Journal of the Mechanics and Physics of Solids**, Elsevier Science, v. 40, p. 1757–1788, 1992. ISSN 0022-5096.

PONTE CASTAÑEDA, P. Second-order homogenization estimates for nonlinear composites incorporating field fluctuations: I–theory. **Journal of the Mechanics and Physics of Solids**, Elsevier Science, v. 50, p. 737–757, 2002. ISSN 0022-5096.

PONTE CASTAÑEDA, P. Second-order homogenization estimates for nonlinear composites incorporating field fluctuations: Ii–applications. **Journal of the Mechanics and Physics of Solids**, Elsevier Science, v. 50, p. 759–782, 2002. ISSN 0022-5096.

PONTE CASTAÑEDA, P.; ZAIDMAN, M. Constitutive models for porous materials with evolving microstructure. **Journal of the Mechanics and Physics of Solids**, Elsevier Science, v. 42, p. 1459–1497, 1994. ISSN 0022-5096.

PONTE CASTAÑEDA, P.; ZAIDMAN, M. The finite deformation of nonlinear composite materials–i. instantaneous constitutive relations. **International Journal of Solids and Structures**, Elsevier Science, v. 33, p. 1271–1286, 1996. ISSN 0020-7683.

PUTTICK, K. E. Ductile fracture in metals. **Philosophical Magazine**, Taylor and Francis Group, v. 4, p. 964–969, Aug. 1959. ISSN 1478-6435.

RICE, J.; TRACEY, D. On the ductile enlargement of voids in triaxial stress fields. **Journal of the Mechanics and Physics of Solids**, Elsevier Science, v. 17, p. 201–217, 1969. ISSN 0022-5096.

ROSENFIELD, A. R. Criteria for ductile fracture of two-phase alloys. **Metallurgical Reviews**, v. 13, p. 29–40, Jan. 1968. ISSN 0076-6690.

ROYER, D.; DIEULESAINT, E. **Elastic Waves in Solids 1**: Free and guided propagation. 1. ed. [S.l.]: Springer, 2000. v. 1. (Advanced Texts in Physics, v. 1).

ROYER, D.; DIEULESAINT, E. **Elastic waves in solids 2**: Generation, acousto-optic interaction, application. 1. ed. [S.l.]: Springer, 2000. v. 2. (Advanced Texts in Physics, v. 2).

ROZOVSKY, E.; HAHN, W. C.; AVITZUR, B. The behavior of particles during plastic deformation of metals. **Metallurgical and Materials Transactions B**, The Minerals, Metals & Materials Society, v. 4, p. 927–930, Apr. 1973. ISSN 1073-5615.

SCALES, M.; TARDIF, N.; KYRIAKIDES, S. Ductile failure of aluminum alloy tubes under combined torsion and tension. **International Journal of Solids and Structures**, Elsevier Science, July 2016. ISSN 0020-7683.

SCHWALBE, K.-H. On the influence of microstructure on crack propagation mechanisms and fracture toughness of metallic materials. **Engineering Fracture Mechanics**, Elsevier Science, v. 9, p. 795–832, 1977. ISSN 0013-7944.

SHARON, J. A.; HATTAR, K.; BOYCE, B. L.; BREWER, L. N. Compressive properties of <110> cu micro-pillars after high-dose self-ion irradiation. **Materials Research Letters**, v. 2, p. 57–62, Apr. 2014.

SOARE, S. C. On the overall yielding of an isotropic porous material with a matrix obeying a non-quadratic criterion. **International Journal of Engineering Science**, Elsevier Science, v. 104, p. 5–19, July 2016. ISSN 0020-7225.

SPEICH, G. R.; SPITZIG, W. A. Effect of volume fraction and shape of sulfide inclusions on through-thickness ductility and impact energy of high-strength 4340 plate steels. **Metallurgical and Materials Transactions A**, The Minerals, Metals & Materials Society, v. 13, p. 2239–2258, Dec. 1982. ISSN 1073-5623.

SPENCER, K.; CORBIN, S. F.; LLOYD, D. J. The influence of iron content on the plane strain fracture behaviour of aa 5754 al–mg sheet alloys. **Materials Science and Engineering: A**, Elsevier Science, v. 325, p. 394–404, 2002. ISSN 0921-5093.

SPITZIG, W. Effect of various sulfide stringer populations on the ductility of hot-rolled c-mn steels. **Acta Metallurgica**, Elsevier Science, v. 33, p. 175–184, 1985. ISSN 0001-6160.

STONE, R. H. V.; COX, T. B.; LOW, J. R.; PSIODA, J. A. Microstructural aspects of fracture by dimpled rupture. **International Metals Reviews**, v. 30, p. 157–180, Jan. 1985. ISSN 0308-4590.

TEKOĞLU, C.; HUTCHINSON, J. W.; PARDOEN, T. On localization and void coalescence as a precursor to ductile fracture. **Philosophical Transactions Mathematical Physical & Engineering Sciences**, The Royal Society, v. 373, Mar. 2015. ISSN 1364-503X.

TENG, X.; WIERZBICKI, T. Evaluation of six fracture models in high velocity perforation. **Engineering Fracture Mechanics**, Elsevier Science, v. 73, p. 1653–1678, 2006. ISSN 0013-7944.

THOMASON, P. F. Ductile fracture by the growth and coalescence of microvoids of non-uniform size and spacing. **Acta Metallurgica et Materialia**, Elsevier Science, v. 41, p. 2127–2134, July 1993. ISSN 0956-7151.

TIPPER, C. F. The fracture of metals. **Metallurgia**, v. 39, p. 133–137, 1948–49.

TRACEY, D. M. Strain-hardening and interaction effects on the growth of voids in ductile fracture. **Engineering Fracture Mechanics**, Elsevier Science, v. 3, p. 301–315, 1971. ISSN 0013-7944.

TRILLAT, M.; PASTOR, J. Limit analysis and gurson's model. **European Journal of Mechanics - A/Solids**, Elsevier Science, v. 24, p. 800–819, 2005. ISSN 0997-7538.

TRILLAT, M.; PASTOR, J.; THORé, P. Limit analysis and conic programming: 'porous drucker–prager' material and gurson's model. **Comptes Rendus Mécanique**, Elsevier Science, v. 334, p. 599–604, 2006. ISSN 1631-0721.

TVERGAARD, V. Influence of voids on shear band instabilities under plane strain conditions. **International Journal of Fracture**, Springer Netherlands, v. 17, p. 389–407, Aug. 1981. ISSN 0376-9429.

TVERGAARD, V. On localization in ductile materials containing spherical voids. **International Journal of Fracture**, Springer Netherlands, v. 18, p. 237–252, Apr. 1982. ISSN 0376-9429.

TVERGAARD, V. Material failure by void growth to coalescence. In: HUTCHINSON, J. AND WU, T. (ED.). **Advances in Applied Mechanics**. [S.l.]: Academic Press, 1990. v. 27, p. 83–151.

TVERGAARD, V.; NEEDLEMAN, A. Analysis of the cup-cone fracture in a round tensile bar. **Acta Metallurgica**, Elsevier Science, v. 32, p. 157–169, 1984. ISSN 0001-6160.

WEINRICH, P. F.; FRENCH, I. E. The influence of hydrostatic pressure on the fracture mechanisms of sheet tensile specimens of copper and brass. **Acta Metallurgica**, Elsevier Science, v. 24, p. 317–322, 1976. ISSN 0001-6160.

WILCOX, B. A.; CLAUER, A. H. The role of grain size and shape in strengthening of dispersion hardened nickel alloys. **Acta Metallurgica**, Elsevier Science, v. 20, p. 743–757, 1972. ISSN 0001-6160.

WILSON, A. D. The influence of inclusions on the toughness and fatigue properties of a516-70 steel. **Journal of Engineering Materials and Technology**, The American Society of Mechanical Engineers, v. 101, p. 265–274, 1979. ISSN 0094-4289.

ZAIDMAN, M.; PONTE CASTAÑEDA, P. The finite deformation of nonlinear composite materials–ii. evolution of the microstructure. **International Journal of Solids and Structures**, Elsevier Science, v. 33, p. 1287–1303, 1996. ISSN 0020-7683.

ZAOUI, A. Continuum micromechanics: Survey. **Journal of Engineering Mechanics**, American Society of Civil Engineers, v. 128, p. 808–816, Aug. 2002. ISSN 0733-9399.

Appendix

APPENDIX A – THE VOIGT NOTATION FOR TENSOR OPERATIONS

The Voigt notation provides a very convenient approach to perform tensorial operations. It consists of representing symmetric fourth ($\mathbb{L}$) and second-order ($\dot{\boldsymbol{\epsilon}}$) tensors by matrices ($\underline{\underline{\boldsymbol{L}}}$) and vectors ($\underline{\dot{\boldsymbol{\epsilon}}}$), respectively. Since the tensors are assumed to hold symmetry (i.e. $L_{ijkl} = L_{ikjl} = L_{kilj}$ and $\epsilon_{ij} = \epsilon_{ji}$), it avoids the evaluation of unnecessary operations, which saves computing time.

Fourth-order tensors are represented by conveniently composing its matrix form as

$$\underline{\underline{\boldsymbol{L}}} = \begin{bmatrix} L_{1111} & L_{1122} & L_{1133} & \sqrt{2}L_{1123} & \sqrt{2}L_{1131} & \sqrt{2}L_{1112} \\ L_{1122} & L_{2222} & L_{2233} & \sqrt{2}L_{2223} & \sqrt{2}L_{2231} & \sqrt{2}L_{2212} \\ L_{1133} & L_{2233} & L_{3333} & \sqrt{2}L_{3323} & \sqrt{2}L_{3331} & \sqrt{2}L_{3312} \\ \sqrt{2}L_{1123} & \sqrt{2}L_{2223} & \sqrt{2}L_{3323} & 2L_{2323} & 2L_{2331} & 2L_{2312} \\ \sqrt{2}L_{1131} & \sqrt{2}L_{2231} & \sqrt{2}L_{3331} & 2L_{2331} & 2L_{3131} & 2L_{3112} \\ \sqrt{2}L_{1112} & \sqrt{2}L_{2212} & \sqrt{2}L_{3312} & 2L_{2312} & 2L_{3112} & 2L_{1212} \end{bmatrix} \tag{A.1}$$

and second-order tensor in its vector form as

$$\underline{\dot{\boldsymbol{\epsilon}}} = \begin{Bmatrix} \epsilon_{11} \\ \epsilon_{22} \\ \epsilon_{33} \\ \sqrt{2}\epsilon_{23} \\ \sqrt{2}\epsilon_{31} \\ \sqrt{2}\epsilon_{12} \end{Bmatrix} \tag{A.2}$$

Due to the coefficients 2 and $\sqrt{2}$ conveniently applied in certain positions in the matrix and vector forms (Eq. (A.1) and (A.2)), the following tensor operations can be easily performed by using conventional matrix algebra products:

- Double contraction of a fourth-order tensor by a second-order tensor ($\mathbb{L} : \dot{\boldsymbol{\epsilon}}$)

$$\mathbb{L} : \dot{\boldsymbol{\epsilon}} \equiv \underline{\underline{\boldsymbol{L}}}\,\underline{\dot{\boldsymbol{\epsilon}}}; \tag{A.3}$$

- Double contraction of between two second-order tensors ($\dot{\boldsymbol{\epsilon}} : \dot{\boldsymbol{\epsilon}}$)

$$\dot{\boldsymbol{\epsilon}} : \dot{\boldsymbol{\epsilon}} \equiv \underline{\dot{\boldsymbol{\epsilon}}}^T \underline{\dot{\boldsymbol{\epsilon}}}; \tag{A.4}$$

  and

- Cross product of two second-order tensors ($\dot{\boldsymbol{\epsilon}} \otimes \dot{\boldsymbol{\epsilon}}$)

$$\dot{\boldsymbol{\epsilon}} \otimes \dot{\boldsymbol{\epsilon}} \equiv \underline{\dot{\boldsymbol{\epsilon}}}\,\underline{\dot{\boldsymbol{\epsilon}}}^T \tag{A.5}$$

APPENDIX B – A PROCEDURE FOR INTERPOLATION OF N-DIMENSIONAL FUNCTIONS FROM STRUCTURED MESH DATA

Let us consider a function $f : \mathbb{R}^{N-1} \rightarrow \mathbb{R}^N$ that has been evaluated in $n_1 \cdot n_2 \cdot ... \cdot n_{N-1}$ points lying on a structured – but not necessarily regular – grid such that $f(\boldsymbol{x^i}) = \boldsymbol{y^i}$, where

$$f(\boldsymbol{x^i}) = f(\boldsymbol{x}^{(i_1,i_2,...,i_{N-1})}), \tag{B.1}$$

$$\boldsymbol{x}^{(i_1,i_2,...,i_{N-1})} = (x_1^{i_1}, x_2^{i_2}, ..., x_{N-1}^{i_{N-1}}), \tag{B.2}$$

and

$$\boldsymbol{y^i} = (y_1^{\boldsymbol{i}}, y_2^{\boldsymbol{i}}, ..., y_N^{\boldsymbol{i}}), \tag{B.3}$$

for $i_j = 1, ..., n_j$, $j = 1, ..., N-1$.

One assumes that $(N-1)$-dimensional hypercubes constitute $(N-1)$-dimensional subdomains (or *elements*). The k-th vertex of the $(i_1, ..., i_{N-1}) \times (i_1 + 1, ..., i_{N-1} + 1)$ hypercube are positioned at $\boldsymbol{x} = \boldsymbol{x^k}$, where $\boldsymbol{k}$ is the k-th subset – among 2^{N-1} possible ones – given by the cartesian product $(i_1, ..., i_{N-1}) \times (i_1 + 1, ..., i_{N-1} + 1)$. One then defines a shape function $\chi_k : \mathbb{R}^{N-1} \rightarrow \mathbb{R}$, associated to the k-th vertex of a given subdomain:

$$\chi_k(\boldsymbol{\iota}) = \frac{1}{2^{N-1}} \prod_{k=1}^{(N-1)} (\iota_k + a_k), \tag{B.4}$$

where $\boldsymbol{\iota} = (\iota_1, ..., \iota_{N-1})$ is a local coordinate system such that $\iota_k \in [-1, 1]$ and a_k is k-th multisubset (i.e. a subset that can contain repeated elements) obtained from the cartesian product of the $(N-1)$-dimensional multisubsets $(-1, ..., -1) \times (1, ..., 1)$.

For each element, one may thus divide the range of each natural coordinate $\iota_k \in [-1, 1]$ so that an auxiliary *subgrid* be defined inside that element. In each position of this new subgrid the function f can be then approximated by

$$f(\boldsymbol{x^i}(\boldsymbol{\iota})) = \sum_{k=1}^{2^{N-1}} f(\boldsymbol{x^k}) \chi_k(\boldsymbol{\iota}), \tag{B.5}$$

where

$$\boldsymbol{x^i}(\boldsymbol{\iota}) = \sum_{k=1}^{2^{N-1}} \boldsymbol{x^k} \chi_k(\boldsymbol{\iota}). \tag{B.6}$$

One may finally verify whether the approximated values of f – that are obtained in each point lying on the subgrid correspondent to each element (i.e. hypercube) – respect

a given level-set condition (e.g. $y_1 = y_2 = ... = y_{N-2} = 0$). The collection of every approximated value comprises a level-set solution to the given level-set condition.

For example, if $N = 3$, Eq. (B.4) retrieves the two-dimensional interpolation function given in Eq. (7.24). Furthermore, $N = 6$ can be used to obtain contour plots of six-dimensional anisotropic yield surfaces.

APPENDIX C – THE EXPRESSIONS OF THE DERIVATIVES INVOLVED IN THE CHAPTER 7

C.1 Derivatives in Eq. (6.16)

$$\frac{\partial \tilde{s}_{eq}}{\partial s^1_{eq}} = \frac{s^1_{eq}}{\tilde{s}_{eq}} \tag{C.1}$$

$$\frac{\partial \tilde{s}_{eq}}{\partial s^2_{eq}} = \frac{s^2_{eq}}{\tilde{s}_{eq}} \tag{C.2}$$

$$\frac{\partial s^1_{eq}}{\partial \boldsymbol{s}^1} = \frac{3}{2}\frac{\boldsymbol{s}^1}{s^1_{eq}} \tag{C.3}$$

$$\frac{\partial s^2_{eq}}{\partial \boldsymbol{s}^2} = \frac{3}{2}\frac{\boldsymbol{s}^2}{s^2_{eq}} \tag{C.4}$$

$$\frac{\partial s^1_{eq}}{\partial \boldsymbol{s}^2} = \frac{\partial s^2_{eq}}{\partial \boldsymbol{s}^1} = \mathbf{0} \tag{C.5}$$

$$h_{ij} = (\cos\alpha\cos\omega^1_i - \sin\alpha\cos\omega^2_j)|\cos\alpha\cos\omega^1_i - \sin\alpha\cos\omega^2_j|^{m-2} \tag{C.6}$$

$$\frac{\partial g}{\partial \omega^1} = -\left(\frac{2}{3}\right)^m \frac{1}{4} g^{(1-m)} \sum_{j=1}^{3}\sum_{i=1}^{3} h_{ij}\cos\alpha\sin\omega^1_i \tag{C.7}$$

$$\frac{\partial g}{\partial \omega^2} = \left(\frac{2}{3}\right)^m \frac{1}{4} g^{(1-m)} \sum_{j=1}^{3}\sum_{i=1}^{3} h_{ij}\sin\alpha\sin\omega^2_j \tag{C.8}$$

$$\frac{\partial g}{\partial \alpha} = -\left(\frac{2}{3}\right)^m \frac{1}{4} g^{(1-m)} \sum_{j=1}^{3}\sum_{i=1}^{3} h_{ij}(\sin\alpha\cos\omega^1_i + \cos\alpha\cos\omega^2_j) \tag{C.9}$$

$$\frac{\partial \omega^1}{\partial \boldsymbol{s}^1} = -\frac{9}{2}\frac{1}{s^1_{eq}\sin 3\omega^1}\left[\left(\frac{\boldsymbol{s}^1}{s^1_{eq}}\right)^2 - \frac{2}{9}\mathbf{1} - \frac{1}{3}\cos 3\omega^1\left(\frac{\boldsymbol{s}^1}{s^1_{eq}}\right)\right] \tag{C.10}$$

$$\frac{\partial \omega^1}{\partial \boldsymbol{s}^2} = \frac{\partial \omega^2}{\partial \boldsymbol{s}^1} = \mathbf{0} \tag{C.11}$$

$$\frac{\partial \omega^2}{\partial \boldsymbol{s}^2} = -\frac{9}{2}\frac{1}{s^2_{eq}\sin 3\omega^2}\left[\left(\frac{\boldsymbol{s}^2}{s^2_{eq}}\right)^2 - \frac{2}{9}\mathbf{1} - \frac{1}{3}\cos 3\omega^1\left(\frac{\boldsymbol{s}^2}{s^2_{eq}}\right)\right] \tag{C.12}$$

$$\frac{\partial \alpha}{\partial \boldsymbol{s}^1} = \frac{3}{2}\cos^2\alpha\tan\alpha\frac{\boldsymbol{s}^1}{(s^1_{eq})^2} \tag{C.13}$$

$$\frac{\partial \alpha}{\partial \boldsymbol{s}^2} = \frac{3}{2}\cos^2\alpha\frac{\boldsymbol{s}^2}{s^1_{eq}s^2_{eq}} \tag{C.14}$$

C.2 Derivatives in Eq. (6.28)

$$\frac{\partial \tilde{\pi}}{\partial \dot{\epsilon}^1_{eq}} = \sigma_0^2\frac{\dot{\epsilon}^1_{eq}}{\tilde{\pi}} \tag{C.15}$$

$$\frac{\partial \tilde{\pi}}{\partial \dot{\epsilon}^2_{eq}} = \sigma_0^2\frac{\dot{\epsilon}^2_{eq}}{\tilde{\pi}} \tag{C.16}$$

$$\frac{\partial \dot{\epsilon}^1_{eq}}{\partial \dot{\boldsymbol{\epsilon}}^1} = \frac{2}{3}\frac{\dot{\boldsymbol{\epsilon}}^1}{\dot{\epsilon}^1_{eq}} \tag{C.17}$$

$$\frac{\partial \dot{\epsilon}^1_{eq}}{\partial \dot{\boldsymbol{\epsilon}}^2} = \frac{\partial \dot{\epsilon}^2_{eq}}{\partial \dot{\boldsymbol{\epsilon}}^1} = \boldsymbol{0} \tag{C.18}$$

$$\frac{\partial \dot{\epsilon}^2_{eq}}{\partial \dot{\boldsymbol{\epsilon}}^2} = \frac{2}{3}\frac{\dot{\boldsymbol{\epsilon}}^2}{\dot{\epsilon}^2_{eq}} \tag{C.19}$$

$$\frac{\partial \dot{\boldsymbol{\epsilon}}^1}{\partial \dot{\boldsymbol{E}}}(r,\varphi,\theta) = \mathbb{L}_1^+ + \frac{1}{3}\left(\frac{R}{r}\right)^3 \boldsymbol{1}\otimes\left\{\mathbb{L}_1^+ : [\boldsymbol{1} - 3\boldsymbol{e}_r(\varphi,\theta)\otimes\boldsymbol{e}_r(\varphi,\theta)]\right\} \tag{C.20}$$

$$\frac{\partial \dot{\boldsymbol{\epsilon}}^2}{\partial \dot{\boldsymbol{E}}}(r,\varphi,\theta) = \mathbb{L}_2^+ + \frac{1}{3}\left(\frac{R}{r}\right)^3 \boldsymbol{1}\otimes\left\{\mathbb{L}_2^+ : [\boldsymbol{1} - 3\boldsymbol{e}_r(\varphi,\theta)\otimes\boldsymbol{e}_r(\varphi,\theta)]\right\} \tag{C.21}$$

C.3 Derivatives in Eq. (6.29)

The second derivatives of the function $g(\omega^1,\omega^2,\alpha)$ (g_{11}, g_{22}, $g_{\alpha\alpha}$, g_{12}, g_{21}, $g_{1\alpha}$, $g_{\alpha 1}$, $g_{2\alpha}$ and $g_{\alpha 2}$) are given in section C.4.

$$\frac{\partial G}{\partial \omega^1} - G(\omega^1,\omega^2,\alpha)\left(gg_1 + g_\alpha g_{\alpha 1} + g_1 g_{11}\sec\alpha + g_2 g_{21}\csc\alpha\right) \tag{C.22}$$

$$\frac{\partial G}{\partial \omega^2} - G(\omega^1,\omega^2,\alpha)\left(gg_2 + g_\alpha g_{\alpha 2} + g_1 g_{12}\sec\alpha + g_2 g_{22}\csc\alpha\right) \tag{C.23}$$

$$\frac{\partial G}{\partial \alpha} = -G(\omega^1, \omega^2, \alpha)[g_\alpha + g_\alpha g_{\alpha\alpha} + g_1 \sec\alpha\,(g_1 \tan\alpha \sec\alpha + g_{1\alpha} \sec\alpha) + g_2 \csc\alpha\,(g_{2\alpha} \csc\alpha - g_2 \cot\alpha \csc\alpha)] \tag{C.24}$$

$$\begin{bmatrix} \frac{\partial\omega^1}{\partial\xi^1} & \frac{\partial\omega^1}{\partial\xi^2} & \frac{\partial\omega^1}{\partial\beta} \\ \frac{\partial\omega^2}{\partial\xi^1} & \frac{\partial\omega^2}{\partial\xi^2} & \frac{\partial\omega^2}{\partial\beta} \\ \frac{\partial\alpha}{\partial\xi^1} & \frac{\partial\alpha}{\partial\xi^2} & \frac{\partial\alpha}{\partial\beta} \end{bmatrix} = \begin{bmatrix} \frac{\partial\xi^1}{\partial\omega^1} & \frac{\partial\xi^1}{\partial\omega^2} & \frac{\partial\xi^1}{\partial\alpha} \\ \frac{\partial\xi^2}{\partial\omega^1} & \frac{\partial\xi^2}{\partial\omega^2} & \frac{\partial\xi^2}{\partial\alpha} \\ \frac{\partial\beta}{\partial\omega^1} & \frac{\partial\beta}{\partial\omega^2} & \frac{\partial\beta}{\partial\alpha} \end{bmatrix}^{-1} \tag{C.25}$$

$$\frac{\partial\xi^1}{\partial\omega^1} = 1 + \frac{\sec^2\alpha\,[\tan\alpha g_1 g_{1\alpha} + g_{11}\,(g - \tan\alpha g_\alpha)]}{(g - \tan\alpha g_\alpha)^2 + g_1^2 \sec^4\alpha} \tag{C.26}$$

$$\frac{\partial\xi^1}{\partial\omega^2} = \frac{\sec^2\alpha\,[\tan\alpha g_1 g_{2\alpha} + g_{12}\,(g - \tan\alpha g_\alpha)]}{(g - \tan\alpha g_\alpha)^2 + g_1^2 \sec^4\alpha} \tag{C.27}$$

$$\frac{\partial\xi^1}{\partial\alpha} = \frac{\sec^2\alpha\,\{[g_\alpha \cos 2\alpha \sec^2\alpha + \tan\alpha(2g + g_{\alpha\alpha})]\,g_1 + (g - g_\alpha \tan\alpha) g_{1\alpha}\}}{(g - \tan\alpha g_\alpha)^2 + g_1^2 \sec^4\alpha} \tag{C.28}$$

$$\frac{\partial\xi^2}{\partial\omega^1} = \frac{\csc^2\alpha\,[-g_2 g_{1\alpha} \cot\alpha + (g + g_\alpha \cot\alpha)\,g_{12}]}{(g + g_\alpha \cot\alpha)^2 + g_2^2 \csc^4\alpha} \tag{C.29}$$

$$\frac{\partial\xi^2}{\partial\omega^2} = 1 + \frac{\csc^2\alpha\,[-g_2 g_{2\alpha} \cot\alpha + (g + g_\alpha \cot\alpha)\,g_{22}]}{(g + g_\alpha \cot\alpha)^2 + g_2^2 \csc^4\alpha} \tag{C.30}$$

$$\frac{\partial\xi^2}{\partial\alpha} = \frac{-\frac{1}{2}\csc^2\alpha\,[2g_\alpha \cos 2\alpha + (2g + g_{\alpha\alpha}) \sin 2\alpha]\,g_2 + g_{2\alpha} \csc^2\alpha (g + g_\alpha \cot\alpha)}{(g + g_\alpha \cot\alpha)^2 + g_2^2 \csc^4\alpha} \tag{C.31}$$

$$\begin{aligned} \frac{\partial\beta}{\partial\omega^1} = &\Big\{\Big[(g\cos\alpha - g_\alpha \sin\alpha)^2 + g_1^2 \sec^2\alpha\Big]\Big[2\cos\alpha(g\sin\alpha + g_\alpha\cos\alpha)g_{1\alpha} + 2g_2 g_{12}\csc^2\alpha\Big] - \\ &\Big[(g\sin\alpha + g_\alpha\cos\alpha)^2 + g_2^2\csc^2\alpha\Big]\Big[2\sin\alpha(-g\cos\alpha + g_\alpha\sin\alpha)g_{1\alpha} + 2g_1 g_{11}\sec^2\alpha\Big]\Big\}/ \\ &\Big\{2\tan\beta(1+\tan^2\beta)\Big[(g\cos\alpha - g_\alpha\sin\alpha)^2 + g_1^2\sec^2\alpha\Big]\Big\} \end{aligned} \tag{C.32}$$

$$\begin{aligned}\frac{\partial\beta}{\partial\omega^1} =&\Big\{\Big[2\cos\alpha(g\sin\alpha+g_\alpha\cos\alpha)g_{2\alpha}+2g_2g_{22}\csc^2\alpha\Big]\Big[(g\cos\alpha-g_\alpha\sin\alpha)^2+g_1^2\sec^2\alpha\Big]-\\&\Big[(g\sin\alpha+g_\alpha\cos\alpha)^2+g_2^2\csc^2\alpha\Big]\Big[2\sin\alpha(-g\cos\alpha+g_\alpha\sin\alpha)g_{2\alpha}+2g_1g_{12}\sec^2\alpha\Big]\Big\}/\\&\Big\{2\tan\beta(1+\tan^2\beta)\Big[(g\cos\alpha-g_\alpha\sin\alpha)^2+g_1^2\sec^2\alpha\Big]\Big\}\end{aligned} \tag{C.33}$$

$$\begin{aligned}\frac{\partial\beta}{\partial\omega^1} =&\Big\{\Big[2(g\sin\alpha+g_\alpha\cos\alpha)(-g_\alpha\sin\alpha+(g+g_{\alpha\alpha})\cos\alpha)-2g_2^2\cot\alpha\csc^2\alpha+2g_2g_{2\alpha}\csc^2\alpha\Big]\\&\Big[(g\cos\alpha-g_\alpha\sin\alpha)^2+g_1^2\sec^2\alpha\Big]-\\&2\Big[(g\sin\alpha+g_\alpha\cos\alpha)^2+g_2^2\csc^2\alpha\Big]-\\&\Big[-(g\cos\alpha-g_\alpha\sin\alpha)(g_\alpha\cos\alpha+\sin\alpha(g+g_{\alpha\alpha}))+g_1^2\sec^\alpha\tan\alpha+g_1g_{1\alpha}\sec^2\alpha\Big]\Big\}/\\&\Big\{2\tan\beta(1+\tan^2\beta)\Big[(g\cos\alpha-g_\alpha\sin\alpha)^2+g_1^2\sec^2\alpha\Big]\Big\}\end{aligned} \tag{C.34}$$

C.4 Second derivatives of the function $g(\omega^1,\omega^2,\alpha)$

$$\begin{aligned}g_{11} =&-\frac{2}{3}^m\frac{1}{4}(1-m)g^{-m}g_1\sum_{j=1}^{3}\sum_{i=1}^{3}h_{ij}\cos\alpha\sin\omega_i^1+\\&-\frac{2}{3}^m\frac{1}{4}g^{1-m}\sum_{i=1}^{3}\left(\frac{\partial h_{ij}}{\partial\omega^1}\cos\alpha\sin\omega_i^1+h_{ij}\cos\alpha\cos\omega_i^1\right)\end{aligned} \tag{C.35}$$

$$\begin{aligned}g_{12} =&-\frac{2}{3}^m\frac{1}{4}(1-m)g^{-m}g_2\sum_{j=1}^{3}\sum_{i=1}^{3}h_{ij}\cos\alpha\sin\omega_i^1+\\&-\frac{2}{3}^m\frac{1}{4}g^{1-m}\sum_{i=1}^{3}\left(\frac{\partial h_{ij}}{\partial\omega^2}\cos\alpha\sin\omega_i^1\right)\end{aligned} \tag{C.36}$$

$$\begin{aligned}g_{1\alpha} =&-\frac{2}{3}^m\frac{1}{4}(1-m)g^{-m}g_\alpha\sum_{j=1}^{3}\sum_{i=1}^{3}h_{ij}\cos\alpha\sin\omega_i^1+\\&-\frac{2}{3}^m\frac{1}{4}g^{1-m}\sum_{i=1}^{3}\left(\frac{\partial h_{ij}}{\partial\alpha}\cos\alpha\sin\omega_i^1-h_{ij}\sin\alpha\sin\omega_i^1\right)\end{aligned} \tag{C.37}$$

$$\begin{aligned}g_{21} =&\frac{2}{3}^m\frac{1}{4}(1-m)g^{-m}g_1\sum_{j=1}^{3}\sum_{i=1}^{3}h_{ij}\sin\alpha\sin\omega_j^2+\\&+\frac{2}{3}^m\frac{1}{4}g^{1-m}\sum_{i=1}^{3}\left(\frac{\partial h_{ij}}{\partial\omega^1}\sin\alpha\sin\omega_j^2\right)\end{aligned} \tag{C.38}$$

$$\begin{aligned} g_{22} =& \frac{2}{3}^m \frac{1}{4}(1-m)g^{-m}g_2 \sum_{j=1}^{3}\sum_{i=1}^{3} h_{ij} \sin\alpha \sin\omega_j^2 + \\ &+ \frac{2}{3}^m \frac{1}{4} g^{1-m} \sum_{i=1}^{3} \left(\frac{\partial h_{ij}}{\partial \omega^2} \sin\alpha \sin\omega_j^2 + h_{ij} \sin\alpha \cos\omega_j^2 \right) \end{aligned} \tag{C.39}$$

$$\begin{aligned} g_{2\alpha} =& \frac{2}{3}^m \frac{1}{4}(1-m)g^{-m}g_\alpha \sum_{j=1}^{3}\sum_{i=1}^{3} h_{ij} \sin\alpha \sin\omega_j^2 + \\ &+ \frac{2}{3}^m \frac{1}{4} g^{1-m} \sum_{i=1}^{3} \left(\frac{\partial h_{ij}}{\partial \alpha} \sin\alpha \sin\omega_j^2 + h_{ij} \cos\alpha \sin\omega_j^2 \right) \end{aligned} \tag{C.40}$$

$$\begin{aligned} g_{\alpha 1} =& -\frac{2}{3}^m \frac{1}{4}(1-m)g^{-m}g_1 \sum_{j=1}^{3}\sum_{i=1}^{3} h_{ij}(\sin\alpha\cos\omega_i^1 + \cos\alpha\cos\omega_j^2) + \\ &- \frac{2}{3}^m \frac{1}{4} g^{1-m} \sum_{i=1}^{3} \left[\frac{\partial h_{ij}}{\partial \omega^1}(\sin\alpha\cos\omega_i^1 + \cos\alpha\cos\omega_j^2) - h_{ij}\sin\alpha\sin\omega_i^1 \right] \end{aligned} \tag{C.41}$$

$$\begin{aligned} g_{\alpha 2} =& -\frac{2}{3}^m \frac{1}{4}(1-m)g^{-m}g_2 \sum_{j=1}^{3}\sum_{i=1}^{3} h_{ij}(\sin\alpha\cos\omega_i^1 + \cos\alpha\cos\omega_j^2) + \\ &- \frac{2}{3}^m \frac{1}{4} g^{1-m} \sum_{i=1}^{3} \left[\frac{\partial h_{ij}}{\partial \omega^2}(\sin\alpha\cos\omega_i^1 + \cos\alpha\cos\omega_j^2) - h_{ij}\cos\alpha\sin\omega_j^2 \right] \end{aligned} \tag{C.42}$$

$$\begin{aligned} g_{\alpha 1} =& -\frac{2}{3}^m \frac{1}{4}(1-m)g^{-m}g_\alpha \sum_{j=1}^{3}\sum_{i=1}^{3} h_{ij}(\sin\alpha\cos\omega_i^1 + \cos\alpha\cos\omega_j^2) + \\ &- \frac{2}{3}^m \frac{1}{4} g^{1-m} \sum_{i=1}^{3} \left[\frac{\partial h_{ij}}{\partial \alpha}(\sin\alpha\cos\omega_i^1 + \cos\alpha\cos\omega_j^2) - h_{ij}(\cos\alpha\cos\omega_i^1 - \sin\alpha\cos\omega_j^2) \right] \end{aligned} \tag{C.43}$$

$$\frac{\partial h_{ij}}{\partial \omega^1} = -(m-1)|\cos\alpha\cos\omega_i^1 - \sin\alpha\cos\omega_j^2|^{m-2}\cos\alpha\sin\omega_i^1 \tag{C.44}$$

$$\frac{\partial h_{ij}}{\partial \omega^2} = (m-1)|\cos\alpha\cos\omega_i^1 - \sin\alpha\cos\omega_j^2|^{m-2}\sin\alpha\sin\omega_j^2 \tag{C.45}$$

$$\frac{\partial h_{ij}}{\partial \alpha} = -(m-1)|\cos\alpha\cos\omega_i^1 - \sin\alpha\cos\omega_j^2|^{m-2}(\sin\alpha\cos\omega_i^1 + \cos\alpha\cos\omega_j^2) \tag{C.46}$$